HU ISSN 2063-6997

GEOSCIENCES AND ENGINEERING

A Publication of the University of Miskolc

Volume 13, Number 1 (2025)

Comminution and Classification for the Circular Economy
Special Issue of the 18th ESCC

Miskolc, University Press

GEOSCIENCES AND ENGINEERING
A Publication of the University of Miskolc
Volume 13, Number 1
Miskolc, University Press
UNIVERSITY OF MISKOLC
FACULTY OF EARTH AND ENVIRONMENTAL SCIENCES & ENGINEERING
HU ISSN 2063-6997

TABLE OF CONTENTS

Geosciences and Engineering, Vol. 13, No. 1 (2025), p. 5.

Comminution and Classification for the Circular Economy, Special Issue of the 18th ESCC in Geosciences and Engineering

Editorial

The 18th European Symposium on Comminution and Classification was held in Miskolc, Hungary, from Monday, June 24th to Wednesday, 26th, 2024 at the University of Miskolc, Hungary. The symposium was organised on behalf of the Working Party Comminution and Classification of the European Federation of Chemical Engineering (EFCE). The organisers were the University of Miskolc, Faculty of Earth and Environmental Sciences and Engineering, Institute of Raw Materials Preparation and Environmental Technology and the Hungarian Chemical Society. This bi-annual conference has a long history of facilitating impactful discussions and networking and results dissemination among expert professionals from both academia and industry in the field since 1964. The two most recent successful events were the 16th in Leeds, UK and the 17th in Toulouse, France. This ESCC is the second one in Hungary and the first one in Miskolc. We think it was the right place, because our predecessor is the world's first technical higher education institution the "Bergakademie of Banská Štiavnica" and therefore, this institution carries within itself the cradle of mineral processing and of course its core comminution and classification roots.

This event has further broadened the traditional scope of ESCC conferences of fundamentals of breakage, advanced modelling of fine- and coarse comminution and classification processes and applications for various industries, i.e. mineral processing, bio-refinery, food, pharmaceutical, chemical, electronic and materials industries with waste recycling and with mechanochemical-mechanofusion processes. The foundation of the circular economy is the recirculation of previously used materials (anthropogenic materials) of which central elements are the first comminution and separation mechanical processes, and this is the reason why this special issue is dedicated to the circular economy. Altogether 80 presentations, including 3 plenary and 4 keynote speakers, parallel 2 times 7 oral sessions, including 64 oral lectures and 1 poster session, which includes 9 posters, were held according to the Programme of ESCC 2024. Some selected papers were invited for publication in the dedicated special issue of Geosciences and Engineering, whose title is "Comminution and Classification for the Circular Economy, Special Issue of 18th ESCC".

The editors wish the readers of this special issue a pleasant and, above all, useful time, which provides an insight into the scientific and professional atmosphere of the 2024 ESCC conference.

With miner's greetings: Good Luck!

J. Faitli and Á. Rácz, organisers and guest editors

Geosciences and Engineering, Vol. 13, No. 1 (2025), pp. 7–17.
https://doi.org/10.33030/geosciences.2025.01.001

INFLUENCE OF FEEDSTOCK COMPOSITION ON THE ADSORPTIVE PROPERTIES OF RDF-BASED ACTIVATED CARBON

EMESE SEBE[1,*], JOHN KWAME BEDIAKO[2], YOUSSEF EL OUARDI[3], GÁBOR NAGY[4]

[1,*]*Institute of Energy, Ceramic and Polymer Technology, University of Miskolc, emese.sebe@uni-miskolc.hu*
[2]*Department of Separation Science, School of Engineering Science, Lappeenranta-Lathi University of Technology (LUT), FI-53850, Lappeenranta, Finland; john.bediako@lut.fi*
[3]*Department of Separation Science, School of Engineering Science, Lappeenranta-Lathi University of Technology (LUT), FI-53850, Lappeenranta, Finland; youssef.el.ouardi@lut.fi*
[4]*Institute of Energy, Ceramic and Polymer Technology, University of Miskolc, gabor.nagy2@uni-miskolc.hu*
[1]*https://orcid.org/0000-0003-4797-4024*
[2]*https://orcid.org/0000-0003-1816-4890*
[3]*https://orcid.org/0000-0002-3199-0006*
[4]*https://orcid.org/0000-0003-3571-9122*

Abstract: This study focuses on converting refuse-derived fuel mixtures (composed of PS, PP, HDPE, paper, cardboard, cotton, and wood) into activated carbon through pyrolysis at 520 °C. The resulting chars underwent steam gasification at 900 °C for 60 min, with a steam flow rate of 5 $cm^3\ h^{-1}$. The physically activated chars were then systematically examined for their efficacy in removing phenol from 20 mg dm^{-3} solutions. The study demonstrated that the produced chars exhibited approximately half of the phenol removal efficiency of commercial activated carbon. Furthermore, an increased plastic content in the RDF blend enhanced the adsorption performance of the resulting activated carbons.

Keywords*: activated carbon, refuse-derived fuel, adsorption, phenol, gasification, pyrolysis*

1. INTRODUCTION

Among the various adsorbent materials, activated carbons are widely utilized in water and gas purification. Approximately 100,000 tonnes of activated carbon are produced annually (Heidarinejad et al., 2020). One characteristic that stands out compared to zeolites and polymer-based adsorbents is their resistance to toxic and corrosive environments. The most common raw materials for activated carbon production include wood, bituminous coal, lignite, and coconut. However, there is an increasing demand for utilizing various wastes as raw materials (Heidarinejad et al., 2020).

Globally, more than 2.2 billion tonnes of municipal solid waste is generated each year and it is expected to reach 3.9 billion tonnes by 2050 (Liu et al., 2024). Municipal solid waste is rich in carbonaceous materials; therefore, it could serve as an alternative raw material for activated carbon production. The challenge with this waste

lies in its heterogeneous and variable nature. However, the fluctuations in its characteristics can be significantly reduced through mechanical processing, such as converting it into refuse-derived fuel (RDF).

The production of activated carbon involves two main steps: carbonization and activation. Activation can be achieved through physical methods, chemical methods, or impregnation (Thapar Kapoor et al., 2021). When physical activation is conducted using steam, an additional product is generated, i.e., synthesis gas (syngas). This gas primarily comprises hydrogen and carbon-monoxide and may find application in the chemical industry.

In this study, activated carbons were produced under laboratory conditions using RDF mixtures with varying compositions, and their phenol adsorption capacities were investigated. Phenol was selected as the adsorbate due to its prevalence as the main component of effluents from biomass gasification. Additionally, phenolic wastewater is commonly generated across various industrial sectors, including polypropylene production, oil refineries, and the paper, pharmaceutical, and textile industries (Cunha and Aguiar, 2014; Hernández-Fernández et al., 2021; Ke et al., 2022; Wang et al., 2022).

2. MATERIALS AND METHODS

2.1. Base material

The seven different materials investigated, which are commonly found in municipal waste, can be grouped into two categories, i.e., cellulosic materials (cardboard, paper, wood, cotton) and plastics (PS, PP, HDPE) (Figure 1).

Figure 1
Base components of RDF mixtures (1. cardboard, 2. office paper, 3. wood, 4. cotton, 5. PP, 6. PS, 7. HDPE)

Using the seven components presented above, model laboratory RDF mixtures with varying compositions were prepared, as shown in Table 1. The composition of RDF1 is based on an analysis of an RDF sample from a production plant in Hejőpapi,

Hungary (Ladányi, 2015). A minor adjustment was made by excluding polyethylene terephthalate (PET), as there is an existing technology capable of effectively removing this component. This step was deemed necessary for two reasons: firstly, by separating PET, it becomes available for recycling; secondly, the pyrolysis of PET can pose challenges, such as the formation of benzoic acid, which can lead to system blockages and potential organic acid pollution (Xayachak et al., 2022). In the RDF2 and RDF3 samples, the total plastic content was increased by 10% and 20% by weight, respectively.

Table 1

Composition of RDF mixtures [wt.%]

Component	RDF1	RDF2	RDF3
Cardboard	9.00	7.76	6.52
Office paper	49.50	42.67	35.84
PP	5.50	7.50	9.50
HDPE	16.50	22.50	28.50
PS	5.50	7.50	9.50
Wood	10.00	8.62	7.24
Cotton	4.00	3.45	2.90

2.2. Activated carbon preparation

The experimental systems are depicted in Figure 2. The RDF mixture was subjected to pyrolysis at 520 °C with a heating rate of approximately 3.5 °C min^{-1}. The pyrolysis temperature was selected based on prior thermogravimetric analysis. Pyrolysis was conducted in a laboratory pyrolysis reactor equipped with electric heating. The material was placed in a 1 dm^3 beaker inside the reactor. After leaving the reactor, the pyrolysis gas passed through a heat exchanger, and the condensed liquid was collected in a glass vessel. The pyrolysis gases were also collected in a multi-layer gas sampling bag and subsequently analyzed using an Agilent 490 Micro GC gas chromatograph.

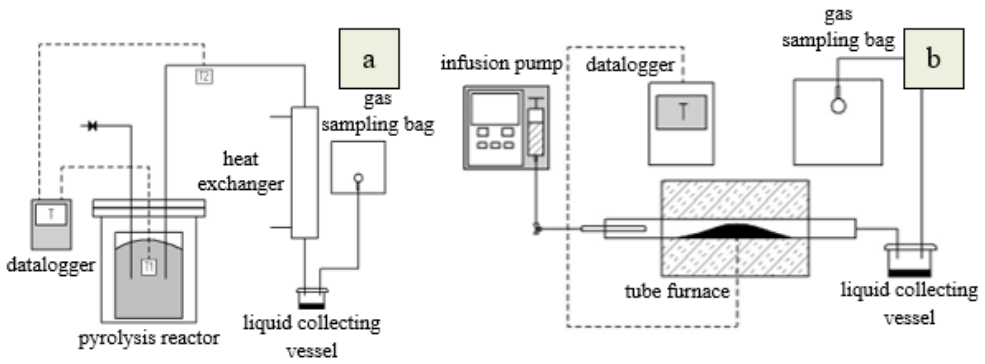

Figure 2

Laboratory pyrolysis (a) and gasification (b) systems

The resulting pyrolysis chars were then subjected to steam gasification at 900 °C for 1 h, with a heating rate of 10 °C min^{-1} and a steam flow rate of 5 cm^3 h^{-1}. These parameters were optimized in a prior study (Sebe et al., 2024). The steam activation of the chars was carried out in a laboratory gasification system, consisting of a tube furnace, a stainless-steel tube, and an infusion pump.

2.3. Adsorption experiments

The adsorption experiments were conducted using simulated phenol solutions with an initial concentration of 20 mg dm^{-3}. A total of 100 mg of activated carbon was added to 100 mL of the solution, and the mixtures were agitated on a reciprocal shaker. After 40 h, the mixtures were filtered, and the residual phenol concentrations were determined according to the ISO 6439:1990 standard titled, *"Water quality — Determination of phenol index — 4-Aminoantipyrine spectrometric method after distillation"*. Activated carbon from Thermo Fisher Scientific with a particle size of ≤ 2 mm and an iodine number of 969 mg g^{-1} was used as a reference point for the experimental evaluations.

The time required to reach adsorption equilibrium was determined using an initial solution concentration of 20 mg dm^{-3}. Pseudo-first-order (1) and pseudo-second-order (2) kinetic models were used to fit the data points.

$$q_t = q_e(1-e^{K_1 \cdot t}) \tag{1}$$

$$q_t = \frac{K_2 \cdot t \cdot q_e^2}{1+q_e \cdot K_2 \cdot t} \tag{2}$$

In these equations, q_e represents the equilibrium adsorption capacity (mg g^{-1}), q_t is the adsorption capacity at time t (mg g^{-1}), K_1 is the Lagergren first-order rate constant (1 min^{-1}), and K_2 is the Lagergren second-order rate constant (g min^{-1} mg^{-1}).

3. RESULTS AND DISCUSSION

3.1. Pyrolysis behavior of RDF mixtures

The first step in the preparation of activated carbons was the pyrolysis of RDF mixtures. After each pyrolysis experiment, the weight of the produced chars was measured. Typically, during the degradation of most plastics, the predominant product is oil, resulting in less char compared to cellulosic and lignocellulosic materials. Consequently, increasing the plastic content of the RDF leads to a decrease in the amount of char produced. In this instance, the reduction occurred from 29.6 ±0.1 to 24.6 ±0.5 wt.%.

The composition of the gases produced during the carbonization process was analyzed by using a gas chromatograph capable of identifying hydrogen, carbon monoxide, methane, carbon dioxide, ethene, and ethane. Figure 3 illustrates the variation

of gas composition during pyrolysis of the experimental RDF blends as a function of the total PP, PS and HDPE content (27.5–47.5 wt.%) of the RDF.

With this method, 71.0–76.6 vol.% of the gases was identified, while the remaining portion possibly consisted of other hydrocarbons. Since the polymeric components of the RDF, apart from the additives, consist primarily of carbon and hydrogen atoms, increasing the plastic content in the RDF mixtures predictably resulted in a higher proportion of hydrocarbons in the produced gas. In contrast, increasing the proportion of cellulosic and lignocellulosic components in the RDF led to a greater presence of oxygen-containing gas components, such as CO_2.

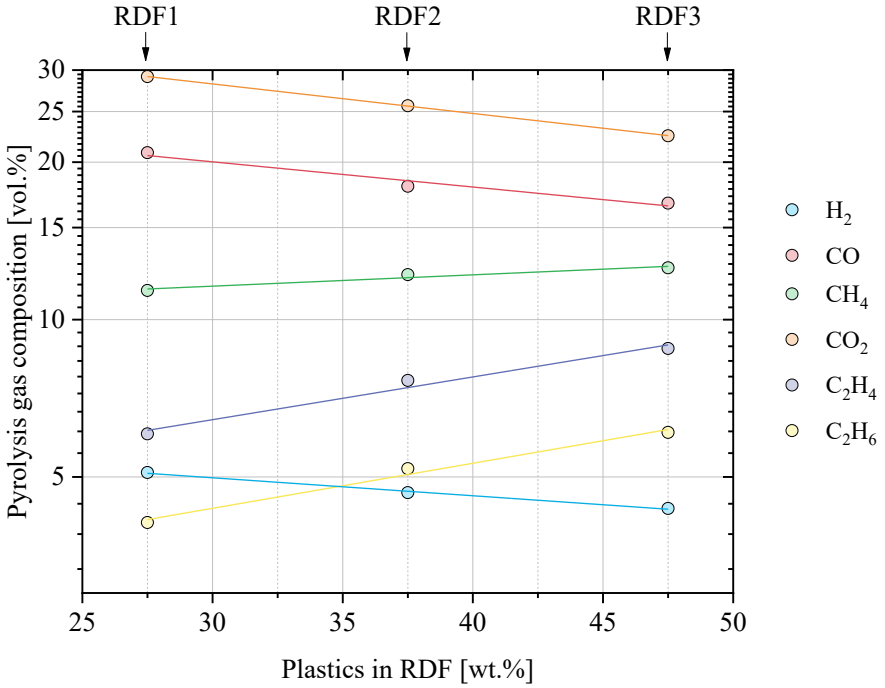

Figure 3
Composition of pyrolysis gases

Due to a significant portion of the produced gas remaining unidentified, it was not possible to accurately calculate its heating value. However, the trends shown in Figure 3 indicate that a higher plastic content in the RDF correlates with an increase in the heating value of the produced gas.

The results of experiments performed with a fixed PP:PS:HDPE ratio of 1:1:3 showed a linear relationship between the amount of plastic in the RDF and the proportion of each pyrolysis gas component. This linear relationship was strongest for H_2 ($R^2 = 0.995$) and CO_2 ($R^2 = 0.999$), and weakest for CH_4 ($R^2 = 0.952$), according to the coefficients of determination, R^2 values.

3.2. Characterization of RDF-based activated carbons

Table 2 presents the ultimate analysis of the RDF1-3 activated carbon samples. The most notable difference is observed in the carbon content, which increases as the ratio of plastic components in the initial RDF mixture increases.

Table 2

Ultimate analysis of activated RDF-chars [wt.%]

Sample	RDF1	RDF2	RDF3
Ultimate analysis (wt.%)			
C	48.4	51.5	53.4
H	1.1	1.1	1.2
N	<0.3	<0.3	<0.3
S	<0.2	<0.2	<0.2
O (by diff.)	0.0	0.0	0.0
Ash	50.5	47.4	45.4
LHV (kJ kg-1)	16636.0	16814.9	17956.2

Nitrogen physisorption measurements were performed under isothermal conditions, and the resulting adsorption and desorption isotherms are depicted in Figure 4, revealing distinct hysteresis loops. These loops are common in materials with mesopores and indicate capillary condensation (Das et al., 2024). According to the International Union of Pure and Applied Chemistry (IUPAC) classification, an H3-type loop can be seen here, which suggests slit-shaped pores (Bläker et al., 2019).

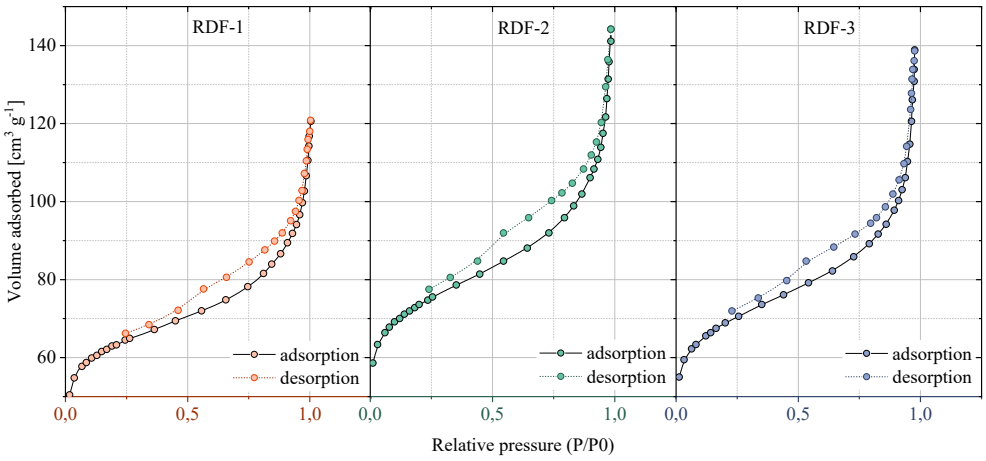

Figure 4

Adsorption and desorption isotherms of RDF chars

The gas adsorption analysis results are presented in Table 3. The specific surface area determined by the Brunauer–Emmett–Teller (BET) method, as well as the pore area and volume, reached their peak values for the RDF2 sample. This observation

aligns with findings from Adeniyi et al. (Adeniyi et al., 2024), who noted a synergy in biomass-plastic mixtures leading to the production of biochar with a higher specific surface area compared to biochar produced solely from biomass. It is possible that a similar synergy occurred in this study, suggesting that the optimal biomass-plastic ratio was achieved with RDF2.

Table 3

Gas adsorption analysis of RDF chars

Parameter	Unit	RDF1	RDF2	RDF3
BET, meas.	$m^2\ g^{-1}$	212.8	248.5	233.6
Total pore area	$m^2\ g^{-1}$	136.8	153.5	142.25
Total pore vol.	$m^3\ g^{-1}$	0.0631	0.0709	0.0658
Avr. pore diam.	nm	3.313	3.372	3.426

3.3. Phenol adsorption

The time dependence of phenol adsorption on RDF-based activated carbons was evaluated using an initial phenol concentration of 20 mg dm^{-3}. The results of adsorption experiments are presented in Figure 5. Increasing the initial plastic content of the RDF led to a corresponding increase in the adsorptive capacity of the resulting activated carbon.

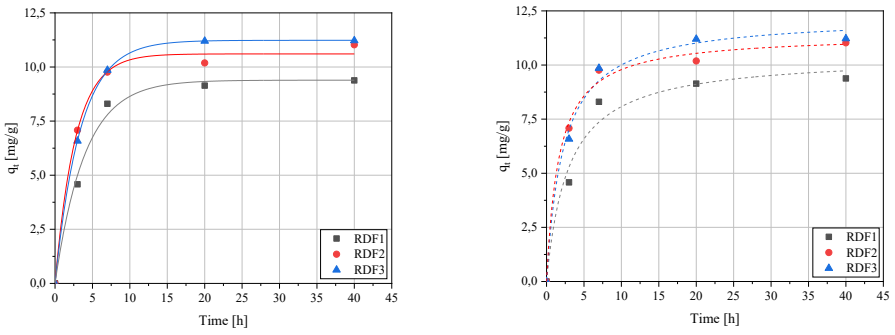

Figure 5

Time dependence of phenol adsorption on RDF-based activated carbons (PFO on the left and PSO on the right)

Table 4 summarizes the key parameters of the fitted pseudo-first order and pseudo-second order kinetic models. Based on the determination coefficient, the PFO model provided a better fit. Evaluating the adsorption efficiency of activated carbons derived from individual components, an estimated uptake capacity (q_{est}) was calculated for the RDF1–3 chars.

Table 4

Parameters of kinetic models fitted to the measurement points of RDF-based activated carbons

	Pseudo-first order			Pseudo-second order		
Par.	q_e	k_1	R^2	q_e	k_2	R^2
Unit	*mg/g*	*1/min*	–	*mg/g*	*mg/(g·min)*	–
RDF1	9.39 ±0.28	0.25 ±0.03	0.9903	10.45 ±0.76	0,03 ±0.01	0.9689
RDF2	10.60 ±0.23	0.37 ±0.03	0.9943	11.42 ±0.38	0,05 ±0.01	0.9920
RDF3	11.23 ±0.02	0.30 ±0.00	0.9999	12.25 ±0.48	0,04 ±0.01	0.9897

This estimation assumes no synergy between the components. Equation (3) outlines the calculation, where q_{est} represents the estimated value of phenol uptake capacity (wt.%), a_i (wt.%) denotes the ratio of the "i" component in the initial RDF mixture, r_i (wt.%) stands for the weight ratio of the remaining char during the pyrolysis of the "i" component, q_i (wt.%) indicates the uptake capacity of the activated carbon derived from component "i", and r_{RDF} (wt.%) represents the remaining char ratio of the RDF mixture.

$$q_{est}=\Sigma\frac{a_i \cdot r_i \cdot q_i}{r_{RDF} \cdot 100} \tag{3}$$

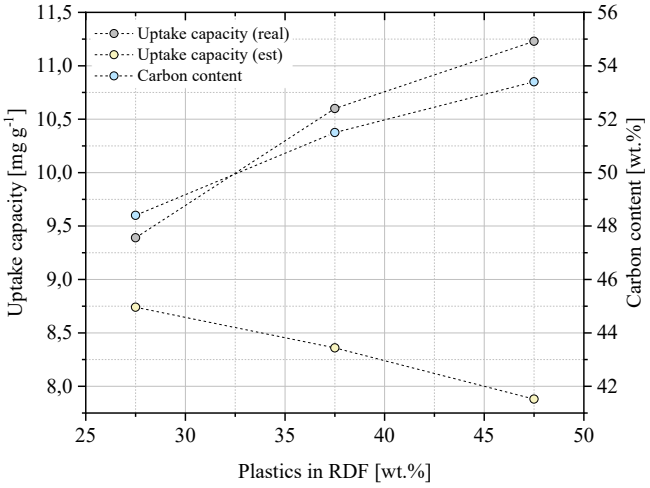

Figure 6

Estimated and real adsorption efficiency

This uptake capacity value specifically applies to the investigated conditions: a 20 mg dm^{-3} initial phenol concentration and a 1 : 1 (mg : mL) adsorbent-solution ratio.

Figure 6 compares the estimated and actual adsorptivity values, along with the carbon content, as a function of the total plastic content in the initial RDF blend. Contrary to expectations, an inverse trend was observed.

In other words, increasing the plastic content of the RDF resulted in improved adsorption efficiency. This could be due to a synergistic effect offered by the increasing presence of plastic in the RDF (Adeniyi et al., 2024). In the same conditions, the efficiency of RDF-based activated carbons is approximately 50–59% when compared to a commercial (Thermo Fisher) activated carbon. Unlike the specific surface area, the carbon content of the chars exhibited a stronger correlation with the uptake capacity. The surface area, pore size and carbon content all play crucial roles in the overall adsorptive capacity of activated carbons. Thus, the increasing adsorption efficiency trend from RDF1-3 could be attributed to factors such as the carbon content and average pore diameter rather than the surface area.

3.4. Examination of the by-product syngas

During the physical activation of the RDF-chars, an additional value-added product was generated, the synthesis gas. This gas was collected, and the composition analyzed using gas chromatography. The results of the gas analysis, along with the specific gas production, are presented in Figure 7. As the initial plastic content in the RDF blend increased, the overall gas production gradually decreased.

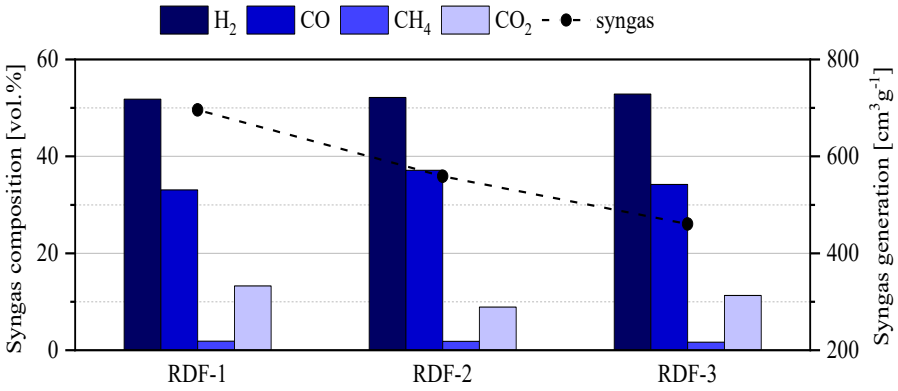

Figure 7
Quantity and composition of synthesis gas as a function of RDF composition

Approximately 89.4–94.0 vol% of the gases were identified. The effect of the initial RDF composition on gas production was less significant compared to its influence on the gas composition during pyrolysis. The analyzed syngas contained 47.1–48.7 vol.% H_2, 30.6–34.6 vol.% CO, 1.5–2.1 vol.% CH_4, and 9.1–10.2 vol.% CO_2. The total CO and H_2 contents, which are crucial components for further utilization in the chemical industry, varied between 77.8 and 83.3 vol%.

4. CONCLUSION

The utilization of municipal solid waste through thermochemical methods often encounters challenges due to its highly heterogeneous composition, influenced by various factors such as location, climate, and living standards. However, the conversion of this waste into refuse-derived fuel (RDF) offers a more manageable and uniform form for processing. Through appropriate high-treatment methods, the inherent unpredictability of RDF can be significantly reduced. Steam gasification presents a versatile approach, offering two potential directions depending on the desired end product: activated carbon or synthesis gas. This study focused on investigating the feasibility of preparing activated carbon from RDF and assessing the influence of RDF composition on product properties. The findings indicate that, within the examined compositional range, the produced chars exhibited approximately half the efficiency in phenol removal compared to high-quality commercial activated carbon. An increasing plastic content in the RDF mixture correlated with higher carbon content and adsorptivity of the activated carbons. Analysis of by-product gases produced after the pyrolysis process revealed minor fluctuations in syngas composition, with at least 77.8 vol.% total H_2 and CO content. These results are promising, considering that even if double the amount of these activated carbons is required, it can still be cost-efficient, given that the raw material is waste requiring treatment regardless.

ACKNOWLEDGMENTS

We acknowledge the support of the CIRCLETECH project (101079354) funded by the Horizon Europe programme of the European Commission.

REFERENCES

Adeniyi, A. G., Iwuozor, K. O., Emenike, E. C., Ajala, O. J., Ogunniyi, S., Muritala, K. B. (2024). Thermochemical co-conversion of biomass-plastic waste to biochar: a review. *Green Chem. Eng*., 5, pp. 31–49. https://doi.org/10.1016/j.gce.2023.03.002

Bläker, C., Muthmann, J., Pasel, C., Bathen, D. (2019). Characterization of Activated Carbon Adsorbents – State of the Art and Novel Approaches. *ChemBioEng Rev*., 6, pp. 119–138. https://doi.org/10.1002/cben.201900008

Cunha, F. S., Aguiar, A. P. (2014). Methods for the Removal of Phenolic Derivatives from Aqueous Effluents. *Rev. Virtual Quím*., 6. https://doi.org/10.5935/1984-6835.20140052

Das, D., Masek, O., Paul, M.C. (2024). Development of novel form-stable PCM-biochar composites and detailed characterization of their morphological, chemical and thermal properties. *J. Energy Storage*, 84, p. 110995. https://doi.org/10.1016/j.est.2024.110995

Heidarinejad, Z., Dehghani, M. H., Heidari, M., Javedan, G., Ali, I., Sillanpää, M. (2020). Methods for preparation and activation of activated carbon: a review. *Environ. Chem. Lett*., 18, pp. 393–415. https://doi.org/10.1007/s10311-019-00955-0

Hernández-Fernández, J., Lopez-Martinez, J., Barceló, D. (2021). Quantification and elimination of substituted synthetic phenols and volatile organic compounds in the wastewater treatment plant during the production of industrial scale polypropylene. *Chemosphere*, 263, p. 128027. https://doi.org/10.1016/j.chemosphere.2020.128027

Ke, P., Zeng, D., Wang, R., Cui, J., Li, X., Fu, Y. (2022). Magnetic carbon microspheres as a reusable catalyst in heterogeneous Fenton system for the efficient degradation of phenol in wastewater. *Colloids Surf. Physicochem. Eng. Asp*., 638, p. 128265. https://doi.org/10.1016/j.colsurfa.2022.128265

Ladányi, R. (2015). *Hejőpapi mechanikai-optikai előkezelő mű*.

Liu, B., Han, B., Liang, X., Liu, Y. (2024). Hydrogen production from municipal solid waste: Potential prediction and environmental impact analysis. *Int. J. Hydrog. Energy*, 52, pp. 1445–1456. https://doi.org/10.1016/j.ijhydene.2023.11.027

Sebe, E., Nagy, G., Kállay, A. A. (2024). Steam gasification of char derived from refuse-derived fuel pyrolysis: adsorption behaviour in phenol solutions. *Environ. Technol*., 45, pp. 5025–5036. https://doi.org/10.1080/09593330.2023.2283794

Thapar Kapoor, R., Treichel, H., Shah, M. P. (eds.) (2021). *Biochar and its Application in Bioremediation*. Springer Nature Singapore, Singapore. https://doi.org/10.1007/978-981-16-4059-9

Wang, Q., Shi, Y., Zhao, Y., Ning, P. (2022). Design of solvent mixtures for removal of phenol from wastewater using a non-linear programming model with a multi-start method. *Emerg. Contam*., 8, pp. 39–45. https://doi.org/10.1016/j.emcon.2021.11.001

Xayachak, T., Haque, N., Parthasarathy, R., King, S., Emami, N., Lau, D., Pramanik, B. K. (2022). Pyrolysis for plastic waste management: An engineering perspective. *J. Environ. Chem. Eng*. 10, 108865. https://doi.org/10.1016/j.jece.2022.108865

Geosciences and Engineering, Vol. 13, No. 1 (2025), pp. 18–31.
https://doi.org/10.33030/geosciences.2025.01.002

CRUSHED CONCRETE – QUALITY ISSUES OF CONCRETE RECYCLING

VIKTÓRIA GÁVEL[1,*], MÁRK KERTÉSZ[2], GÁBOR RADNAI[3]
[1,*]*CEMKUT Research & Development Ltd. for Cement Industry, Budapest, Hungary; dr.gavel.viktoria@gmail.com*
[2]*CEMKUT Research & Development Ltd. for Cement Industry, Budapest, Hungary; kerteszm@cemkut.hu*
[3]*CEMKUT Research & Development Ltd. for Cement Industry, Budapest, Hungary; radnaig@cemkut.hu*
[1]*https://orcid.org/0009-0009-0745-1780*

Abstract: Structural concrete is designed to last for decades, and when a concrete structure reaches the end of its life cycle, it must be recycled according to the principle of the circular economic approach. The presented results expand the knowledge required for the re-use of recycled concrete aggregates produced from crushed concrete in concrete and the re-use of recycled concrete fines as cement additive. They represent the importance of selective preparation technology and the role played by the material characteristics of crushed concrete in the development of certain properties of concrete. Knowledge of these relationships is essential, in order for crushed concrete to become a valuable product, instead of ending up as waste.

Keywords*: concrete recycling, recycled concrete aggregate, concrete durability, concrete fines, grindability of concrete*

1. INTRODUCTION

Concrete is actually an artificial stone. A composite material that traditionally consists of three components: aggregate (most often sanded gravel or crushed stone), cement and water. However, modern concrete can consist of up to five or six components. With admixtures, concrete additives (active or inert fine powders), fibers, etc. the properties of the concrete can be significantly influenced.

Due to its plasticity, versatile usability and durability, concrete has become the most used construction material in the world today, and after water, concrete is the second most used material. Commonly used concrete is designed to last at least 50 years, but the lifetime of more serious structures (bridges, tunnels, valley closing dams, marine structures, etc.) is more than hundred years.

When a building made of concrete reaches the end of its lifetime, it can be completely recycled with modern technologies available today. The processing of demolished concrete is very similar to that of natural aggregates: it is extracted, crushed and graded according to size (Figure 1). That's why concrete recycling is a perfect example of 'urban mining'. Based on its carefully examined characteristics, the field of use where these processed concrete wastes can be used as raw materials can be

determined. By recycling, the accumulation of concrete waste can be avoided and natural raw material sources can be protected.

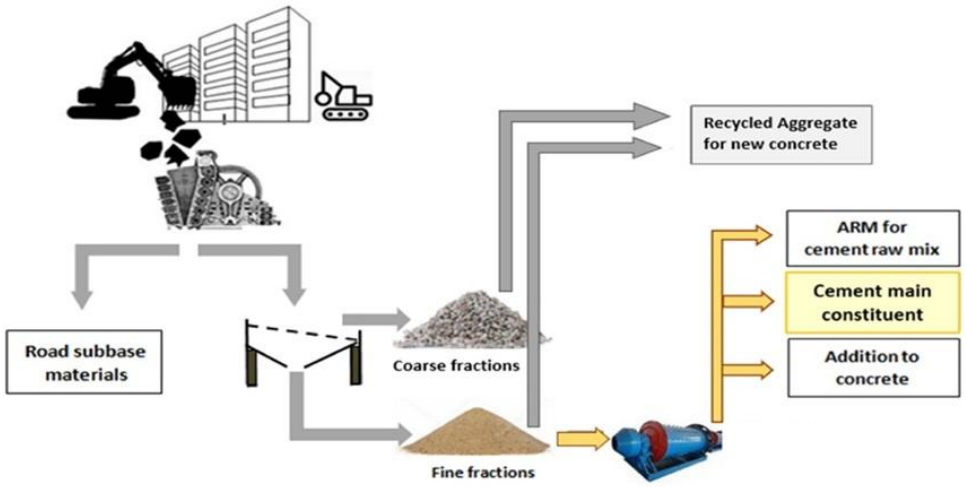

Figure 1

Recycling process of demolished concrete (CEN/TC 51 Document N 1500, 2021)

This approach, the idea of circular economy, waste reduction and more efficient use of resources have become basic requirements also in the construction industry, especially in the building materials industry (Marsh et al., 2022). Nowadays, there are no technical obstacles to the recycling of crushed concrete as aggregate and/or cement additive (Likes at al., 2022), we have sufficient experience (Rocha and Filho, 2023) and appropriate technical regulations (see the References: European standards signed EN, Hungarian national standard signed MSZ, Hungarian road technical specifications signed e-UT).

For decades, the construction industry has been striving for the largest possible proportion recycling of construction, demolition and construction material production waste, but this was not really successful for a long time because of the lack of guidance for concrete technologists that would have helped them to design the composition without a large number of mixes trialed.

Nowadays there are several technical guidelines and standards which prescribe the technical requirements of recycled concrete to use as concrete aggregate. European product standards for concrete aggregates (EN 12620+A1, EN 13139/AC, EN 13242+A1) also cover recycled aggregates from demolition waste and the Hungarian concrete standard (MSZ 4798) also contains limitations concerning the maximal proportion of recycled aggregate used in ready-mixed concrete but the technical specifications cannot give exact composition of these concrete mixtures because of the differences of original properties of concrete and because of the long-term environmental effects.

Despite detailed technical specifications, the rate of high-quality recycling of demolished concrete is still quite low (Rocha and Filho, 2023). In Hungary the majority of demolished concrete is placed in road sub-bases and landfills (OECD, 2023). However, with the increase in construction industry output, the amount of concrete waste increases, which, in contrast to gravel quarries, is mostly generated in densely populated areas where the greatest need for concrete use occurs. One of the reasons for the low rate of high-quality recycling is the misconception that concrete made from recycled aggregates has worse characteristics than concrete with conventional aggregates. The experiments presented here prove that with proper care, regular raw material tests and precise composition planning, concrete made with recycled aggregate can have the same or even better properties than concrete made with conventional additives. Moreover, if the natural sand and gravel additive with high transport costs can be replaced at least in part, then the cost of concrete production can be reduced in addition to protecting the environment.

However, there is another problem, the recycling of the fine (< 4 mm) part of crushed concrete. Coincidentally, to this, the EN 197-6 non-harmonized cement product standard offers an option. This standard allows the use of the fine fraction of crushed recycled concrete as a cement additive. Initial experiments aimed at determining the composition and technical parameters of cements containing concrete fines with appropriate quality and application properties are also in progress.

2. MATERIALS AND METHODS

The test materials were recycled aggregates from road concrete made with basalt aggregate, concrete paving stones and formwork elements produced with a laboratory jaw crusher and natural aggregates from eight Hungarian gravel quarries, as well as the concretes made with them (Figure 2).

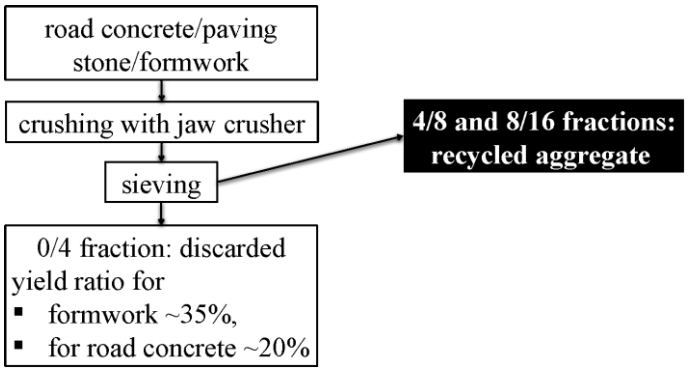

Figure 2
Production of experimental recycled aggregates

According to the technical specifications, only the part of the crushed concrete waste over 4 mm was used for concrete mixes as aggregate, classified into 4/8 and 8/16 fractions and 50 m/m% replacing the natural gravel fraction.

The following tests were performed on the crushed concrete and natural gravel fractions:

- particle density and water absorption according to EN 1097-6 standard;
- resistance to wear (micro-Deval test) according to EN 1097-1 standard;
- resistance to fragmentation (Los Angeles test) according to EN 1097-2 standard;
- resistance to freezing and thawing according to EN 1367-1 standard.

The test results of crushed concrete aggregates were compared with the average of the test results of natural gravel aggregates from eight different Hungarian quarries. Experimental concrete mixtures were prepared with crushed concrete aggregates from different types of concrete elements, which consisted of 50 m/m% natural gravel and 50 m/m% crushed concrete per fraction of aggregate over 4 mm. Concrete with recycled aggregate is commonly called re-concrete. The experimental concrete mixes were designed to have almost the same consistency (flow class F2), which was achieved by changing the amount of plasticizing admixture while maintaining the water/cement ratio of v/c = 0.55.

The composition of the experimental concrete mixtures was as follows:

- 325 kg of CEM II/A-S 42.5 N type Portland-slag cement
- 179 kg of water
- 896 kg of 0/4 aggregate fraction
- 573 kg of 4/8 aggregate fraction
- 386 kg of 8/16 aggregate fraction
- 50-100-110-120 g of plasticizing concrete admixture

Cube test specimens with an edge length of 150 mm were prepared from the experimental concrete mixes for compressive strength and freeze-thaw resistance tests according to the requirements of the relevant standards. The compressive strength test specimens were stored under water at 20 ±2 °C until they were 28 days old, and the freeze-thaw resistance test specimens were also stored under water at 20 ±2 °C for 7 days, then in a climate chamber (at 20 ±2 °C and relative humidity ≥ 95%) until the beginning of the test.

The compressive strength was tested according to the EN 12390-3 standard. The freeze-thaw with de-icing salts resistance test was carried out according to the reference method of CEN/TS 12390-9 technical specification, which is called scaling.
The structure of hardened re-concretes, namely the interface between the cement matrix and aggregate particles was also examined by optical microscopy (Keyence VHX-7000 digital microscope).

The fine fraction (< 4 mm) of recycled concrete made from natural gravel was aimed to be tested as cement additive. However, the 1-4 mm fraction was discarded because of its high content of quartz. It was 70.5% according to the XRD measurement and didn't meet the requirements of carbonate content in accordance with the EN 197-6 standard (see below). The experimental concrete fine was made of the original < 0.090 mm fraction and of the ground 0.090-1 mm fraction of crushed concrete (Figure 3).

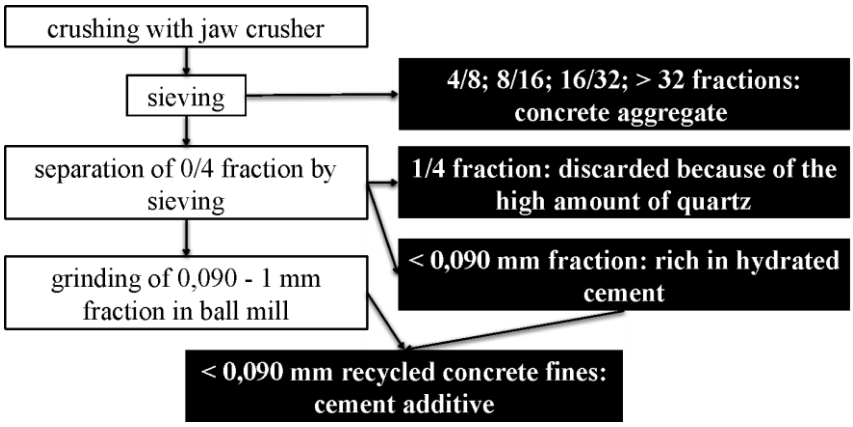

Figure 3
Production of concrete fines as cement additive

The yield ratio of concrete fines as cement additive was ~4.5 m/m%. Recycled concrete fine used for the experiments met the quality requirements in the relevant EN 197-6 standard:

- $R_{CU90} \geq 90$ m/m% concrete;
- total organic content (TOC) ≤ 0.8 m/m%;
- sulfate content (SO_3) ≤ 0.8 m/m%;
- clay content (methylene blue value) ≤ 1.20 g / 100 g;
- calcium carbonate ($CaCO_3$) ≥ 40 m/m%;
- sum of calcium carbonate and magnesium carbonate ($CaCO_3$+$MgCO_3$) ≥ 75 m/m%.

The grindability of the 0.090-1 mm fraction of crushed concrete was tested according to the Zeisel-method (Zeisel, 1953). Both (ground and non-ground) < 0.090 mm fractions of concrete fine were ground together to three different finenesses in laboratory ball mill without grinding aid and with TEA (triethanolamine). Experimental cements were made with ground concrete fines, 20 m/m% of them added to ordinary Portland cement (CEM I 42.5 N) and their standard strength on cement mortar was tested according to the EN 196-1 standard.

3. RESULTS

The differences between the three different types of concrete (road concrete, paving stones and formwork elements) were already evident during crushing and classification. The yield of fractions produced in the same way depends significantly on the composition, strength, and porosity of the original concrete. The profitability of recycling mostly depends on the energy spent on crushing and the yield ratio of the 0/4 fraction to be further treated, which in this case was the highest for the formwork stone (~35 m/m%) and the lowest for the road concrete (~20 m/m%) (Figure 2).

Of course, in the case of concrete with a heterogeneous composition, such as road concrete with crushed basalt aggregate, the crushed concrete fraction above 4 mm contained a much higher proportion of basalt fraction 11/22 than in the original concrete aggregate, and in addition, the different crushing technologies result different grain shapes, which affect the properties of both fresh and hardened concrete.

3.1. Results of aggregates

As expected, crushed concrete aggregates have lower particle density than natural gravel (Figure 4), which mostly consists of low-porosity quartz grains and fragments of volcanic rocks. It is also reflected in the results of water absorption of aggregates (Figure 5).

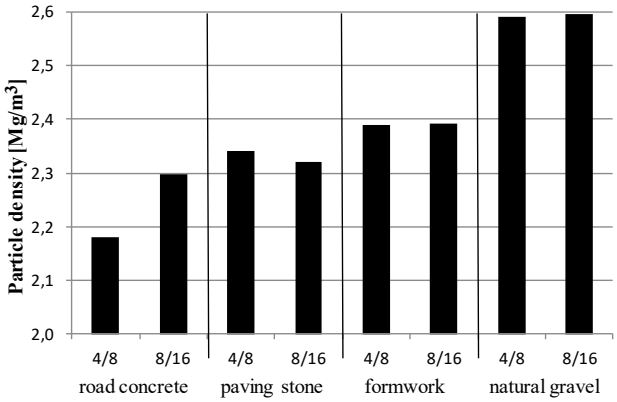

Figure 4
Particle density of different recycled concrete and natural gravel aggregate fractions

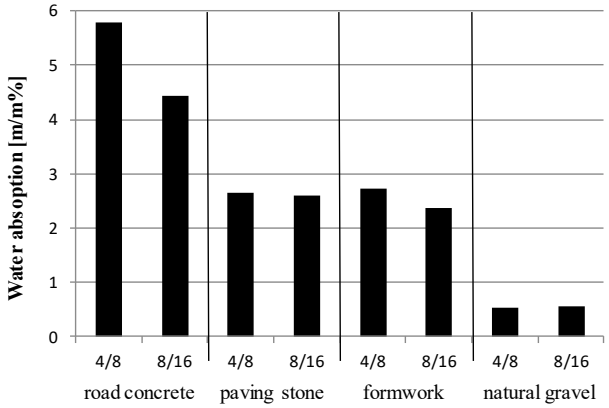

Figure 5
Water absorption of different recycled concrete and natural gravel aggregate fractions

The resistance to wear and fragmentation of the crushed, recycled concrete aggregate was worse than that of the harder natural quartz gravel (Figure 6).

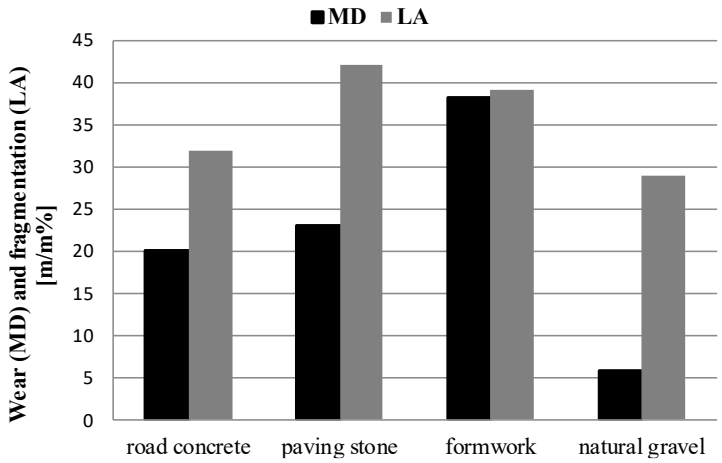

Figure 6

Mechanical properties of different recycled concrete aggregates and natural gravel

As a result, the recycled aggregates are not suitable for use as the wear layer of roads and paving and their use is also not recommended for making high-strength concrete. Concerning freeze-thaw, only the recycled aggregate made of formwork elements had extremely bad results (Figure 7), that's why, it is not recommended for making concrete with requirement of freeze-thaw resisting.

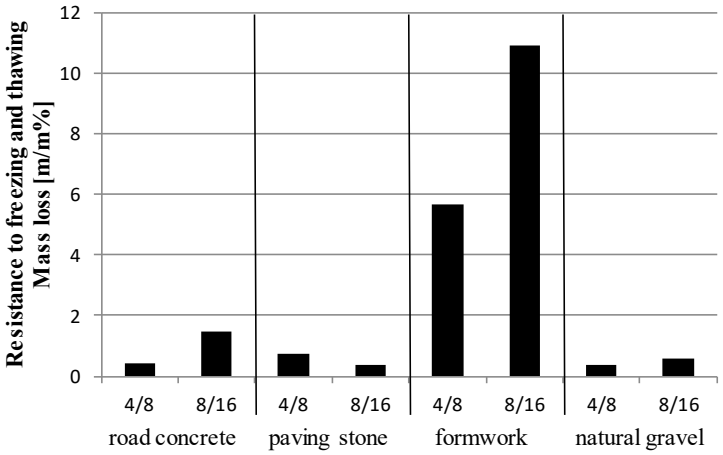

Figure 7

Weathering properties of different recycled concrete and natural gravel aggregate fractions

3.2. Results of concretes

The properties of both fresh and hardened concretes were examined, from which only the most important ones are presented here.

In the case of using crushed, recycled concrete as an aggregate, due to its significantly higher water absorption, in order to achieve the planned consistency of the fresh concrete, it is necessary to use a higher w/c ratio or to use a larger amount of plasticizing admixture (Figure 8).

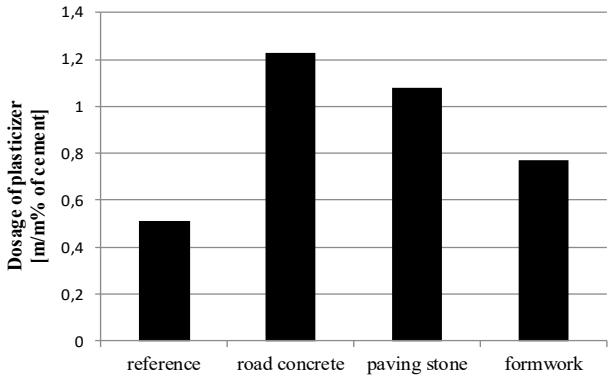

Figure 8

Demand of plasticizing admixture to the same consistency of re-concretes and reference concrete

Figure 9 shows the average compressive strength at the age of 28 days of experimental concretes made with a gravel fraction and different types of crushed concrete aggregates (50-50 m/m%), and the reference concrete made with only natural gravel aggregates.

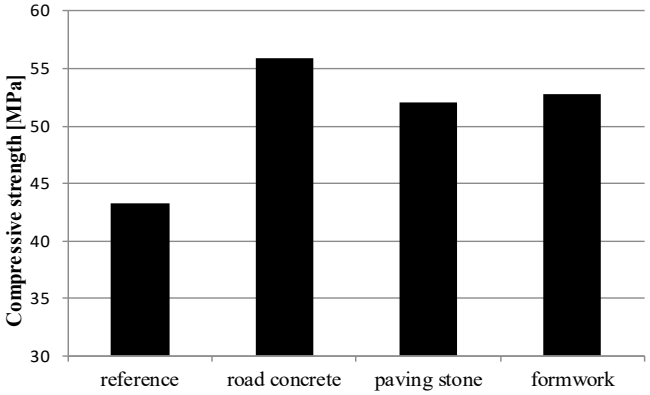

Figure 9

Compressive strength of the re-concretes made with 50 m/m% recycled concrete aggregate and the reference concrete without recycled concrete aggregate

The compressive strength of all experimental concretes was higher than that of the reference concrete, which, by the way, contained only natural gravel aggregate with higher particle strength based on its resistance to wear and fragmentation. In the case of the test specimens made with crushed concrete containing basalt, we measured a significant strength increase of almost 30% compared to the reference concrete.

Figure 10 shows the structure of re-concretes with different recycled concrete aggregates.

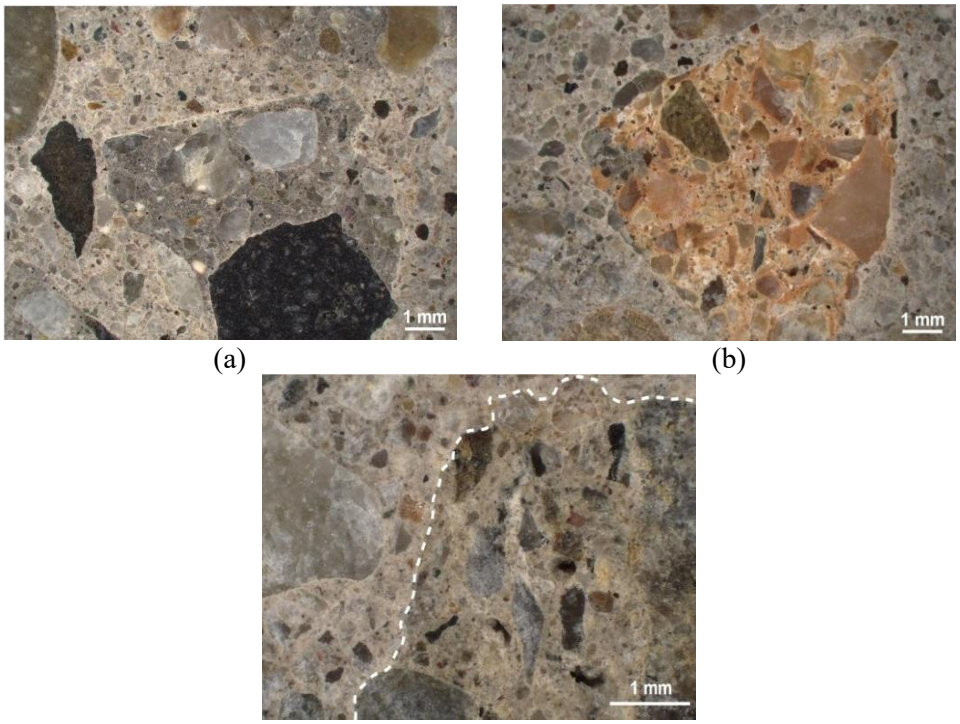

(a) (b)

(c)

Figure 10

Microscopic images of concretes made with different recycled concrete aggregates a) road concrete, b) paving stone, c) formwork element

Compared to natural gravel, crushed concrete particles come into contact with the cement paste on a larger surface area. It must be considered when calculating the necessary paste content of concrete. During crushing, the concrete waste broke along the cracks and weak joints, cracks inside the grains were not typical.

These results indicate that the size of the surface of the aggregate binding to the cement paste plays an important role in the development of the compressive strength of concrete.

Figure 11 shows the results of the freeze-thaw test (the specific amount of material scaled from the surface exposed to the salt solution during freezing) of the re-

concretes made using different types of crushed concrete aggregates (50 m/m% in the gravel fraction) and the reference concrete after 7, 14, 21 and 28 freeze-thaw cycles (days).

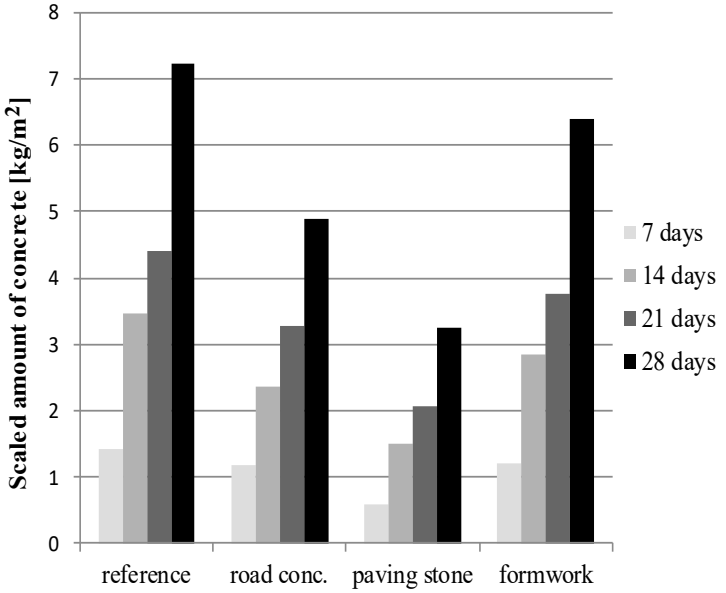

Figure 11
Freeze-thaw resistance of the re-concretes made with 50 m/m% recycled concrete aggregate and the reference concrete without recycled concrete aggregate

Air entraining admixture, which is required for freeze-thaw resistant concrete, was not added to the concrete mixtures, so it was expected that none of the concretes would meet the requirements of the standards. However, it is clear from the test results that the crushed road concrete and paving stones (which were originally designed to be freeze-thaw resistant) significantly improved the freeze-thaw resistance of the experimental concretes made with them compared to the reference.

3.3. Results of concrete fines as cement additive

As it was already mentioned, according to the currently valid technical specifications, the use of fine (< 4 mm) recycled concrete as aggregate is not allowed in Hungary. But fortunately, there is another possibility, thanks to a new European cement standard issued 2023: the non-harmonized product standard of cements with recycled building materials (EN 197-6:2023). The quality requirements of recycled concrete fines are quite similar to that of limestone cement additive.

However, there is an important difference between concrete fines and limestone, namely their grindability. Based on the results of grindability tests according to the

the Zeisel-method, concrete fines need three times more energy to reach a common cement fineness than does limestone (Figure 12).

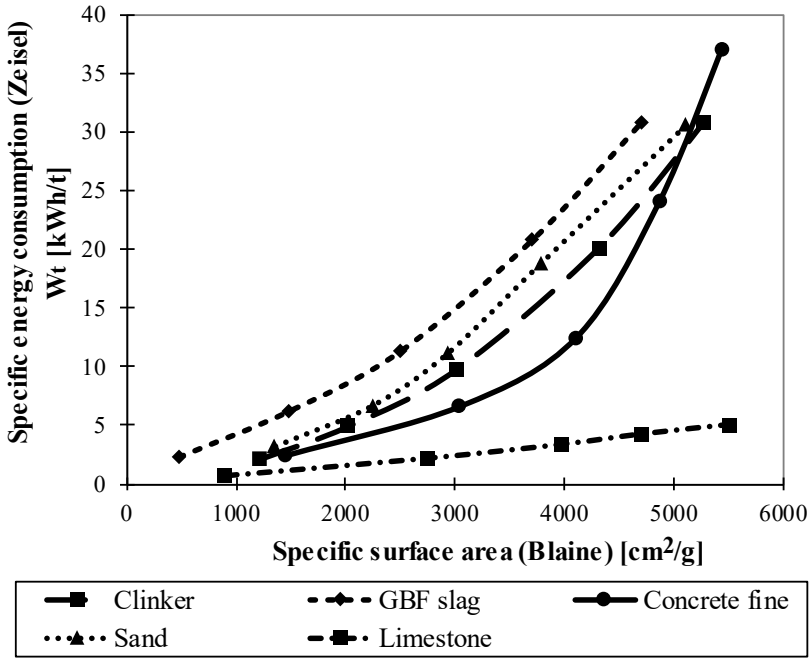

Figure 12
Grindability of recycled concrete fines and different raw materials of cement/concrete

For further experiments, the concrete fine was ground to three different finenesses in a laboratory ball mill without grinding aid (F01 and F02) and with TEA (F03). According to the grinding experiments, with the use of grinding aid (TEA) the agglomeration of concrete fines can be reduced and its fineness can be increased (Table 1).

Table 1
Finenesses of ground recycled concrete fines as cement additive

Mark	Grinding in ball mill	Specific surface area (Blaine) [cm^2/g]
F01	to a common cement fineness	~4200
F02	until agglomeration	~5700
F03	added grinding aid	~7700

Laboratory cements (K01, K02, K03) were made with of the ground concrete fines at 20 m/m% being added to ordinary Portland cement (K00) and their standard strength on cement mortar at the age of 28 days was tested. The test results show that

the concrete fines decreased the compressive strength compared to that of the reference cement, yet all cements still met the requirements of standard strength according to the relevant standard (Table 2).

Table 2

Standard compressive strength of cements with ground recycled concrete fines as cement additive (separate grinding)

Mark	Composition	Compressive strength (28 days) [MPa]	Loss of strength [%]
K00	100% CEM I 42.5 N	61.10	–
K01	80% K00 + 20% F01	54.56	10.7
K02	80% K00 + 20% F02	55.40	9.3
K03	80% K00 + 20% F03	59.16	3.2

The negative effect of concrete fines additive on compressive strength of cement can be moderated by increasing the grinding fineness of the recycled concrete fines.

For emphasizing the importance of separate grinding of concrete fines Table 3 shows our earlier results of laboratory cements made with 20 m/m% of limestone by co-grinding to different fineness (Gável, 2024).

Table 3

Standard compressive strength of laboratory cements without limestone and with 20 m/m% of limestone (co-grinding)

Specific surface area (Blaine) [cm^2/g]	Compressive strength (28 days) [MPa]		Loss of strength [%]
	100% clinker	80% clinker + 20% limestone	
3000	50.6	37.3	26.28
3500	53.8	40.0	25.65
4000	57.6	44.8	22.22

It is clear that not only the grinding fineness of the cement but rather the fineness of cement components, i.e. the fraction composition and the particle size distribution of the cement are decisive for its compressive strength. Separate grinding is more suitable for adjusting the proper grinding fineness of cement components that has also a significant effect on the applicable properties of cement and on the durability of concrete. Further tests of recycled concrete fines as cement additives, that concern especially long-term durability tests, are also the focus of our research. Those results are the subject of a future article.

4. DISCUSSION AND CONCLUSIONS

Our test results indicate that, in addition to the physical characteristics of aggregates laid down in the technical specifications, it is advisable to carry out additional raw

material tests before using recycled concrete as aggregate. These characteristics fundamentally influence the properties of fresh and hardened concrete, and by knowing them, it is possible to design a concrete mixture composition that can have more favorable properties than concrete that does not contain recycled concrete.

These results also draw attention to the importance of knowledge of the types of recycled concrete aggregate (crushed concrete) and of original concrete waste constituents and their limitations before use. In general, demolished concrete structures or manufacturing scrap can be used as recycled concrete aggregates, especially if they have been selectively demolished and stored.

Satisfying these technical requirements is the task of the producers of recycled concrete aggregates, who, when choosing the required crushing machine, must pay attention to the fact that different crushing technologies result in different grain shapes, which significantly affects the properties of both fresh and hardened concrete. In addition, efforts must currently be made to minimize the amount of the 0/4 fraction that cannot be used as a concrete filler. In this regard, it should be noted that the new EN 197-6 European cement product standard published in August 2023 offers the opportunity to use the fine part of recycled concrete waste (0/4 fraction) as a cement additive. Cement with recycled concrete fines can have a similar compressive strength as an ordinary Portland cement, but in this case grindability of crushed concrete has to be taken into consideration! Despite of these promising results, we cannot expect the mass appearance of these new types of cements in the near future, because as far as we know, suitable concrete fines are not yet widely available in industrial quantities, and the experiments establishing the bases for the production of these cements and the concrete technology tests that facilitate their practical use are still in their initial stages.

REFERENCES

CEN/TC 51 Document N 1500 (2021). CEN, Bruxelles.

CEN/TS 12390-9 (2016). Testing hardened concrete – Part 9: Freeze-thaw resistance with de-icing salts – Scaling, CEN, Bruxelles.

EN 196-1 (2016). Methods of testing cement – Part 1: Determination of strength, CEN, Bruxelles.

EN 197-6 (2023). Cement – Part 6: Cement with recycled building materials, CEN, Bruxelles.

EN 1097-1 (2023).. Tests for mechanical and physical properties of aggregates – Part 1: Determination of the resistance to wear (micro-Deval), CEN, Bruxelles.

EN 1097-2 (2020). Tests for mechanical and physical properties of aggregates – Part 2: Methods for the determination of resistance to fragmentation, CEN, Bruxelles.

EN 1097-6 (2022). Tests for mechanical and physical properties of aggregates – Part 6: Determination of particle density and water absorption, CEN, Bruxelles.

EN 1367-1 (2007). Tests for thermal and weathering properties of aggregates – Part 1: Determination of resistance to freezing and thawing, CEN, Bruxelles.

EN 12390-3 (2019). Testing hardened concrete. Part 3: Compressive strength of test specimens, CEN, Bruxelles.

EN 12620+A1 (2008). Aggregates for concrete, CEN, Bruxelles.

EN 13139/AC (2004). Aggregates for mortar, CEN, Bruxelles.

EN 13242+A1 (2007). Aggregates for unbound and hydraulically bound materials for use in civil engineering work and road construction, CEN, Bruxelles.

e-UT 05.01.15 (2018). Aggregates for road construction, Hungarian Public Road Non-profit Ltd., Budapest,

e-UT 05.02.31 (2008). Road concrete making with reuse of recycling concrete, Hungarian Public Road Non-profit Ltd., Budapest,

Gável, V. (2024). CEM II/B-LL: a mészkőtartalmú, klímabarát cementek értékei – 2. rész (Values of the limestone containing, climate-friendly cements – Part 2). *Beton*, 32 (3), pp. 12–15, Available online: https://www.betonujsag.hu/userfiles/lapszam/285/pdf/beton_ujsag_2024_03_web.pdf (accessed on 1 December 2024)

Likes, L., Markandeya, A., Haider, M., Bollinger, D., McCloy, J.S., Nassiri, S. (2022), Recycled concrete and brick powders as supplements to Portland cement for more sustainable concrete. *Journal of Cleaner Production*, 364, p. 132651. https://doi.org/10.1016/j.jclepro.2022.132651

Marsh, A.T.M., Velenturf, A.P.M., Bernal, S.A. (2022), Circular Economy strategies for concrete: implementation and integration. *Journal of Cleaner Production*, 362, p. 132486. https://doi.org/10.1016/j.jclepro.2022.132486

MSZ 4798 (2016). Concrete. Specification, performance, production, conformity, and rules of application of EN 206 in Hungary, MSZT, Budapest.

OECD (2023), *Towards a National Circular Economy Strategy for Hungary*, OECD Publishing, Paris. https://doi.org/10.1787/1178c379-en

Rocha, J. H. A., Filho, R. D. T. (2023). *The utilization of recycled concrete powder as supplementary cementitious material in cement-based materials: A systematic literature review*, *Journal of Building Engineering*, 76, p. 107319. https://doi.org/10.1016/j.jobe.2023.107319

Zeisel, H. G. (1953). *Schriftenreihe der Zementindustrie, Heft 14*. Düsseldorf, VDZ e.v.

Geosciences and Engineering, Vol. 13, No. 1 (2025), pp. 32–44.
https://doi.org/10.33030/geosciences.2025.01.003

INVESTIGATIONS OF THE SUITABILITY OF K-FELDSPAR MODIFIED BY MILLING FOR CO_2 SEQUESTRATION

MARCELA ACHIMOVIČOVÁ[1, *], ERIKA TÓTHOVÁ[2], MATEJ BALÁŽ[3] ANTON ZUBRIK[4], MURAT ERGEMOGLU[5], MUSTAFA BIRINCI[6], SEMA ERGEMOGLU[7], HIKMET SIS[8], PETER BALÁŽ[9]

[1, 2, 3, 4, 9, *] *Institute of Geotechnics, Slovak Academy of Sciences, Slovakia*
[5, 6, 7, 8] *Mining Engineering Department, Inönü University, Türkiye*
[1]*https://orcid.org/0000-0002-0533-8866 (achimovic@saske.sk)*
[2]*https://orcid.org/0000-0001-6202-0371 (etothova@saske.sk)*
[3]*https://orcid.org/0000-0001-6563-7588 (balazm@saske.sk)*
[4]*https://orcid.org/0000-0002-2176-0549 (zubant@saske.sk)*
[5]*https://orcid.org/0000-0003-2922-7965 (murat.erdemoglu@inonu.edu.tr)*
[6]*https://orcid.org/0000-0002-1954-7837 (mustafa.birinci@inonu.edu.tr)*
[7]*https://orcid.org/0000-0002-0119-1596 (sema.erdemoglu@inonu.edu.tr)*
[8]*https://orcid.org/0000-0001-8840-5448 (hikmet.sis@inonu.edu.tr)*
[9]*https://orcid.org/0000-0002-7089-7437 (balaz@saske.sk)*

Abstract: Nowadays, carbon dioxide (CO_2) emissions are one of the main factors of global warming and climate change. Controlling CO_2 levels in the atmosphere and limiting global warming requires urgent action. Some minerals can be used to capture and store CO_2 from the air or other sources. Mechanochemically modified K-feldspar (with KOH, $Ca(OH)_2$, and CaO) was used for *ex situ* and *in situ* CO_2 capture. In the *ex situ* experiment (in a thermoanalytical apparatus at 150 °C, 5 h), infrared spectroscopy indicated that mechanochemically modified K-feldspar was capable of CO_2 sequestration via carbonate formation. The *in situ* CO_2 capture experiment consists of two steps. The first step involved the mechanochemical modification of K-feldspar using $Ca(OH)_2$ and CaO as additives during milling. The second step consisted of direct *in situ* CO_2 sequestration in the milling chamber. X-ray diffraction patterns demonstrated the formation of the calcite phase, and thermal analysis confirmed the decomposition of such created calcite. Elemental analysis has found the binding of approximately 1.6% of carbon, and 5.23 % carbonation ratio of modified feldspar was achieved. In addition, the use of the mineral vermiculite as a natural additive for *in situ* sequestration of K-feldspar was investigated using the above-mentioned analytical techniques.

Keywords*: K-feldspar, vermiculite, mechanochemical modification, milling, CO_2 sequestration, mechanochemical carbonation*

1. INTRODUCTION

It is well-known that CO_2 is the most abundant of the greenhouse gases and is, therefore, the largest contributor to the greenhouse effect. In the last decade, the need and various activities to reduce CO_2 emissions to pre-industrial levels have greatly intensified (What is carbon neutrality and how can it be achieved by 2050?, [Online]).

Mineral carbonation is a natural weathering process in which alkaline earth metals, mainly Ca and Mg react with CO_2 to form stable carbonates. These reactions are exothermic, but in nature, they take place slowly during the weathering of silicate minerals (Pachauri and Reisinger, 2007; Seifritz, 1990). O'Connor and coworkers (2002) developed an aqueous process of direct carbonation of silicate minerals (olivine, serpentine, enstatite) using pressure and temperature above 150 °C as a method for CO_2 storage in solid form. Wang et al. (2014) studied carbonation using natural K-feldspar calcined with phosphogypsum. The first attempts to use mechanical activation (high-energy milling) of various silicate minerals for CO_2 sequestration were performed already 20 years ago (Kalinkin et al., 2003, 2004; Kalinkina et al., 2001a, b). Later, Turianicová and coworkers (2013a, 2014) investigated the carbonation of olivine and vermiculite using mechanical activation. It is known from the literature that mechanical activation causes particle comminution, increases the specific surface area of the minerals and even breaks their crystal structure by the formation of lattice defects, which increases their overall reactivity in subsequent reactions (Baláž, 2008).

K-feldspar, a mineral with the specific composition $KAlSi_3O_8$, is a member of the aluminosilicate group. It is widely distributed and abundant in various regions worldwide, including China and Türkiye. Its unique properties make it a significant resource for various industries such as ceramic. Additionally, K-feldspar minerals are emerging as potential candidates for carbon dioxide (CO_2) capture (Guo et al., 2015). For intensification of its carbonation process various additives such as gypsum - $CaSO_4 .2\ H_2O$ or $CaCl_2$ slag were used (Wang et al., 2014; Ye et al., 2014). In order to initiate the chemical reaction of refractory K-feldspar and to introduce alkaline earth metal K or Ca into its crystal structure by mechanochemical modification, it could be used as a milling additive KOH, $Ca(OH)_2$ or CaO respectively in the process of studying CO_2 capture. Vermiculite, a natural silicate mineral with the chemical formula $(Mg,Fe,Al)_3(Al,Si)_4O_{10}(OH)_2.4H_2O$, is another material used in carbon capture studies. It is inherently harmless and has a large specific surface area, high cation exchange capacity, and excellent chemical and mechanical stability. Due to the presence of exchangeable cations (K^+, Ca^{2+}, and Mg^{2+}) inherent to vermiculite, it has demonstrated utility in studies related to the adsorptions (Ma et al., 2024).

The aim of our study was to demonstrate the potential CO_2 sequestration strategies within mineral carbonation of abundant aluminosilicate K-feldspar. *Ex situ* and *in situ* capture of CO_2 on mechanochemically additive-modified K-feldspar during high-energy milling was elaborated, characterized and quantified.

2. MATERIALS AND METHODS

2.1. Materials

K-feldspar or microcline ore used as input material for the experiments was provided by Kale Seramik Company, Türkiye with the following chemical analysis: 70.87% SiO_2, 16.33% Al_2O_3, 10.6% K_2O, 1.99% Na_2O, 0.34% CaO, 0.15% Fe_2O_3, 0.14% BaO, 0.06% P_2O_5, 0.05% TiO_2, 0.04% MgO, 0.01% SrO. In Figure 1 the X-ray diffraction analysis

(XRD) showed in addition to K-feldspar or microcline ($KAlSi_3O_8$), quartz (SiO_2) and albite ($NaAlSi_3O_8$) as well.

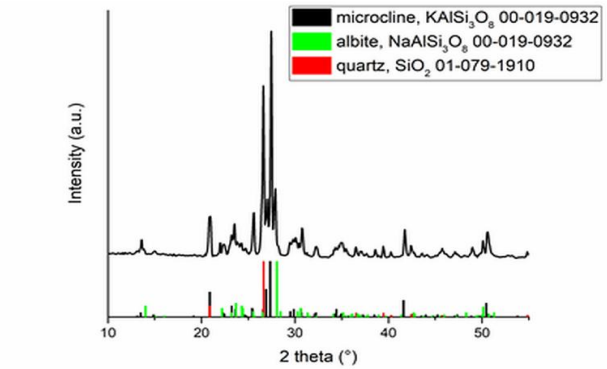

Figure 1

XRD pattern of as-received K-feldspar ore. Reprinted with permission from ref. (Baláž et al., 2024). Copyright 2024 Elsevier

The particle size d_{90}, d_{50}, and d_{10} values were 518, 293, and 121 μm, respectively. For mechanochemical modification of feldspar pure chemicals p.a. KOH (Centralchem, Slovakia), $Ca(OH)_2$, (Centralchem, Slovakia) and CaO (Sigma-Aldrich, USA) were used. Natural vermiculite $(Mg, Fe, Al)_3(Al, Si)_4O_{10}(OH)_2.4H_2O$ from Kuluncak (Malatya, Türkiye) has also been used as an additive to prepare K-feldspar/ vermiculite (F:V) composites.

2.1.1. Mechanochemical modification of K-feldspar

Mechanochemical modification of K-feldspar ore was performed in the laboratory planetary ball mill Pulverisette 6 (Fritsch, Germany) with the addition of 1 M of KOH, $Ca(OH)_2$ or CaO (Table 1) under the following conditions: volume of milling chamber-250 mL, loading of the mill-50 balls (10 mm in diameter), the material of milling chamber and balls- tungsten carbide, WC, the total mass of the milling charge-20.18 g, ball-to-powder ratio-20:1, milling atmosphere-air, rotation speed 600 rpm, and milling time 90 min (each cycle of milling lasting 30 min was followed by a cooling break of 15 min).

Table 1

The amounts of added materials for mechanochemical modification of K-feldspar by milling

Sample	Mass of feldspar [g]	Mass of added material + H2O [g]
Feldspar	20.18	–
Feldspar/KOH	16.79	3.39
Feldspar/$Ca(OH)_2$	15.94	4.24
Feldspar/$Ca(OH)_2$ wet	16.85	2.24 + 1.1
Feldspar/CaO wet	16.40	1.65 + 2.1

2.2. CO_2 sequestration of K-feldspar

2.2.1. Ex situ CO_2 sequestration

Mechanically activated K-feldspar and mechanochemically modified samples of K-feldspar with hydroxides KOH, and $Ca(OH)_2$ were subjected to *ex situ* sequestration using thermoanalytical apparatus STA 449 F3 Jupiter (Netzsch, Germany) under dynamic conditions in CO_2 (50 $cm^3.min^{-1}$) by heating up to 150 °C for 5 h.

2.2.2. In situ CO_2 sequestration

The mechanochemically modified samples of K-feldspar with $Ca(OH)_2$ and CaO according to the conditions in *2.1.1* were *in situ* sequestrated using laboratory planetary ball mill Pulverisette 6 (Fritsch, Germany) according to the following conditions: volume of milling chamber-250 ml, loading of the mill-50 balls (10 mm in diameter), the material of milling chamber and balls-tungsten carbide, WC, the total mass of the milling charge-20.18 g, the addition of 10.1 mL H_2O, ball-to-powder ratio-20:1, milling atmosphere-CO_2 (5 $L.min^{-1}$, 3 min flushing), rotation speed 450 rpm, and milling time 30 min.

For testing the sequestration potential of K-feldspar:vermiculite (F:V) composites, the same mill and milling balls (both number and diameter) as specified above were used. The overall sample mass was 18 g and the weight ratio between V and F was modified (namely as-received F and V, and their combinations in 80:20, and 60:40 ratios were used). Before milling, 9 mL H_2O was added and a milling atmosphere of CO_2 (5 $L.min^{-1}$, 3 min flushing) was used. The rotation speed was set to 450 rpm and the milling time was 30 min according to our previous experiments (Turianicová, 2009).

2.3. Characterization techniques

X-ray diffraction measurements (XRD) were carried out in the Bragg-Brentano geometry using a D8 Advance diffractometer (Bruker, Germany), working with CuK_α radiation. ICDD-PDF2 was used for phase matching.

Fourier-transform infrared (FT-IR) spectra were measured using the Tensor 29 (Bruker, Germany) in the frequency range of 4000–400 cm^{-1} with the KBr pellet method. KBr was dried before the analysis at 100 °C for 1 h.

Thermogravimetric measurements were carried out using STA 449 Jupiter thermal analyzer (Netzsch, Germany) coupled with a QMS 430C Aëolos mass spectrometer (Netzsch, Germany). The measurements were performed at steady airflow from 45 °C up to 1000 °C with a heating rate of 10 °C/min. Changes in the sample weight and m/z signals [m/z = 18 (H_2O) and m/z = 44 (CO_2)] were constantly monitored.

The elemental analysis (CHNS) was performed by elementary analyser Vario MACRO cube (Elementar Analysensysteme GmbH, Germany) using a thermal conductivity detector. Helium (purity 99.995%, intake pressure 2 bar) was chosen as the carrier gas in all analyses. The purity of oxygen for combustion was 99.995% with an intake pressure of 2 bar A combustion tube was set up at 1150 °C and a reduction

tube at 850 °C. Sulphanilamide (C = 41.81%, N = 16.26%, H = 4.65%, S = 18.62%) was used as the CHNS standard.

CO_2 mineralization ratio or mechanochemical carbonation ratio was calculated according to literature (Shangguan et al. 2016) based on the weight loss of the *in situ* sequestered mechanochemically modified feldspar samples with $Ca(OH)_2$ and CaO after calcination in a muffle furnace. The calculation was performed according to the formula:

$$CO_2\ carbonation\ ratio\ (\%) = \frac{M_2 - M_3}{M_1} \times 100 \quad (1)$$

where M_2 and M_3 are masses of 1 h calcinated samples at 400 °C and 800 °C respectively, and M_1 is the mass of the sample before calcination.

3. RESULTS

3.1. *Ex situ* sequestration of mechanochemically modified K-feldspar with hydroxides

The first *ex situ* CO_2 capture tests using mechanically activated K-feldspar without modification were unsuccessful. Therefore, the K-feldspar was subjected to mechanochemical modification with the addition of KOH and $Ca(OH)_2$ in order to break the K-feldspar crystal structure and/or create new phases e.g. $Al(OH)_3$, $CaAl_2Si_3O_{10}$ that would be able to capture CO_2 gas. By evaluating the XRD patterns (see Figure 2) of such modified K-feldspar was found, that during 90 min of milling, only the amorphization of K-feldspar/microcline and albite phases was detected and no new phases were formed when performing milling under neat conditions with both KOH and $Ca(OH)_2$. In the case of milling with KOH, and $Ca(OH)_2$ with H_2O (wet), a WC phase appeared originating from the wear of the milling chamber and balls.

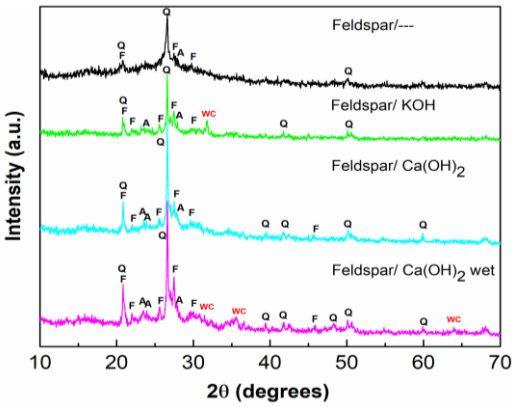

Figure 2

XRD patterns of mechanically activated K-feldspar and mechanochemically modified K-feldspar with KOH and $Ca(OH)_2$. F - $KAlSi_3O_8$, A- $NaAlSi_3O_8$, Q - SiO_2, WC – tungsten carbide

The experimental process of *ex situ* CO_2 sequestration of mechanically activated K-feldspar and mechanochemically modified samples has been carried out according to the conditions in part *2.2.1*. The course of the process is visualized in Figure 3 where TG and DTA curves can be seen. The curves revealed that at the beginning of the experiment, a slight weight increase was observed in the case of K-feldspar/ KOH and K-feldspar/$Ca(OH)_2$ mixtures. This increase in weight might be due to the carbonation process; however, no other effects were detected.

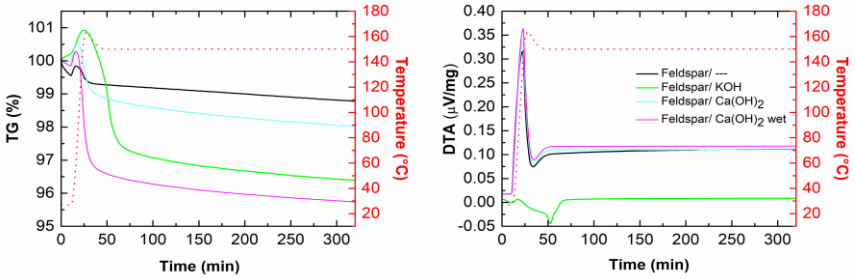

Figure 3

TG and DTA curves of mechanically activated K-feldspar (black line) and mechanochemically modified K-feldspar with KOH and $Ca(OH)_2$ during ex situ CO_2 sequestration

FTIR spectroscopy as another sensitive method for demonstrating CO_2 capture was used. The FT-IR spectra of the samples modified with KOH, $Ca(OH)_2$ under dry and wet conditions after CO_2 exposure in Figure 4 showed evidence of CO_2 binding and carbonate phase formation in all three cases, which can be determined by the peak in the wavenumber region of 1600-1300 cm^{-1}, characteristic for CO_3^{2-} vibrations (Nakamoto 2008). The bands attributed to the carbonate group can be observed as a single or double peak in the range of 1350–1565 cm^{-1}. It was found that peak splitting or merging is related to the alkaline metal with which CO_2 is combined (Turianicová et al. 2013b).

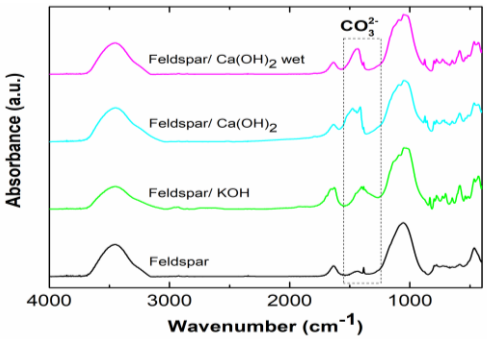

Figure 4

FT-IR spectra of mechanically activated K-feldspar (black line) and mechanochemically modified K-feldspar with KOH and $Ca(OH)_2$ after ex situ CO_2 sequestration

The same behaviour was not detected in the case of unmodified K-feldspar. It means, that probably $CaCO_3$ and K_2CO_3 were formed during mentioned conditions in the case of K-feldspar modified with KOH and $Ca(OH)_2$. However, we assume that the binding of CO_2 proceeds only due to the presence of KOH and $Ca(OH)_2$ and K-feldspar is inactive.

3.2. *In situ* sequestration of mechanochemically modified K-feldspar with $Ca(OH)_2$ and CaO

To intensify CO_2 capture by modified K-feldspar, another investigation strategy was chosen- two-step milling. In the first step, K-feldspar was milled with the addition of $Ca(OH)_2$, or CaO, resulting in a mechanochemically altered K-feldspar, and subsequently in the following second step *in situ* CO_2 sequestration was realized. XRD analysis performed after sequestration confirmed the formation of the calcite phase, $CaCO_3$ in all three cases (Figure 5). This is the evidence that there is a chemical bond between CO_2 and Ca^{2+} during *in situ* sequestration, i.e. 30 min of milling in a CO_2 atmosphere and the so-called mechanochemical carbonation took place. Moreover, the inactivity of as-received K-feldspar was also detected in this case.

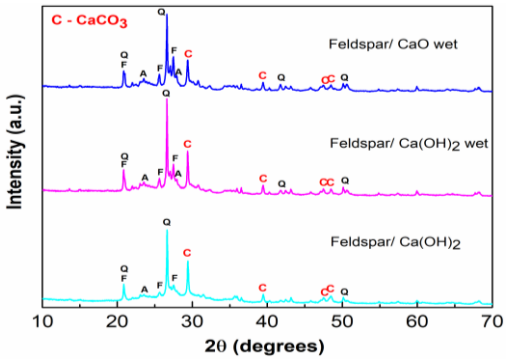

Figure 5

XRD patterns of K-feldspar after two-step milling: mechanochemical modification with $Ca(OH)_2$ and CaO and subsequent in situ CO_2 sequestration

With the aim to confirm $CaCO_3$ formation during milling in a CO_2 atmosphere, the thermal decomposition accompanied by the evolution of gases from the calcium carbonate-containing samples was monitored. Figure 6 compares the thermal behaviour of K-feldspar modified with $Ca(OH)_2$ and CaO after *in situ* mechanochemical carbonation.

As can be seen, in both cases, the TG/DTG-DTA curves are similar. As expected, the evolution of H_2O and CO_2 gases has been observed in both cases. While dehydration occurred in the range of 25–400 °C, decarbonation occurred in the range of 500–850 °C, which confirmed the decomposition of the mechanochemically formed calcite phase.

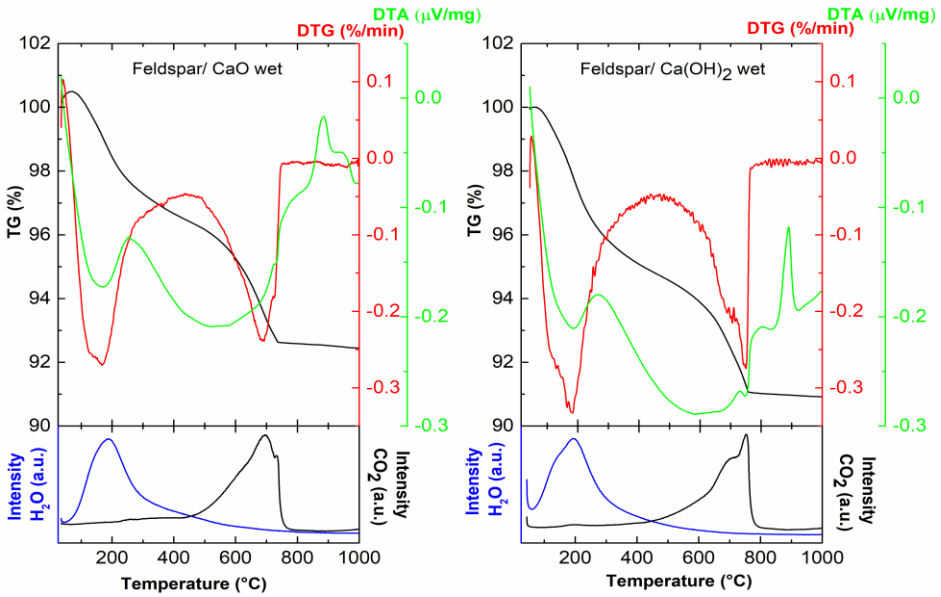

Figure 6

TG/DTG-DTA curves with mass spectrometry analysis of K-feldspar after two-step milling: mechanochemical modification with $Ca(OH)_2$ and CaO and subsequent in situ CO_2 sequestration

The results of CHNS elemental analysis and the values of CO_2 carbonation (mineralization) ratios of the samples after *in situ* CO_2 sequestration are summarised in Table 2. According to the analysis of the amount of carbon, about 1.2–1.36% C was actually bound in the modified samples after deducting the amount of C of 0.27% corresponding to the unmodified K-feldspar. The contents of N and S were under the detection limit. The mineralization ratio increased up to 7 times compared to unmodified K-feldspar and reached a value of 5.23% comparable to the result achieved by milled K-feldspar (up to 20 h) with the addition of $CaCl_2$-slag, while the CO_2 sequestration was carried out in an autoclave at a temperature of 150 °C and a pressure of 4 MPa (Shangguan et al. 2016).

Table 2

CHNS elemental analysis of K-feldspar after two-step milling: mechanochemical modification with $Ca(OH)_2$ and CaO and subsequent in situ CO_2 sequestration and calculated CO_2 carbonation ratio

Sample	C [%]	H [%]	CO_2 carbonation ratio [%]
Feldspar	0.27	1.59	0.74
Feldspar/ CaO wet	1.50	0.71	3.49
Feldspar/ $Ca(OH)_2$ wet	1.63	0.82	4.66
Feldspar/ $Ca(OH)_2$	1.47	0.76	5.23

3.3. *In situ* sequestration of K-feldspar and vermiculite mixtures

In addition to introducing pure artificial chemicals to the K-feldspar, also natural material can be used in this way. It is known that vermiculite mineral is capable of sequestrating CO_2. In order to find a potential synergy and thus the improvement of the CO_2 sequestration ability of K-feldspar, the mixtures of K-feldspar and vermiculite were prepared and subsequently subjected to sequestration. The XRD patterns are provided in Figure 7.

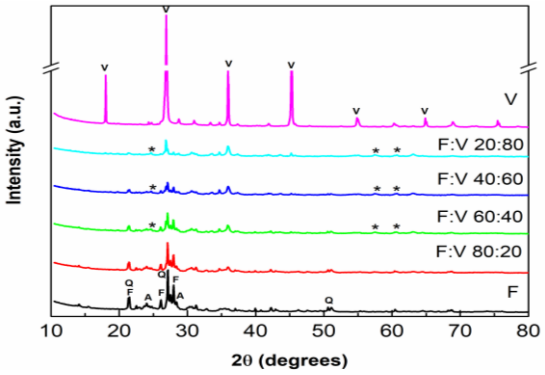

Figure 7

XRD patterns of as-received K-feldspar(F), K-feldspar(F): vermiculite(V) mixtures, and as-received vermiculite(V) after in situ CO_2 sequestration. Specific peaks are marked with an asterisk- see the explanation in the text below)

The XRD pattern of the K-feldspar after CO_2 sequestration is almost completely identical to the starting one described in (Baláž et al. 2024). All diffractions corresponding to microcline or K-feldspar (F), albite (A) and quartz (Q) are visible. Thus, the effect of neither mechanochemical modification nor sequestration is visible. Increasing the content of vermiculite leads to a gradual decrease in K-feldspar diffractions, whereas those corresponding to vermiculite become more pronounced. Interestingly, the four main vermiculite diffractions are still less pronounced than those corresponding to K-feldspar in the F:V 40:60 sample. The diffractions of as-received vermiculite are much more intensive (the counts detected for the most intensive diffraction peak detected for this sample are more than 17 times higher than that of the most intensive one belonging to K-feldspar, and that of other samples are even less intensive) and point to potentially different mechanism involved in CO_2 sequestration. This is further supported by the fact that there are few diffraction peaks (e.g., at 2 Θ = 24.7°, 57.6 ° and 60.7°) that increase in intensity until F:V 20:80 mixture (marked with an asterisk in Figure 7), but they remain in the same intensity when as-received vermiculite was applied. However, no clear diffractions corresponding to carbonate species in either of the samples could be clearly identified via XRD.

However, due to the detection limit of the XRD technique being around 5%, the potential presence of carbon as a result of mechanochemical carbonation was investigated via elemental analysis. The results are provided in Table 3.

Table 3

CHNS elemental analysis of as-received K-feldspar, vermiculite and the mixtures K-feldspar:vermiculite after in situ CO_2 sequestration

Sample [wt.%]	C [%]	H [%]	N [%]	S [%]
Vermiculite 100	0.30	2.21	0.07	0.11
F:V 20:80	0.89	0.55	0.15	0.09
F:V 40:60	0.65	1.15	0.13	0.06
F:V 60:40	0.54	0.55	0.13	0.06
F:V 80:20	0.31	1.57	0.12	0.06
Feldspar 100	0.18	1.24	0.15	0.02

K-feldspar is capable of binding only 0.18% C, whereas, in the case of vermiculite, this value is 0.30%. Interestingly, the composites seem to be more favourable for C binding than as-received vermiculite. Namely, the mixture containing only 20% vermiculite shows the same result and a gradual increase of C content with further increasing vermiculite content can be observed in Table 3. It turns out that K-feldspar can serve the role of the beneficial support to vermiculite being an efficient CO_2 adsorbent, thus a synergy between the two minerals was confirmed in the end. Figure 8 shows the FT-IR spectra of F:V mixtures in four different ratios (20:80 wt.%, 40:60 wt.%, 60:40 wt.%, 80:20 wt.%) after in situ CO_2 sequestration, in the range of 4000–600 cm^{-1}.

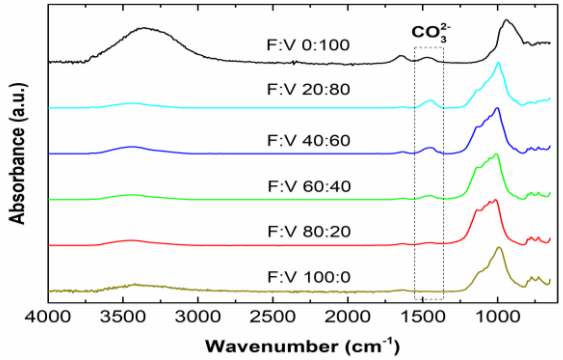

Figure 8

FT-IR spectra of K-feldspar: vermiculite mixtures, F:V after in situ CO_2 sequestration

In the case of K-feldspar mixtures, the intensity of a single carbonate peak with a maximum at approximately 1450 cm^{-1} is present and decreases with an increasing proportion of K-feldspar. Clearly, CO_2 was sequestered by vermiculite. However, it should be noted that the presence of K-feldspar is not negligible. When comparing the CHNS analysis results for as-received vermiculite (100 wt.%) with the F:V mixture (20:80 wt.%), almost 3 times higher amount of carbon was found in the mixture, indicating a greater amount of sequestered CO_2. The interaction of natural and thermally processed vermiculite with CO_2 during milling was also confirmed by Turianicová et al. (2014).

4. DISCUSSION AND CONCLUSIONS

In this paper, three hitherto unused strategies for the potential use of common but refractory K-feldspar mineral for CO2 sequestration were presented and tested. Before sequestration itself, which took place during the thermal process in a CO2 atmosphere (ex situ) or during milling in a planetary mill (in situ), the K-feldspar was mechanochemically modified by milling. KOH, Ca(OH)2, and CaO with and without H2O were used for its mechanochemical modification. In the ex situ strategy, it was found that binding of CO2 to K-feldspar modified with KOH and Ca(OH)2 occurred and depended only on the added additive. During the second in situ strategy of mechanochemically modified K-feldspar with Ca(OH)2, and CaO mechanochemical carbonation and subsequent calcite formation occurred, while a maximum CO2 carbonation/mineralization ratio of 5% was achieved by 30 min milling. The third in situ strategy consisted of adding the mineral vermiculite capable of sequestering CO2 to the K-feldspar in different weight ratios. The highest content of captured carbon 0.89% was achieved for the K-feldspar:vermiculite 20:80 composite during 30 minutes of milling in a CO2 atmosphere.

A variety of techniques with new experimental approaches were applied in this case. Both applied strategies (*ex situ* and *in situ*) manifested new possibilities to expand the portfolio of usable materials for mineral decarbonation. Except for artificial chemicals, calcium-based additives also natural material – vermiculite were applied for the modification of K-feldspar. This expanded portfolio of objects under study revealed different mechanisms of CO_2 sequestration. However, despite the particular success caused by the modification of K-feldspar, the application of K-feldspar alone has no beneficial effect on CO_2 sequestration.

ACKNOWLEDGEMENTS

The present investigation was supported by the ERA-MIN3 POTASSIAL 27 project and the Scientific and Technological Research Council of Türkiye (Project 122N039). The authors are grateful to the group of Prof. Emmerling from the Federal Institute of Materials Research and Testing (BAM) in Berlin, Germany for making XRD analysis available.

REFERENCES

What is carbon neutrality and how can it be achieved by 2050?, Topics European Parliament. Available online: https://www.europarl.europa.eu/news/en/headlines/society/20190926STO62270/what-is-carbon-neutrality-and-how-can-it-be-achieved-by-2050 (Accessed on 13 June 2023).

Baláž, P. (2008). *Mechanochemistry in Nanoscience and Minerals Engineering.* Berlin, Springer. https://doi.org/10.1007/978-3-540-74855-7

Baláž, M., Birinci, M., Şentürk, K., Achimovičová, M., Baláž, P., Tampubolon, I. O., Stolar, T., Bienert, R., Emmerling, F., Ergemoglu, S, Sis, H., Ergemoglu, M. (2024).

Utilizing Taguchi method and in situ X-ray powder diffraction monitoring to determine the influence of mechanical activation conditions on the physico-chemical properties and Al leachability of K-feldspar. *Journal of Materials Research and Technology*, 32, pp. 3886–95. https://doi.org/10.1016/j.jmrt.2024.08.156

Guo, Y., Li, C., Lu, S., Zhao, C. (2015). K_2CO_3-modified potassium feldspar for CO_2 capture from post-combustion flue gas. *Energy & Fuels*, 29 (12), pp. 8151–8156. https://doi.org/10.1021/acs.energyfuels.5b02207

Kalinkin, A., Boldyrev, V., Politov, A., Kalinkina, E., Makarov, V., Kalinnikov, V. (2003). Investigation into the mechanism of interaction of calcium and magnesium silicates with carbon dioxide in the course of mechanical activation. *Glass Physics and Chemistry*, 29 (4), pp. 410–414. https://doi.org/10.1023/A:1025185229274

Kalinkin, A., Kalinkina, E., Politov, A., Makarov, V., Boldyrev, V. (2004). Mechano-chemical interaction of Ca silicate and aluminosilicate minerals with carbon dioxide. *Journal of Materials Science*, 39 (16–17), pp. 5393–5398. https://doi.org/10.1023/B:JMSC.0000039252.13062.63

Kalinkina, E., Kalinkin, A., Forsling, W., Makarov, V. (2001a). Sorption of atmospheric carbon dioxide and structural changes of Ca and Mg silicate minerals during grinding – I. Diopside. *International Journal of Mineral Processing*, 61 (4), pp. 273–288. https://doi.org/10.1016/S0301-7516(00)00035-1

Kalinkina, E., Kalinkin, A., Forsling, W., Makarov, V. (2001b). Sorption of atmospheric carbon dioxide and structural changes of Ca and Mg silicate minerals during grinding – II. Enstatite, akermanite and wollastonite. *International Journal of Mineral Processing*, 61 (4), pp. 289–299. https://doi.org/10.1016/S0301-7516(00)00038-7

Ma, Z., Zheng, D., Liang, B., Liang, B., Li, H. (2024). Effect of vermiculite-modified biochar on carbon sequestration potential, mercury adsorption stability, and economics. *Biomass Conversion and Biorefinery*. https://doi.org/10.1007/s13399-024-05774-0

Nakamoto, K. (2008). *Infrared and Raman Spectra of Inorganic and Coordination Compounds: Part A: Theory and Applications in Inorganic Chemistry*, 6th edition. John Wiley & Sons, Inc. https://doi.org/10.1002/9780470405840

O'Connor, W., Dahlin, D., Rush, G., Dahlin, C., Collins, W. (2002). Carbon dioxide sequestration by direct mineral carbonation: process mineralogy of feed and products. *Minerals & Metallurgical Processing*, 19 (2), pp. 95–101. https://doi.org/10.1007/BF03403262.

Pachauri, R.K., Reisinger, A. (2007). Synthesis Report. Contribution of Working Groups I, II and III to the Fourth Assessment Report of the Intergovernmental Panel on Climate Change. *IPCC, Climate Change 2007*, Geneva, Switzerland.

Seifritz, W. (1990). CO_2 disposal by means of silicates. *Nature*, 345 (6275), p. 486. https://doi.org/10.1038/345486b0

Shangguan, W., Song, J., Yue, H., Tang, S., Liu, Ch., Li, Ch., Liang, B., Xie, H. (2016). An efficient milling-assisted technology for K-feldspar processing, industrial waste treatment and CO_2 mineralization. *Chemical Engineering Journal*, 292, pp. 255–63. https://doi.org/10.1016/j.cej.2016.02.031

Turianicová, E. (2009). CO_2 sequestration on mechanically activated minerals. PhD. Thesis, Institute of Geotechnics, Slovak Academy of Sciences, Košice.

Turianicová, E., Baláž, P., Tuček, L., Zorkovská, A., Zeleňák, V., Németh, Z., Šatka, A., Kováč, J. (2013a). A comparison of the reactivity of activated and non-activated olivine with CO_2. *International Journal of Mineral Processing*, 123, pp. 73–77. https://doi.org/10.1016/j.minpro.2013.05.006

Turianicová, E., Obut, A., Zorkovská, A., Baláž, P, Matik, M., Briančin, J. (2013b). The effects of LiOH and NaOH on the carbonation of $SrSO_4$ by dry high-energy milling. *Minerals Engineering*, 49, pp. 98–102. https://doi.org/10.1016/j.mineng.2013.05.017.

Turianicová, E., Obut, A., Tuček, Ľ, Zorkovská, A., Girgin, İ., Baláž, P., Németh, Z., Matik, M., Kupka., D. (2014). Interaction of natural and thermally processed vermiculites with gaseous carbon dioxide during mechanical activation. *Applied Clay Science*, 88–89, pp. 86–91. https://doi.org/10.1016/j.clay.2013.11.005

Wang, C., Yue, H., Li, C., Liang, B., Zhu, J., Xie, H. (2014). Mineralization of CO_2 using natural K-feldspar and industrial solid waste to produce soluble potassium. *Industrial & Engineering Chemistry Research*, 53 (19), pp. 7971–7978. https://dx.doi.org/10.1021/ie5003284.

Ye, L., Yue, H., Wang, Y., Sheng, H., Yuan, B., Lv, L., Li, Ch., Liang, B., Zhu, J., Xie, H. (2014). CO_2 mineralization of activated K-feldspar + $CaCl_2$ slag to fix carbon and produce soluble potash salt. *Industrial & Engineering Chemistry Research*, 53, pp. 10557–10565, https://dx.doi.org/10.1021/ie500992y

Geosciences and Engineering, Vol. 13, No. 1 (2025), pp. 45–58.
https://doi.org/10.33030/geosciences.2025.01.004

MECHANOCHEMICALLY SYNTHESIZED TERNARY CHALCOGENIDE $CuInSe_2/TiO_2$ NANOCOMPOSITE FOR SOLAR CELL APPLICATIONS

ERIKA DUTKOVÁ[1, *], MATEJ BALÁŽ[2], JAROSLAV KOVÁČ[3], ADELIA KASHIMBETOVA[4], JAROSLAV BRIANČIN[5], JAROSLAV KOVÁČ, Jr.[6], LADISLAV ČELKO[7]

[1, *]*Institute of Geotechnics Slovak Academy of Sciences, Slovakia; dutkova@saske.sk*
[2]*Institute of Geotechnics Slovak Academy of Sciences, Slovakia; balazm@saske.sk*
[3]*Institute of Electronics and Photonics, Slovak University of Technology, Slovakia; jaroslav.kovac@stuba.sk*
[4]*Central European Institute of Technology, Brno University of Technology, Czech Republic; kashimbetova@vutbr.cz*
[5]*Institute of Geotechnics Slovak Academy of Sciences, Slovakia; briancin@saske.sk*
[6]*Institute of Electronics and Photonics, Slovak University of Technology, Slovakia; jaroslav_kovac@stuba.sk*
[7]*Central European Institute of Technology, Brno University of Technology, Czech Republic; ladislav.celko@ceitec.vutbr.cz*

Abstract: In this paper, the simple mechanochemical synthesis of $CuInSe_2/TiO_2$ nanocomposite is described. $CuInSe_2/TiO_2$ nanocomposite was characterized from the crystal structure, microstructural, morphology, surface, optical, and optoelectrical properties viewpoints. X-ray diffraction has confirmed the nanocrystalline character of all components of the nanocomposite, the crystallite size for $CuInSe_2$ (18 nm) being larger than in the case of both TiO_2 phases (5 and 8 nm for rutile and anatase, respectively). Raman spectroscopy confirmed the presence of both components in the synthesized nanocomposite. SEM has shown that the nanoparticles are agglomerated into larger grains. High-resolution XPS analysis confirmed the presence of all elements with their expected oxidation states. The measured optical properties using UV-Vis spectroscopy exhibit stronger absorption from the ultraviolet to visible region with the determined optical bandgap 1.3 eV for mechanochemically synthesized $CuInSe_2/TiO_2$ nanocomposite. The photocurrent increased by 57% in $CuInSe_2/TiO_2$ nanocomposite compared to $CuInSe_2$ under illumination in comparison with that in the dark state.

Keywords*: mechanochemistry, $CuInSe_2/TiO_2$, nanocomposite, optical properties, optoelectrical properties*

1. INTRODUCTION

Ternary chalcogenide semiconductors of I–III–VI group with promising applications in electronics, optics, and catalysis have been intensively studied in recent years (Klenk et al., 2011). However, the majority of the best investigated sulphide-based semiconductors contain toxic heavy metals, which seriously limit their potential application.

$CuInSe_2$ is also one of the promising semiconductive ternary materials applicable in high-efficiency solar cells and photocatalysis due to its large absorption coefficient, suitably small bandgap, large conversion efficiency and radiation stability (Guo et al., 2008; Kang et al., 2009). It is beneficial to couple $CuInSe_2$, a small bandgap semiconductor (its bulk bandgap is 1.05 eV) with the material with a larger bandgap, like TiO_2 (its bulk bandgap is 3.2 eV). Coupling these two components can improve optical properties due to the elimination of surface non-radiative recombination defects. $CuInSe_2/TiO_2$ nanocomposite can be an excellent alternative for solar cell applications (Yu et al., 2011; Das et al., 2017), as well as for the photocatalytic degradation of dyes in the visible light region.

There are several synthetic procedures for the preparation of $CuInSe_2/TiO_2$ nanomaterial, including thermal and microwave assisted hybridization (Kshirsagar et al., 2017), oxidative chemical polymerization method (Yu et al., 2011), electrodeposition technique (Valdes et al., 2011; Das et al., 2017), colloidal synthesis (Wu et al., 2015), electrophoretic deposition technique (Liao et al., 2013), simple successive ionic layer adsorption and reaction (SILAR) method (Wang et al., 2015), spin coating method (Zhang et al., 2020), electrochemical anodic oxidation and solvothermal synthesis (Yang et al., 2022).

Mechanochemistry as an environmentally friendly alternative to the traditional preparation methods is well-applicable in the field of materials science. The high-energy milling process is used either as a synthesis step to prepare inorganic nanomaterials applicable in advanced applications or to introduce defects into the crystalline structure, which can dramatically improve the application potential (Baláž et al., 2017).

To the best of our knowledge, the $CuInSe_2/TiO_2$ nanocomposite has not been prepared by mechanochemical synthesis so far. The novelty of this work is the simple and environmentally friendly mechanochemical method of $CuInSe_2/TiO_2$ nanocomposite preparation for a very short time, at ambient pressure and temperature as a suitable material for solar cell applications.

2. MATERIALS AND METHODS

2.1. Materials

For the synthesis of $CuInSe_2/TiO_2$ nanocomposite were used: elemental copper (99.7%, Merck, Darmstadt, Germany), indium (99.99%, Aldrich, Taufkirchen, Germany), selenium (99.5% Aldrich, Taufkirchen, Germany) and commercially available TiO_2 Degussa P25 (Degussa, Netherland) (75% anatase and 25% rutile).

2.2. Methods

$CuInSe_2/TiO_2$ nanocomposite was synthesized by a two-step process. In the first step (Equation 1), $CuInSe_2$ was prepared by milling 0.94 g of copper, 1.71 g of indium and 2.35 g of selenium. The milling was carried out in a planetary mill Pulverisette 6 (Fritsch, Idar-Oberstein, Germany) at 550 rpm using a tungsten carbide milling

chamber (250 mL in volume) and 50 balls (360 g) with 10 mm in diameter, composed of the same material, during 60 min in an argon atmosphere according the procedure described in (Dutkova et al., 2016). The ball-to-powder ratio was 72:1. In the second step, 2.5 g of TiO_2 was introduced into milling with 2.5 g of previously synthesized $CuInSe_2$. Co-milling (Equation 2) was also performed in a planetary mill Pulverisette 6 (Fritsch, Idar-Oberstein, Germany) in an argon atmosphere (>99.998%, Linde Gas group, Bratislava, Slovakia) for 30 min without break cooling due to shorter milling times. The milling chamber was vented with Ar gas for 3 min providing an inert atmosphere. The 250 mL tungsten carbide milling chamber with 50 tungsten carbide balls with 10 mm in diameter was used. The rotational speed of the planet carrier was 500 rpm. The ball-to-powder ratio was 72:1.

The synthesis of $CuInSe_2/TiO_2$ nanocomposite can be described by the following Equations 1–2:

$$Cu + In + 2Se \rightarrow CuInSe_2 \quad (1)$$

$$CuInSe_2 + TiO_2 \rightarrow CuInSe_2/TiO_2 \quad (2)$$

2.3. Characterization techniques

X-ray diffraction (XRD) measurements were performed using a D8 Advance diffractometer (Bruker, Bremen, Germany) equipped with a θ-θ goniometer, CuK_α radiation (40 kV, 40 mA), a secondary graphite monochromator, and a scintillation detector. All samples were scanned from 15° to 70° with the step 0.03° and 12 s counting time. Diffracplus Eva software was used for phase analysis according to the ICDD - PDF2 database. The Rietveld refinement was performed using a TOPAS Academic software (Evans, 2010; Coelho, 2018).

The micro-Raman and micro-PL measurements were performed in air at room temperature, with the focus of the beam of an Ar laser (514 nm) via a confocal Raman Microscope (Spectroscopy & Imaging, Warstein, Germany) in backscattering geometry. The frequency of the Raman line of crystalline Si at 520 cm^{-1} was used to calibrate the system in the present study.

Morphology was investigated using a field emission-scanning electron microscope (FE-SEM, Mira 3, Tescan, Czech Republic) coupled with an EDX analyzer (Oxford Instruments).

The values of the specific surface area were received by using a NOVA 1200e Surface Area & Pore Size Analyzer (Quantachrome Instruments, Boynton Beach, FL, USA).

The X-ray photoelectron spectroscopy (XPS) measurements were performed in the XPS Kratos Axis Supra apparatus (Manchester, UK) with a monochromatic AlKα X-ray radiation, an emission current of 15 mA, and a hybrid lens model. XPS survey and high-resolution (HR) spectra were recorded using scanning steps of 1.0 and 0.1 eV, respectively. The obtained data were calibrated by setting the C1s emission at 284.8 eV. The deconvolution and fitting of the interesting elements were carried out using the CasaXPS software (version 2.3.17) by applying a Spine Shirley

background in the high-resolution spectra and a Gaussian/Lorentzian line shape for fitting the XPS peaks.

Absorption spectra were recorded using a UV-Vis spectrophotometer Helios Gamma (Thermo Electron Corporation, Warwickshire, UK) in a quartz cell by dispersing the synthesized particles in absolute ethanol by ultrasonic stirring. The band gap energy (Eg) was determined by utilization of Tauc equation (3):

$$(\alpha h\nu)^{1/n} = A(h\nu - E_g) \quad (3)$$

where α is the absorption coefficient, A is a constant, h = Planck's constant, ν = frequency and n is a constant associated with different kinds of electronic transitions (0.5 for a direct allowed, 2 for an indirect allowed, 1.5 for a direct forbidden and 3 for an indirect forbidden). The optical band gap, Eg was estimated by plotting $(\alpha h\nu)^2$ as a function of the photon energy hν. Extrapolating the straight line portion of the Tauc plot for zero absorption coefficient (α = 0) gives optical bandgap energy.

The current-voltage (I-V) characteristics were measured using semiconductor parameter analyzer Agilent 4155C under dark and focused halogen white light illumination (illumination intensity of ~ 600 mW/cm^2). The measured sample was separated from crushing pellets to small pieces (thin stripe with dimensions ~ 200-500 μm) and transferred onto insulating pad. The sample contacts were made by small droplet of silver paste and then annealed together with wiring to the socket.

3. Results and Discussion

3.1. Structural characterization

The X-ray diffraction (XRD) patterns of previously mechanochemically prepared $CuInSe_2$, commercial TiO_2 and mechanochemically synthesized $CuInSe_2/TiO_2$ nanocomposite are shown in Fig. 1. The Rietveld refinement was carried out to study the phase composition and crystallite size of the produced nanocomposite (Figure 2). The diffractions of both components of the nanocomposite can be well-seen in the figure. Surprisingly, the reflections corresponding to tetragonal $CuInSe_2$, the content of which is same with content of TiO_2, are more intensive that of TiO_2. This means that the crystallite size of selenide seems to be larger than in the case of titanium dioxide. With regards to TiO_2, commercial Degussa P25 with the 75% content of anatase and 25% of rutile has been used. However, the reflections corresponding to the latter are more pronounced, so it seems that the anatase-to-rutile phase transformation took place during milling, which has been previously observed (Kostova and Dutkova, 2016). According to Rietveld refinement, the estimated crystallite size of $CuInSe_2$ is 18 ±5 nm and the detected microstrain is 2.1 ±0.4%. $CuInSe_2$ crystallized in I-42d space group with the following refined lattice parameters a = 5.753 ±0.014 Å and c = 11.595 ±0.017 Å. For titanium dioxide phases, the estimated crystallite size is 5 ±1 and 8 ±1 nm for rutile and anatase, respectively, which confirms the presence of very fine crystallites and broad diffractions with low intensity detected for TiO_2 in the XRD pattern. TiO_2-anatase crystallized in I41/amd space group with the refined lattice parameters a = 3.764 ±0.007 Å

and c = 9.47 ±0.023 Å. Another one TiO_2- rutile phase crystallized in P42/mnm space group with the refined lattice parameters a = 4.590 ±0.017 Å and c = 2.973 ±0.013 Å.

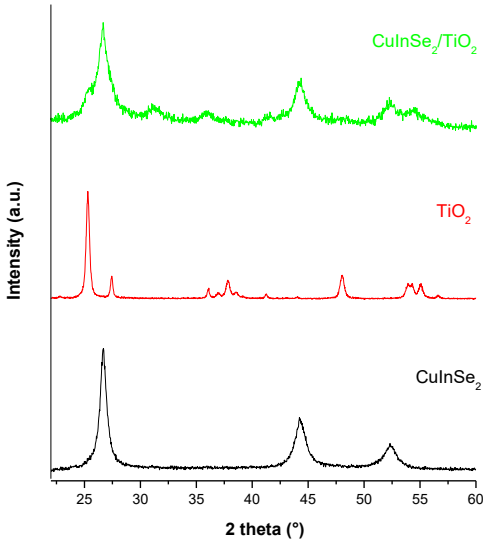

Figure 1
XRD patterns of $CuInSe_2$, TiO_2, and $CuInSe_2/TiO_2$ nanocomposite

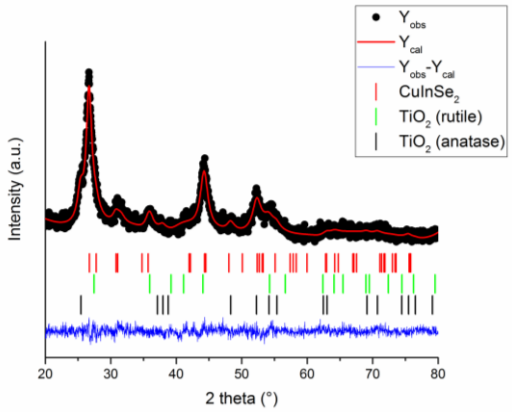

Figure 2
XRD pattern and the results of Rietveld refinement of $CuInSe_2/TiO_2$ nanocomposite

The micro-Raman spectra of the synthesized $CuInSe_2$, $CuInSe_2/TiO_2$ nanocomposite and commercially available TiO_2 under laser excitation at 514 nm are shown in Figure 3. The results of Raman spectrum of synthesized $CuInSe_2$ are in good agreement with previously published $CuInSe_2$ measurements (Rincon and Ramirez, 1992; Zaretskaya et al., 2003). The $CuInSe_2/TiO_2$ nanocomposite is a mixture of both components which are broadened upon interaction. The measured spectrum shows that

the dominant feature of Raman spectrum of $CuInSe_2/TiO_2$ nanocomposite are the peaks of TiO_2 showing the formation of a compound in various crystallographic forms – polymorphism (Tuschel, 2019). The intense peak at 146 cm^{-1} and a broad less intense peak at 250 cm^{-1} and near 395–440 cm^{-1} correspond to anatase form TiO_2 with symmetries E_g and B_{1g} and rutile form with symmetry E_g and E (Tuschel, 2019). The deflection near 173 cm^{-1} and peak at 208 cm^{-1} can be assigned to $CuInSe_2$ phase with symmetries A_1 and E. Raman spectroscopy confirmed the crystalline nanoparticles formation being in a good agreement with the results measured by XRD.

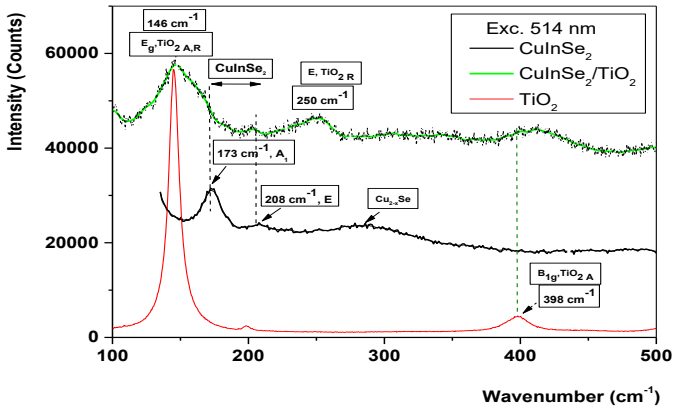

Figure 3

Micro-Raman spectrum of $CuInSe_2$, TiO_2, and $CuInSe_2/TiO_2$ nanocomposite

3.2. Surface and morphological characterization

The specific surface area (S_A) values belong to some of the most important characteristics of milled samples (Baláž et al., 2013). The S_A of pure $CuInSe_2$, from which the studied nanocomposite was prepared, is 2.9 m^2g^{-1} as was reported in (Dutkova et al., 2016). In the present study, the co-milling with TiO_2 led to a considerable increase of the specific surface area of the sample $CuInSe_2/TiO_2$ (13 m^2g^{-1}) in comparison with CuInSe2 alone. However, the obtained value is significantly lower than that acquired after the introduction of ZnS to $CuInSe_2$ reported in (Dutkova et al., 2021). Further, the S_A value of ZnS (108 m^2g^{-1}) is much higher than that of pure TiO_2 P25 (28.7 m^2g^{-1}). The achieved value of S_A for $CuInSe_2/TiO_2$ is far lower than in the other reports on similar systems applying different synthetic approaches (Kshirsagar et al., 2017).

The morphology of synthesized nanocomposite was studied by the means of scanning electron microscopy (SEM). SEM micrograph of the prepared $CuInSe_2/TiO_2$ nanocomposite is shown in Figure 4a. SEM image displays polydispersed particles, where the agglomerates exhibit the size in micrometers, however, smaller units with the sizes in the nanometer range can be clearly distinguished. The results of a representative EDX analysis are presented in Figure 4b. Several EDX analyses performed at different parts of the sample revealed a relatively homogeneous distribution of the elements present in $CuInSe_2/TiO_2$ nanocomposite.

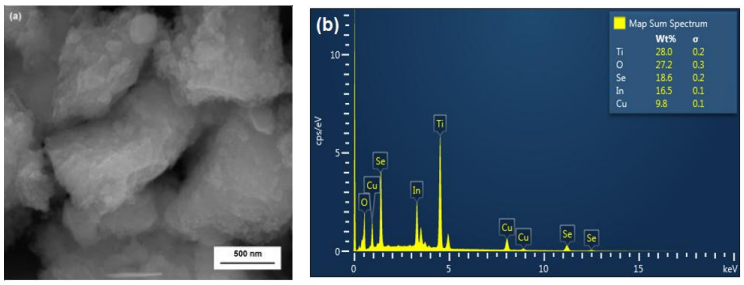

Figure 4

a) SEM image and (b) EDX spectrum recorded in characteristic parts of $CuInSe_2/TiO_2$ nanocomposite

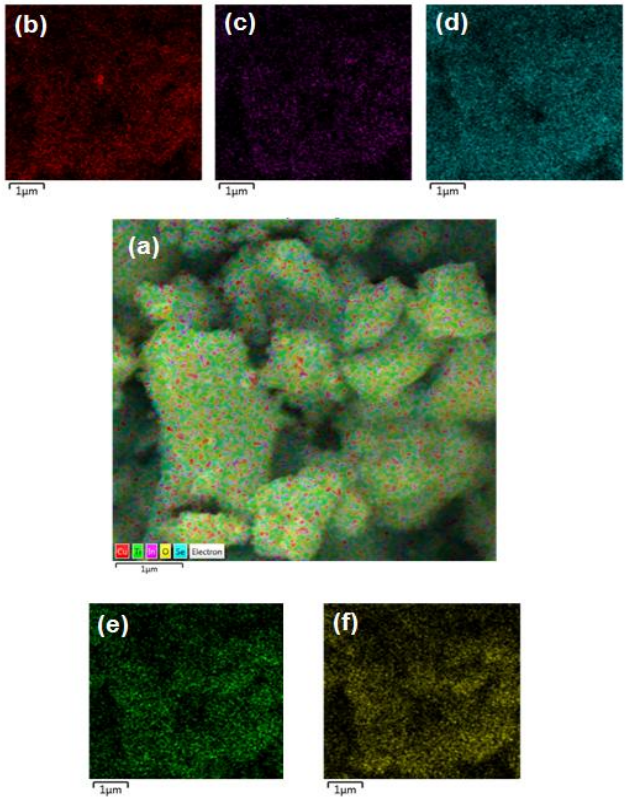

Figure 5

EDX mapping of $CuInSe_2/TiO_2$ nanocomposite. (a) EDX layered image; (b) EDX image of Cu distribution; (c) EDX image of In distribution; (d) EDX image of Se distribution; (e) EDX image of Ti distribution, and (f) EDX image of O distribution

The uniform distribution of all elements in the produced $CuInSe_2/TiO_2$ nanocomposite is well-documented utilizing the EDX mapping method. The results are shown in Figure 5. The EDX layered images of all the elements are illustrated in Figure 5a

and the individual EDX imaging for Cu, In, Se, Ti and O, respectively are shown in Figure 5b–f.

The surface composition of synthesized $CuInSe_2/TiO_2$ nanocomposite was analyzed by X-ray photoelectron spectroscopy (XPS). XPS survey and high-resolution spectra of $CuInSe_2/TiO_2$ nanocomposite are shown in Figure 6.

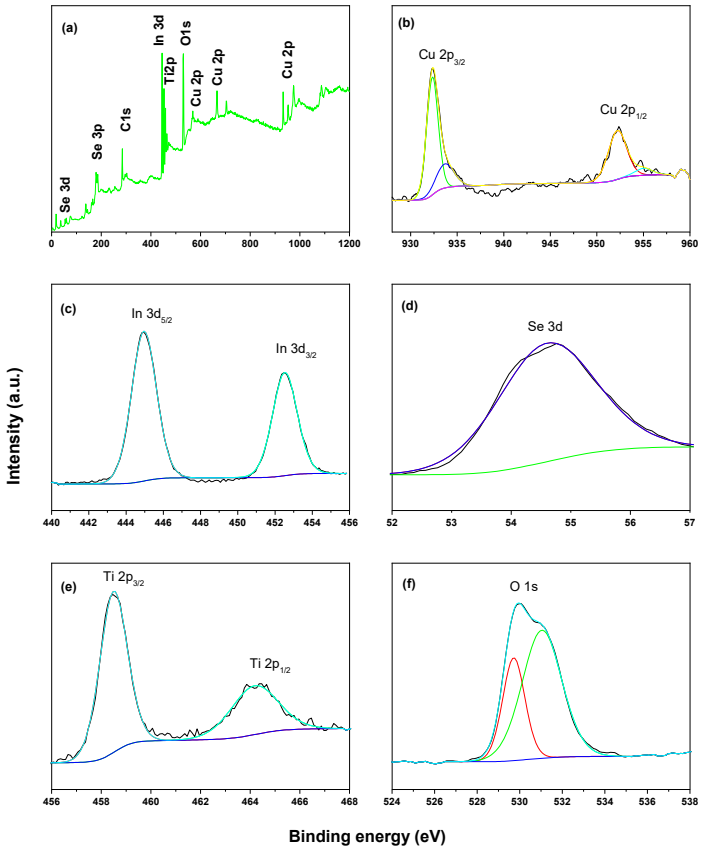

Figure 6

XPS survey spectrum (a) and high-resolution XPS spectra of $CuInSe_2/TiO_2$ nanocomposite: (b) – Cu 2p core level, (c) – In 3d core level, (d) – Se 3d core level, (e) Ti – 2p core level, (f) – O 1s core level

Cu, In, Se, Ti, O, and C as elements of interest, appear on XPS survey spectrum of the $CuInSe_2/TiO_2$ nanocomposite (Figure 6a). Regarding the high-resolution spectrum of Cu2p region (Figure 6b), there are two pairs of the spin-orbit components. Two components with higher intensity at 952.28 ($Cu2p_{1/2}$) and 932.36 eV ($Cu2p_{3/2}$), with a charge separation ΔE of 19.92 eV confirmed the monovalent nature of copper. The observed values are in accordance with the ones for $CuInSe_2$ reported in the paper (Chen et al., 2010; Kshirsagar et al., 2017). The other two components with lower intensity at 955.03 eV and 933.62 eV might be related to CuO. The doublet

components of the In3d core-level region appear at 444.96 eV ($In3d_{5/2}$) and at 452.46 eV ($In3d_{3/2}$), with a charge separation of 7.5 eV, which confirms the trivalent nature of indium (Figure 6c). As displayed in Figure 6d, the peak at 54.76 eV was indexed to $Se3d_{5/2}$, indicating the presence of Se^{2-} and proving the absence of oxide formation. $Ti2p_{3/2}$ and $Ti2p_{1/2}$ splitting components of Ti2p core-level region are found at 458.46 eV and 464.36 eV, which corresponds to the presence of TiO_2 compound. Thus, they are separated by 5.90 eV, which confirms the tetravalent nature of titanium (Figure 6e). O1s spectrum (Figure 6f) exhibits two components with binding energy positions of 529.76 eV and 531.06 eV. The results also indicate the presence of titanium dioxide. Binding energies showed that all the signals detected for individual elements Cu, In, Se, Ti and O confirmed their anticipated oxidation states. All the observed values for different elements match well with the reported ones in the paper (Kshirsagar et al., 2017).

3.3. Optical properties

The optical properties of $CuInSe_2$, TiO_2 and mechanochemically synthesized $CuInSe_2/TiO_2$ nanocomposite were investigated using UV-Vis (Figure 7) and microphotoluminescence spectroscopy at room temperature (Figure 8).

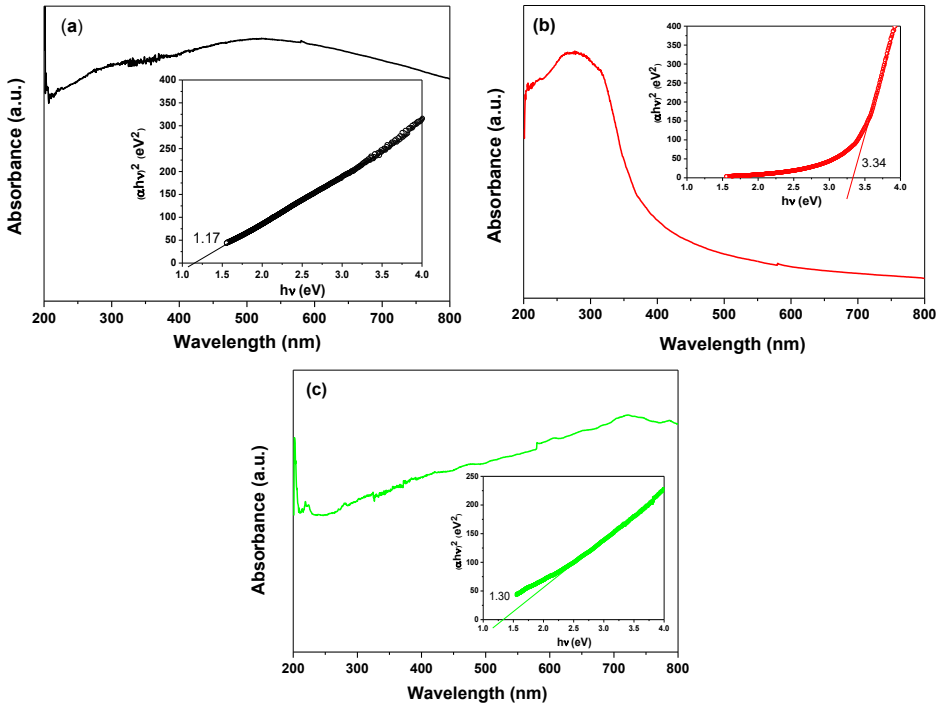

Figure 7

UV-Vis spectra and Tauc plots (inset) for $CuInSe_2$ (a), TiO_2 (b) and $CuInSe_2/TiO_2$ nanocomposite (c)

The optical band gaps were determined by plotting $(\alpha h\nu)^2$ against $(h\nu)$ and extrapolating the slope in the band edge region to zero (Equation 3) as shown in insets of Figure 7. The calculated band gap of $CuInSe_2$, TiO_2 and $CuInSe_2/TiO_2$ nanocomposite was determined to be 1.17, 3.34 and 1.30 eV, respectively. The optical band gap of TiO_2 was lightly blue-shifted in comparison with the previous reports (Kostova et al., 2015; Kostova and Dutkova, 2016). The optical band gap of $CuInSe_2$ was also blue-shifted compared to the bulk $CuInSe_2$ with band gap of 1.05 eV (Eisener et al., 1999). The observed band gap value of the nanocomposite is between those of pure $CuInSe_2$ and TiO_2 and mixing of both semiconducting materials are expected to show absorption patterns bearing the signature of both components. In comparison with pure $CuInSe_2$, the obtained $CuInSe_2/TiO_2$ nanocomposite exhibits lightly enhanced absorption in the visible light region.

Figure 8 shows the micro-photoluminescence (PL) spectrum of the mechanochemically synthesized $CuInSe_2$ and $CuInSe_2/TiO_2$ nanocomposite under laser excitation at 514 nm. In the spectrum of $CuInSe_2$ the peaks at 780 nm (1.59 eV) and 905 nm (1.37 eV) are in agreement with the peaks of nanoparticles published in the paper (Ghali et al., 2016). The interaction of $CuInSe_2$ with TiO_2 in the $CuInSe_2/TiO_2$ nanocomposite causes an increase and broadening of the emission spectrum in the 630 nm (1.96 eV) region which indicates the emission of $CuInSe_2$ nanoparticles, as described in the literature (Ghali et al., 2016). Clusters with $CuInSe_2$ quantum dots emanate a wide range of luminescence in the visible region depending upon their size and surface defects. The PL spectrum shows a gradual decrease up to the region of 1100 nm corresponding to the $CuInSe_2$ band gap (~1.12 eV).

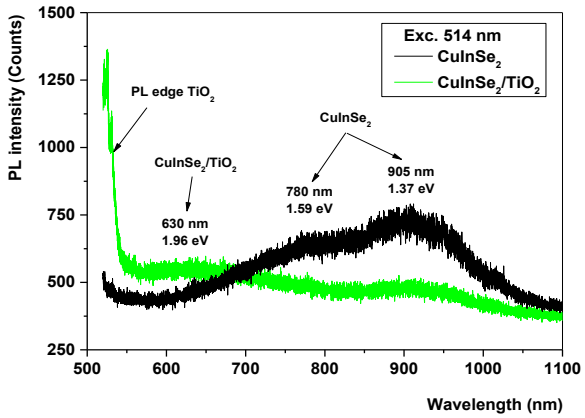

Figure 8
PL spectrum of $CuInSe_2$ and $CuInSe_2/TiO_2$ nanocomposite

3.4. Optoelectrical properties

To verify the optoelectrical properties of the mechanochemically synthesized $CuInSe_2$ and $CuInSe_2/TiO_2$ nanocomposite, the current-voltage (I-V) characteristics were measured in the dark and under illumination. The measured I-V characteristics

in the dark in Figure 9 show sufficient conductivity and are almost linear, which confirms the formation of an ohmic contact on the $CuInSe_2$ and prepared $CuInSe_2/TiO_2$ nanocomposite. After illuminating the sample, the number of generated charge carriers in the $CuInSe_2/TiO_2$ nanocomposite increases, causing an increase in the photocurrent. The results showed a photosensitivity of 5% for $CuInSe_2$ and 4.8% for $CuInSe_2/TiO_2$ at an applied voltage of 2 V compared to the current in the dark. Overall, in the nanocomposite $CuInSe_2/TiO_2$ compared to $CuInSe_2$, there was an increase in the current by 57%.

This suggests that the structure formed between $CuInSe_2$ and TiO_2 can increase the photoelectron transfer rate and promote the separation of photogenerated carriers as reported in the literature (Yu et al., 2011; Yang et al., 2022). The above-mentioned measurements of optoelectrical properties confirm the suitability of using this material for the absorber layer in solar cells.

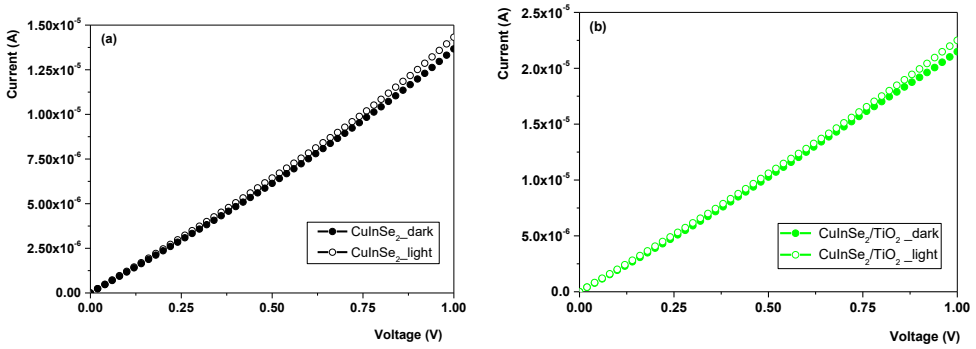

Figure 9

Current vs. Voltage (I-V) characteristics of (a) $CuInSe_2$ and (b) $CuInSe_2/TiO_2$ nanocomposite in the dark and under light illumination

4. CONCLUSIONS

In this work, $CuInSe_2/TiO_2$ nanocomposite was prepared by a simple, low-cost mechanochemical route. X-ray diffraction confirmed the nanocrystalline character of all the components of the nanocomposite, the crystallite size for $CuInSe_2$ (18 nm) being larger than in the case of both TiO_2 phases (5 and 8 nm for rutile and anatase, respectively). Raman spectroscopy confirmed the presence of both components in the nanocomposite. The morphology characterization using SEM demonstrated the homogeneity of the prepared nanocomposite. The surface properties investigated by the low-temperature nitrogen adsorption showed that the nanocrystallites are agglomerated into micron-scale particles and co-milling $CuInSe_2$ with TiO_2 led to a considerable increase of the specific surface area of the sample $CuInSe_2/TiO_2$ (13 m^2g^{-1}) in comparison with alone $CuInSe_2$. XPS analysis validated the presence of all elements in their expected oxidation states. Optical characterization indicated that the $CuInSe_2$ could extend the visible-light response range. $CuInSe_2/TiO_2$ nanocomposite exhibits strong absorption from the ultraviolet to visible region with the determined optical bandgap 1.3 eV. The current increased by 57% in $CuInSe_2/TiO_2$ nanocomposite compared to $CuInSe_2$.

This investigation has shown the possibility to prepare nanocomposite material with potential applications in optoelectronics by an environmentally friendly manner.

ACKNOWLEDGMENTS

This work was supported by the Slovak Research and Development Agency under the contracts No. APVV-18-0357, APVV-20-0437 and by the Slovak Grant Agency VEGA (project 2/0112/22 and 2/0084/23). The support of COST Action CA18112 MechSustInd (www.mechsustind.eu), supported by the COST Association (European Cooperation in Science and Technology, www.cost.eu is also acknowledged.

REFERENCES

Baláž, P., Achimovičová, M., Baláž, M., Billik, P., Cherkezova-Zheleva, Z., Criado, J. M., Delogu, F., Dutková, E., Gaffet, E., Gotor, F. J., Kumar, R., Mitov, I., Rojac, T., Senna, M., Streletskii, A. & Wieczorek-Ciurowa, K. (2013). Hallmarks of mechanochemistry: from nanoparticles to technology. *Chemical Society Reviews*, 42, pp. 7571–7637. doi: 10.1039/C3cs35468g

Baláž, P., Baláž, M., Achimovičová, M., Bujňáková, Z. & Dutková, E. (2017). Chalcogenide mechanochemistry in materials science: insight into synthesis and applications (a review). *Journal of Materials Science*, 52, pp. 11851–11890. doi:10.1007/s10853-017-1174-7

Coelho, A. A. (2018). TOPAS and TOPAS-Academic: an optimization program integrating computer algebra and crystallographic objects written in C plus. *Journal of Applied Crystallography*, 51, pp. 210–218. doi:10.1107/S1600576718000183

Das, S., Sopha, H., Krbal, M., Zazpe, R., Podzemna, V., Prikryl, J. & Macak, J. M. (2017). Electrochemical Infilling of $CuInSe_2$ within TiO_2 Nanotube Layers and Subsequent Photoelectrochemical Studies. *Chemelectrochem,* 4, pp. 495–499. doi:10.1016/j.tsf.2011.08.001

Dutkova, E., Bujnakova, L., Z., Sphotyuk, O., Jakubikova, J., Cholujova, D., Siskova, V., Daneu, N., Balaz, M., Kovac, J., Kovac, J., Briancin, J. & Demchenko, P. (2021). SDS-Stabilized $CuInSe_2$/ZnS Multinanocomposites Prepared by Mechanochemical Synthesis for Advanced Biomedical Application. *Nanomaterials*, 11. doi:Artn 6910.3390/Nano11010069

Dutkova, E., Sayagues, M. J., Kovac, J., Kovac, J., Bujnakova, Z., Briancin, J., Zorkovska, A., Balaz, P. & Ficeriova, J. (2016). Mechanochemically synthesized nanocrystalline ternary $CuInSe_2$ chalcogenide semiconductor. *Materials Letters*, 173, pp. 182–186. doi:10.1016/j.matlet.2016.03.051

Eisener, B., Wagner, M., Wolf, D. & Muller, G. (1999). Study of the intrinsic defects in solution grown $CuInSe_2$ crystals depending on the path of crystallization. *Journal of Crystal Growth*, 198, pp. 321–324. doi:10.1016/S0022-0248(98)01195-6

Evans, J. S. O. (2010). Advanced Input Files & Parametric Quantitative Analysis Using Topas. *Extending the Reach of Powder Diffraction Modelling by User Defined Macros*, 651, pp. 1–9. doi:10.4028/www.scientific.net/MSF.651.1

Ghali, M., Elnimr, M., Ali, G. F. & Yousif, B. (2016). Colloidal $CuInSe_2$ nanocrystals and thin films for low-cost photovoltaics. *Optical Materials*, 55, pp. 145–152. doi:10.1016/j.optmat.2016.03.026

Guo, Q., Kim, S. J., Kar, M., Shafarman, W. N., Birkmire, R. W., Stach, E. A., Agrawal, R. & Hillhouse, H. W. (2008). Development of $CuInSe_2$ nanocrystal and nanoring inks for low-cost solar cells. *Nano Letters*, 8, pp. 2982–2987. doi:10.1021/nl802042g

Chen, H., Yu, S. M., Shin, D. W. & Yoo, J. B. (2010). Solvothermal Synthesis and Characterization of Chalcopyrite $CuInSe_2$ Nanoparticles. *Nanoscale Research Letters*, 5, pp. 217–223. doi:10.1007/s11671-009-9468-6

Kang, F., Ao, J. P., Sun, G. Z., He, Q. & Sun, Y. (2009). Structure and photovoltaic characteristics of $CuInSe_2$ thin films prepared by pulse-reverse electrodeposition and selenization process. *Journal of Alloys and Compounds*, 478, L25–L27. doi:10.1016/j.jallcom.2008.12.020

Klenk, R., Klaer, J., Koble, C., Mainz, R., Merdes, S., Rodriguez-Alvarez, H., Scheer, R. & Schock, H. W. (2011). Development of $CuInS_2$-based solar cells and modules. *Solar Energy Materials and Solar Cells*, 95, pp. 1441–1445. doi:10.1016/j.solmat.2010.11.001

Kostova, N. & Dutkova, E. (2016). Mechanochemical synthesis and properties of ZnS/TiO_2 composites. *Bulgarian Chemical Communications*, 48, pp. 161–166.

Kostova, N. G., Dutkova, E., Eliyas, A., Stoyanova-Eliyas, E., Fabian, M. & Balaz, P. (2015). Mechanochemical synthesis, characterization, and photocatalytic activity of CdS/TiO_2 composites in air purification. *Bulgarian Chemical Communications*, 47, pp. 87–93.

Kshirsagar, A. S., Gautam, A. & Khanna, P. K. (2017). Efficient photo-catalytic oxidative degradation of organic dyes using $CuInSe_2/TiO_2$ hybrid hetero-nanostructures. *Journal of Photochemistry and Photobiology a-Chemistry*, 349, pp. 73–90. doi:10.1016/j.jphotochem.2017.08.058

Liao, Y. L., Zhang, H. W., Zhong, Z. Y., Jia, L. J., Bai, F. M., Li, J., Zhong, P., Chen, H. & Zhang, J. (2013). Enhanced Visible-Photocatalytic Activity of Anodic TiO_2 Nanotubes Film via Decoration with $CuInSe_2$ Nanocrystals. *ACS Applied Materials & Interfaces*, 5, pp. 11022–11028. doi:10.1021/am403264q

Rincon, C. & Ramirez, F. J. (1992). Lattice-Vibrations of $CuInSe_2$ and $CuGaSe_2$ by Raman Microspectrometry. *Journal of Applied Physics*, 72, pp. 4321–4324.

Tuschel, D. (2019). Molecular Spectroscopy Workbench Raman Spectroscopy and Polymorphism. *Spectroscopy*, 34, pp. 10–21.

Valdes, M., Goossens, A. & Vazquez, M. (2011). Sulfurization of electrodeposited $CuInSe_2$-based solar cells. *Materials Chemistry and Physics*, 125, pp. 860–865. doi:10.1016/j.matchemphys.2010.09.032

Wang, Q. Y., Qiao, J. L., Zhou, J. & Gao, S. M. (2015). Fabrication of $CuInSe_2$ quantum dots sensitized TiO_2 nanotube arrays for enhancing visible light photoelectrochemical performance. *Electrochimica Acta*, 167, pp. 470–475. doi:10.1016/j.electacta.2014.08.037

Wu, Z. M., Tong, X., Sheng, P. T., Li, W. L., Yin, X. H., Zou, J. M. & Cai, Q. Y. (2015). Fabrication of high-performance $CuInSe_2$ nanocrystals-modified TiO_2 NTs for photocatalytic degradation applications. *Applied Surface Science*, 351, pp. 309–315. doi:10.1016/j.apsusc.2015.05.147

Yang, Z. Y., Li, H., Cui, X. Q., Zhu, J. K., Li, Y. H., Zhang, P. F. & Li, J. R. (2022). Highly Efficient $CuInSe_2$ Sensitized TiO_2 Nanotube Films for Photocathodic Protection of 316 Stainless Steel. *Coatings*, 12. doi:Artn 1448 10.3390/Coatings12101448

Yu, Y. Y., Chien, W. C., Ko, Y. H. & Chen, S. H. (2011). Preparation and characterization of P_3HT:$CuInSe_2$:TiO_2 thin film for hybrid solar cell applications. *Thin Solid Films*, 520, pp. 1503–1510. doi:10.1016/j.tsf.2011.08.001

Zaretskaya, E. P., Gremenok, V. F., Riede, V., Schmitz, W., Bente, K., Zalesski, V. B. & Ermakov, O. (2003). Raman spectroscopy of $CuInSe_2$ thin films prepared by selenization. *Journal of Physics and Chemistry of Solids*, 64, pp. 1989–1993. doi:10.1016/S0022-3697(03)00216-6

Zhang, Y. N., Yang, Y., Hou, Z. Y., Jiang, X. J., Zhang, L., Yang, Y. Y. & Wang, Y. L. (2020). The effect of reaction temperature and time on $CuInSe_2$ quantum dots by solvothermal method. *AIP Advances*, 10. doi:Artn03531310.1063/1.5135065

Geosciences and Engineering, Vol. 13, No.1 (2025), pp. 59–68.
https://doi.org/10.33030/geosciences.2025.01.005

EXPERIMENTAL INVESTIGATION OF THE EFFECT OF THE POWDER AND THE SUSPENSION RHEOLOGY ON GRINDABILITY

KATALIN BOHÁCS[1*], ROLAND ROMENDA[2], ÁDÁM RÁCZ[3], TEEMU KINNARINEN[4], NAZILA BOLOURIEH[5], JÓZSEF FAITLI[6], BARNABÁS CSŐKE[7]

[1]*Institute of Raw Materials Preparation and Environmental Technology, University of Miskolc, Hungary; katalin.bohacs@uni-miskolc.hu*
[2]*Institute of Raw Materials Preparation and Environmental Technology, University of Miskolc, Hungary; roland.romenda@uni-miskolc.hu,*
[3]*Institute of Raw Materials Preparation and Environmental Technology, University of Miskolc, Hungary; adam.racz@uni-miskolc.hu*
[4]*LUT School of Engineering Sciences, Lappeenranta-Lahti University of Technology LUT, Lappeenranta, Finland; teemu.kinnarinen@lut.fi*
[5]*LUT School of Engineering Sciences, Lappeenranta-Lahti University of Technology LUT, Lappeenranta, Finland; nazila.bolourieh@lut.fi*
[6]*Institute of Raw Materials Preparation and Environmental Technology, University of Miskolc, Hungary, jozsef.faitli@uni-miskolc.hu*
[7]*Institute of Raw Materials Preparation and Environmental Technology, University of Miskolc, Hungary; csoke.barnabas@gmail.com*
[1]*https://orcid.org/0000-0001-8480-9701*
[2]*https://orcid.org/0009-0006-0003-5731*
[3]*https://orcid.org/0000-0002-6561-2177*
[6]*https://orcid.org/0000-0002-4037-5208*

Abstract: The grindability of raw materials is a key parameter of mineral processing. It is also very important for some kinds of secondary raw materials, such as demolition and construction wastes. The rheological behavior of the ground slurry or suspension evidently affects grinding because of the well-known viscous dampening effect. However, the grindability of materials as a function of the moisture content and rheology has not been studied online. Therefore, the grindability of a soft adhesive (limestone) and a hard non-adhesive (quartz) material was examined in the Universal Hardgrove Mill during room temperature dry and wet (in tap water) grinding. The powder flow behavior of the dry ground samples was measured in an FT4 powder rheometer, while the rheological properties of the wet ground suspensions were measured in a rotational rheometer.

Keywords: *grindability, Universal Hardgrove Mill, moisture content, grinding, quartz*

1. INTRODUCTION

The issue of the high energy demand of comminution is widely known in the literature and continuous research is ongoing in this field. On the other hand, the process engineering design of crushing and grinding units is typically carried out by using different kinds of grindability indices characterizing the given raw material. This is the

reason why the fundamental research of grindability test methodology development and the development of the auxiliary complementary test methodology is so important. At the Institute of Raw Materials Preparation and Environmental Technology of the University of Miskolc, it has a long tradition, the Universal Hardgove Mill and the Universal Bond Mill had been developed by with grindability can be measured at so called universal circumstances, namely at high temperature and in any kind of (neutral, acidic, alkali) media (Csőke et al., 2003; Mucsi et al., 2006).

Deniz (Deniz, 2022a and 2022b) determined the effects of kinetic breakage parameters on calcites in a Hardgrove mill. Yang et al. (Yang et al., 2020) studied experimentally the effect of moisture on Shengli lignite breakage behavior and energy efficiency. They concluded that the energy-size reduction process for grinding lignite is markedly influenced by moisture occurrence and content. Removing surface moisture from 37.90% to 16.61% (the air-dried condition) resulted in a slight increase of input energy by 0.04 kWh.t−1 per 10 s. However, with further drying to inherent moisture to 0%, the consumed energy significantly increased by 0.16 kWh.t−1 per 10 s. Meanwhile, the mass fraction of the top size decreased from 42.29% to 24.73% and then to 13.00%, while the pulverized coal production increased sharply from 6.28% to 10.68% and to 23.64%, both at a grinding time of 6 min. The energy efficiency was also significantly improved as the moisture content of lignite was reduced to below the air-dried level. The air-dried moisture content was the inflecting point for lignite grinding in the Hardgrove mill. A two-stage pre-drying system was proposed accordingly. The experimental results of Vuthaluru et al. (Vuthaluru et al., 2003) suggest that no relationship exists between the coarse fraction moisture and Hardgrove index in the case of coal. Beyond these, lack of knowledge about the effect of the moisture content on grindability can be found in the literature in the case of quartz or limestone. The effect of the moisture content of coal (Vuthaluru et al., 2003; Yang et al., 2020) was measured.

Another current issue is the question of viscous dampening in comminution machines. Therefore, two model materials, – a soft and adhesive material: the limestone and a hard and non-adhesive material: the quartz – were selected. After the preparation of the taken samples the so-called dry (< 20 m/m% moisture content) and wet (> 50 m/m%) grindability tests were carried out in the Universal Hardgrove Mill. At this time auxiliary tests had also been carried out. Powder flow features were measured in a powder rheometer and suspension rheology was measured in a rotational rheometer.

2. MATERIALS AND METHODS

The limestone samples – with a particle density of 2680 kg/m^3 (measured by liquid pycnometer in water) were taken in Tornanádaska, Hungary. The quartz samples – with a particle density of 2631 kg/m^3 (measured by a liquid pycnometer in water) were taken in Alsózsolca, Hungary. The Hardgrove grindability index was measured by the earlier developed – but a newly built and improved – Universal Hardgrove Mill (Figure 1 and 2). Parts of the Universal Hardgrove Mill are: 1. Grinding balls, 2. Shaped closing assembly for pushing down the balls, 3. Grinding crucible, 4. Crucible furnace: heat-insulating enclosure with three 230 V/500 W heating wires and

three PT100 platinum thermal resistors, 5. Electric connection field for connecting the heating wires and thermal resistors, 6. Electric connection field for connecting the heating wire and thermal resistor, 7. Cover of crucible furnace: heat-insulating enclosure with one 230 V/500 W heating wire and one PT100 platinum thermal resistor, 8. Axially moving shaft with bearing, 9. Bearing, 10. Worm-gear drive, 11. Weight, 12. Asynchronous motor, 13. Lever, 14. Measurement electronics, 15. Measurement data acquisition and A/D card, measuring and controlling computer, measuring and controlling software, 16, Axial bearing, 17. Force measuring transducer.

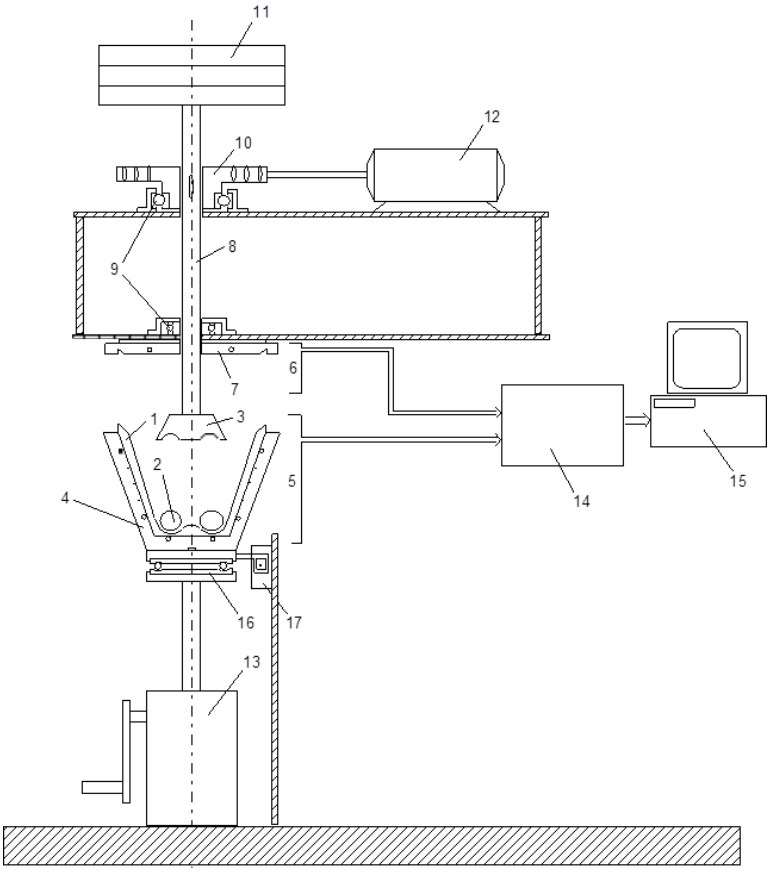

Figure 1
Schematics of the Universal Hardgrove mill

According to the standard Hardgrove protocol 50 g prepared sample, namely only the x = 590… 1190 μm particle size fraction is fed into the grinding chamber. There are eight 25.4 mm diameter balls in there. The vertical force on the grinding balls is set constant to be 290 N. The constant revolution number of the rotor is 20 1/min and a grinding lasts until 60 full revolutions. After grinding, the ground solids are removed and sieved in a Retsch sieving machine for 20 minutes using a 0.075 mm

aperture size screen. The mass of the fine fraction (m_{75}) is measured in gram unit and the Hardgrove index is calculated by Equation 1. However, the Hardgrove index (H) is widely used in the industry, this index characterises the specific energy need only indirectly. Csőke et.al. (2013) suggested a simple conversion equation (Equation 2) by with the Bond index ($W_{B,H}$) can be calculated from the Hardgrove index.

$$H = 16 + 6.93 \cdot m_{75} \tag{1}$$

$$W_{B,H} = \frac{468}{H^{0.82}} \tag{2}$$

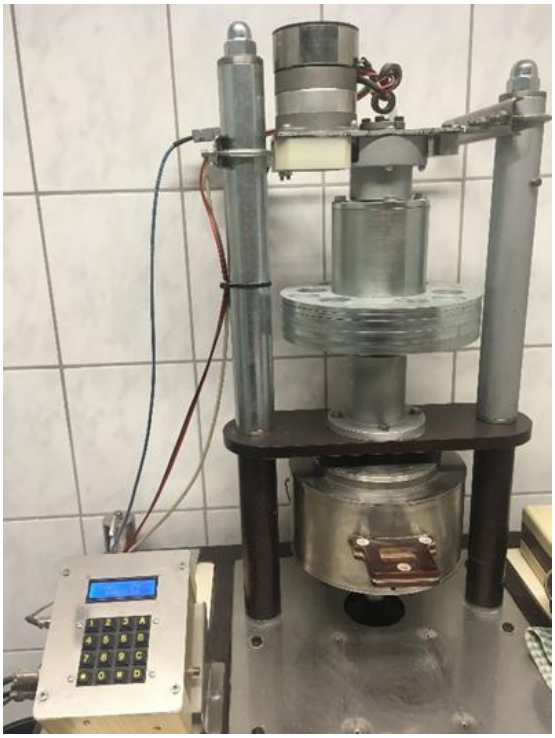

Figure 2
Photo of the upgraded newly built Universal Hardgrove mill

Powder flow properties were measured in a FreemanTech FT4 powder rheometer according to the so-called Specific Energy (SE) protocol. SE is a measure of how powder flows in an unconfined or low-stress environment. It is calculated from the energy required to establish a particular flow pattern in a conditioned, precise volume of powder. This flow pattern is an upward clockwise motion of the blade, generating gentle lifting and low-stress flow of the powder. The powder samples were placed into the 25 mm diameter and 60 mm height sample holder. The shape of the blade is shown in Figure 3.

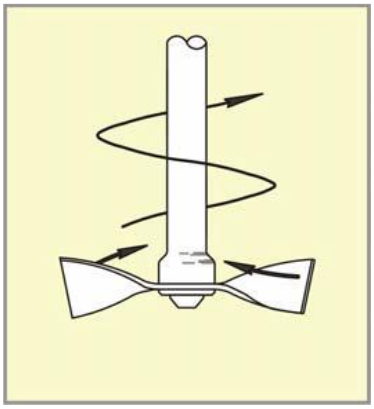

Figure 3
Shape of blade of SE tests

During each SE tests 8 test cycles were done, and the tip speed of the blade was always constant 100 mm/s. One test cycle contained first a total down and an upward moving of the blade into the powder bed for conditioning purposes without measurements. Afterward, the blade moved down again, and measurement started when the blade started to move up again. Since the revolution number and torque were measured, the total energy that the blade needed for the total upward movement was calculated by the data acquisition software by numerical integration. The measured SE values as a function of the 8 consecutive test cycles can be considered as the function of powder flow and cohesion and the friction angle can be determined as the energy axis intersect and slope of the fitted straight line.

The rheological properties of the suspensions were measured in an Anton-Paar Physica MCR51 rotational rheometer using a cylinder – cylinder measuring system with a 40 mm diameter bob and 0.5 mm Couette gap when the necessary sample quantity for one test was 50 cm^3. The revolution number of the bob was set when the shear rate was gradually decreased from 1000 1/s down to 100 1/s. The data acquisition system of the rotational rheometer records the measured torque and set revolution values and calculates the pseudo shear rate and pseudo shear stress values, namely the points of the pseudo shear curve. Afterwards, the rheological model and the parameters can be determined by curve fitting.

3. RESULTS AND DISCUSSION

During the systematic tests two different materials, limestone (LS) and quartz (QA) and five initial moisture contents were tested. Moisture contents of 0, 10 and 20 m/m% can be considered as dry grindability tests and the ones of 50 and 70 m/m% can be considered as wet tests. The exact moisture contents were set by drying and wetting before the Hardgrove tests. After the Hardgrove tests the ground samples were dried at 105 °C until mass equilibrium, because without this, sieving with the 0.075 mm opening size screen was not feasible. This simple operation just shows

why the moisture content is not considered during regular Hardgrove testing. The results of the Hardgrove tests are shown in Table 1.

After the Hardgrove testing the entire fine (<0.075 mm) and coarse fractions were mixed again and the Specific Energy (SE) tests were performed. Figure 4 shows the sample holder of the FT4 powder rheometer with a quartz sample when the blade was rotated in it.

Figure 4
Sample holder of SE testing

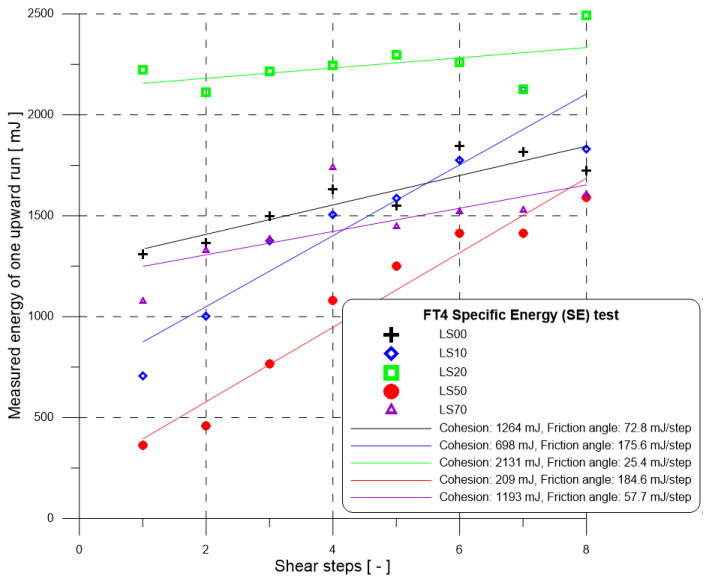

Figure 5
Specific energy as function of test cycles of limestone SE tests

Figure 4 illustrates what the problem was with the SE tests of quartz. The particulate system was a little too coarse for the device and the powder was gradually dug up by the blade. The carrying out of quartz SE tests was not feasible, but with limestone it was without problems. Figure 5 shows the measured powder flow points and fitted flow curves of the limestone SE tests. The results of linear curve fitting and the measured Hardgrove indices, cohesions and friction angle values – based on Figure 5 – are shown in Table 1.

According to Table 1, grindability is strongly influenced by the initial moisture content. It is well known in the literature that sieving at 15 m/m% moisture content is critical because the capillary force between the adjacent particles is the highest in such cases, practically materials with such moisture content cannot be sieved. Above 20 m/m% moisture content, wet sieving has occurred. At the so-called dry grinding range (0 and 10 m/m%) of quartz the measured Bond grindability indices are considerably higher because the particles with themselves and with the balls are bonded by the capillary forces. At wet quartz grinding (20, 50 and 70 m/m%) the required energy is lower, because the inter-particle bond decreases but the particles still can be bonded to the surface of the balls.

Table 1

Results of the Hardgrove and SE tests

Mark of sample	**H index –**	**$W_{B,H}$ Wh/t**	**Spec. work Ws/50g**	**Coh. mJ**	**Frict. angle mJ/step**
LS00	58.48	16.7	26.8	1264	72.8
LS10	57.93	16.8	26.8	698	175.6
LS20	70.26	14.3	26.8	2131	25.4
LS50	71.51	14.1	26.7	209	184.6
LS70	70.75	14.2	26.8	1193	57.7
QA00	47.05	19.9	26.7	–	–
QA10	42.47	21.6	26.7	–	–
QA20	51.07	18.6	26.7	–	–
QA50	54.05	17.7	26.8	–	–
QA70	53.70	17.9	26.8	–	–

Probably, grinding also deteriorates at extremely high moisture contents because particles cannot be bonded to the balls anymore. From these observations the conclusion must be drawn that the Hardgrove grindability testing should be carried out at the actual moisture content of industrial grinding, especially when the measured values are used for on-line grinding regulation. Regarding the limestone grindability tests similar conclusions can be drawn except that the adhesive limestone can be efficiently ground at 70 m/m% moisture content too, because limestone can still be bonded to the balls.

After the powder flow tests the same material was used for the rotational rheometer tests. Because of the Couette gap width (0.5 mm) between the cylinders and according to our earlier experiences, particles typically coarser than 0.16 mm should not be measured in the MCR51 rotational rheometer with this measurement system. This is a general rule of sampling and test methodology, that the smallest size of the equipment should be at least three times the typical particle size ($L_{min} \geq 3 \cdot X$).

Table 2

Results of rheological tests of limestone samples

Original sample	**Volumetric concentration %**	**Absolute viscosity mPas**	**Absolute viscosity (repeated) mPas**
finer than 0.16 mm			
LS10	2.2	4.0	3.9
	4.4	4.0	4.1
LS20	2.2	4.0	4.0
	4.4	4.2	4.1
	6.7	4.4	4.4
LS70	2.2	3.9	4.0
	4.4	4.0	4.0
	6.7	4.3	4.3
finer than 0.5 mm			
LS70	16.3	4.6	4.4

Therefore, the solids were sieved again, but now with a 0.16 mm aperture size screen. Unfortunately, this method decreased the quantity of fine solids; therefore only low solids concentrations could be measured. There is one exception, in the case of the LS70 solids a higher concentration and the <0.5 mm fraction were measured successfully, but this result has to be handled with care (the simple sampling rule of $L_{min} \geq 3 \cdot X$ was not satisfied in this single case). Table 2 shows the results of rheological tests of limestone samples; these low concentration suspensions were Newtonian fluids with low absolute viscosity values. Table 3 shows the results of rheological tests of quartz samples.

It is well seen that the many sample operations with the ground solids (drying, sieving, SE testing, sieving, mixing) probably destroyed the original effect of Hardgrove testing or there is no such effect in this case. The measured absolute viscosity values follow the well-known Einstein concentration-viscosity relation for dilute fine suspensions.

Table 3

Results of rheological tests of quartz samples

Original sample	**Volumetric concentration %**	**Absolute viscosity mPas**	**Absolute viscosity (repeated) mPas**
finer than 0.16 mm			
QA00	2.2	4.0	4.0
	4.4	4.0	4.0
QA10	2.2	4.1	4.1
	3.0	4.1	4.1
QA20	2.2	4.1	4.1
	4.4	4.1	4.1
QA50	2.2	4.0	4.0
QA70	2.2	4.0	4.0

4. CONCLUSION

The carried out wet mode grindability testing has proved that the moisture content is also a very important technological parameter. At the so-called dry grinding range (0 and 10 m/m%) the measured necessary grinding energy was typically higher, at wet grinding (20, 50 and 70 m/m%) the required energy was lower. 50 m/m% moisture content resulted in the lowest grinding energy need. The same trends were observed for both model materials, namely for the limestone (soft adhesive) and the quartz (hard non-adhesive).

Two important phenomena were revealed, namely that the places of capillary force acting among the particles and among the particles and the balls are also important and opposite effects can be observed in the two places. The particle-particle bonds are typically not advantageous because they deteriorate grinding; however, particle-ball bonds are advantageous because in ball and ring mills it helps for the formation of more stressing events.

It was also concluded that on-line grindability testing for technological regulation should be done at a moisture value equal to the actual moisture content of the material in the industrial equipment.

This study also has revealed that further measurement methodology development is also necessary. Just think about the problem when Hardgrove grindability is measured in the 10–20 m/m% moisture content range, but sieving at this range is impossible, because of the high capillary forces. Measurement technique difficulties were also found at the powder flow and the rotational rheometer testing, but it is thought that this initial work can pave the way for later developments.

ACKNOWLEDGMENTS

This project is funded by the European Union's Horizon Europe program under grant no. 101079354 (CiRCLETECH Project).

REFERENCES

Csőke B., Faitli J., Hatvani Z., Solymár K., Papanastassiou D.: (2003) New test method for investigation of grindability in alkaline media at high temperature. In: Leon, Lorenzen (ed.) Proceedings of the *XXII International Mineral Processing Congress, South African Institute of Mining and Metallurgy (SAIMM)*, pp. 434–441.

Csőke B., Rácz Á., Mucsi G. (2013) Determination of the Bond work index of binary mixtures by different methods. *International Journal of Mineral Processing*, Vol. 123. pp. 78–86. DOI: 10.1016/j.minpro.2013.05.004

Deniz V. (2022a) A new model between the Bond and Hardgrove grindability based on volumetric powder filling by using limestones. *Minerals Engineering*, Vol. 179.107444, pp. 1–9. DOI: 10.1016/j.mineng.2022.107444

Deniz V. (2022b) The effects on the grinding parameters of chemical, morphological and mineralogical properties of three different calcites in a Hardgrove mill. *Minerals Engineering*, 176.107348, pp. 1–10. DOI: 10.1016/j.mineng.2021. 107348

Faitli J., Bohács K., Mucsi G. (2016) Online Rheological Monitoring of Stirred Media Milling. *Powder Technology*, Vol. 308. pp. 20–29. DOI: 10.1016/j.powtec.2016.12.021

Mucsi G., Csőke B., Faitli J., Solymár K.: (2006) Grindability tests in heated Bond mill. In: Önal, Güven (ed.) Proceedings of the *XXIII. International Mineral Processing Congress*, Istanbul, Turkey. pp. 87–90.

Vuthaluru H. B., Brooke R. J., Zhang D. K., Yan H. M. (2003) Effects of moisture and coal blending on Hardgrove Grindability Index of Western Australian coal. *Fuel Processing Technology*, Vol. 81. pp. 67–76. DOI: 10.1016/S0378-3820 (03)00044-4

Tarján G.: (1981 and 1986) *Mineral processing 1 and 2*. Akadémiai Kiadó, Budapest.

Yang Y., Hea Y., Bi H., Grace J.R., Wanga H., Fotovat F., Xie W., Wang S. (2020) Effect of moisture on energy-size reduction of lignite coal in Hardgrove mill. *Fuel*, Vol. 270.117477. pp. 1–7. DOI: 10.1016/j.fuel.2020.117477

Geosciences and Engineering, Vol. 13, No. 1 (2025), pp. 69–87.
https://doi.org/10.33030/geosciences.2025.01.006

URBAN MINING COMMINUTION TECHNOLOGICAL APPLICATIONS AS THE MOST IMPORTANT PART OF CIRCULAR ECONOMY, A REVIEW

JÓZSEF FAITLI[1, *], MIAA JOHN[2], IMRE GOMBKÖTŐ[3], EVELIINA REPO[4]
[1, *]*University of Miskolc, Hungary; jozsef.faitli@uni-miskolc.hu*
[2]*Lappeenranta-Lahti University of Technology, Finland; Miia.John@lut.fii*
[3]*University of Miskolc, Hungary; imre.gombkoto@uni-miskolc.hu*
[4]*Lappeenranta-Lahti University of Technology LUT, Finland; Eveliina.Repo@lut.fi*
[1]*https://orcid.org/0000-0002-4037-5208*
[2]*https://orcid.org/0000-0002-6015-0735*
[3]*https://orcid.org/0000-0002-4683-2510*
[4]*https://orcid.org/0000-0002-6006-3631*

Abstract: Mankind needs materials for civilisation. The earth sciences & engineering (exploration, extraction and processing of natural and anthropogenic resources) has been supplied raw- and commodity materials for production. Recently, it is evident that a better management with natural resources is necessary and therefore the concept of circular economy was born. Its first leg is the system level optimization of the production – consumption cycle by optimal energy usage, circular-minded design, and circular-minded behaviour of the society, optimised and elongated use of products, re-use, re-manufacture and so on. However, as the name circular economy implies the second leg, namely the circulation of the materials is the most important element. The concept of urban mining means the mining and processing, therefore reclaiming compounds and elements from any kind of anthropogenic origin stocks, including buildings, infrastructure, industries and products (in and out of use). This review paper compiles examples from the literature showcasing industrial applications of urban mining waste-to-material recycling, focusing on cases where mechanical processing of man-made raw materials is essential, thus necessitating comminution and classification processes. Flow types of anthropogenic raw materials are reported to EU authorities regularly, therefore subcategorization of waste types follows the EU nomenclature. Characteristic comminution machines and main types of stressing and in some cases characterising separation units are presented which are illustrated by a few selected application examples.

Keywords*: circular economy, urban mining, stock and flow types of anthropogenic raw materials, waste crushing and grinding*

1. INTRODUCTION AND AIM

The challenges to the sustainability of human life on earth have intensified in recent times, as it has now become generally evident that it is under threat. As an answer for sparing and managing natural resources, the concept of the circular economy and urban mining was born. The scientific vocabulary of these relatively new areas was clarified probably by Cossu and Williams (2015). According to Cossu and Williams (2015) the terminology Landfill Mining represents the activities involved in

extracting and processing wastes which have been previously stocked in particular kinds of deposits (municipal landfills, mine tailings, etc.). Urban Mining extends landfill mining to the process of reclaiming compounds and elements from any kind of anthropogenic stocks, including buildings, infrastructure, industries, products (in and out of use), and environmental media receiving anthropogenic emissions. Circular economy is even a much wider term, because it covers all the economic and social impacts too, including how to design fully recyclable products and so on, meaning everything that facilitates the real material circular flow. Figure 1 illustrates a material balance on Earth. The two legs of the circular economy and the scientific vocabulary are clearly visible on this figure. For human civilisation materials are needed, and the earth sciences & engineering - meaning the exploration and extraction of natural- and anthropogenic resources and the processing of the mined virgin- and secondary raw materials - supplies all the necessary geogenic origin materials for mankind.

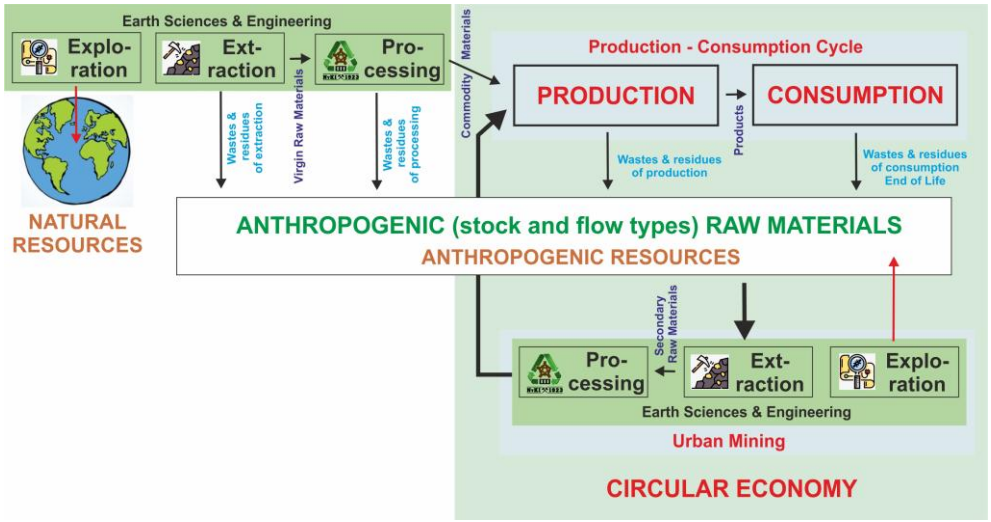

Figure 1

Urban mining as the most important part of the circular economy

In the English-speaking world, the terms “raw materials” and “commodity materials” are generally not distinguished; however, the role of mineral- and waste processing cannot be well explained without this. Mineral processing upgrades the mined virgin raw materials and produces commodity materials for production. Similarly waste processing upgrades the mined secondary raw materials and produces commodity materials also. The first leg of the circular economy falls into the system level optimization of the production – consumption cycle and this is a really wide area. It necessitates optimal energy usage, circular-minded design, and circular-minded behaviour of the society, optimised and elongated use of products, re-use, re-manufacture and so on. However, we still think that the most important part of the circular economy is the second leg, namely how we can gain raw materials from

anthropogenic resources by urban mining and inside this the real challenge is not the waste mining but rather how the waste is processed. Unfortunately, wastes are typically multi-material systems and this is where the challenge lies. The stocked materials may represent a significant source of resources, with concentrations of elements often comparable to or exceeding natural stocks. A definition distinguishing between "stock" and "flow" resources, either anthropogenic or natural is necessary. The origin of natural stocks can be either geogenic or biogenic and many times geogenic natural stocks are called "virgin" (Winterstetter et. al. 2016). Annual stocks of materials held in geological deposits, groundwater reservoirs, household and industrial buildings, infrastructure and scrap products may not vary much over time. However, annual flows of materials may change considerably from year to year, depending upon the prevailing economic situation, fashion, technical innovations, etc. Nevertheless, from both anthropogenic stock and flow resources, secondary raw materials are produced. Resource Recovery includes materials recycling as well as the energy that can be generated by treating and managing wastes (waste-to-energy recovery). Materials Recycling (or waste-to-material recycling) aims to transform selected wastes into materials that can be used again in the manufacture of new products. The mining and processing of virgin geogenic raw materials have always been with us for as long as humans have lived, since without materials there can be no civilized life on earth.

Therefore, the current task is to transfer the known technologies of mining and mineral processing to the field of urban mining including waste processing. The first comprehensive paper applying this concept was probably written by Ambros (2023). Ambros (2023) reviewed the typical gravity concentration units and their applications in mineral processing and then investigated the possible applications of that mechanical process for waste upgrading. Another new scientific term we have to learn is the Distinct Urban Mine (DUM). The materials and resources recoverable from individual urban spaces differ. The uniqueness of an urban mine is due to factors such as the composition and concentration of post-production and post-consumption materials of interest as well as the demographic profile of the urban space. This delimited space, unique in its material composition and concentration is called a Distinct Urban Mine (DUM) (Ongondo et. al. 2015). As with a traditional mine, a DUM requires prospection to determine its viability. Information such as size, concentration of materials and grade of resources of interest and its location within the wider anthroposphere is necessary. According to Ambros (2023) the miners of the present will gradually become recyclers in the future since there will be more copper, iron, and zinc (and other metals) in the cities than in the earth's crust after 2050 (considering current known reserves).

Taking this introduction into account it was concluded that a review of technological applications of comminution and classification in the field of urban mining could be useful for the scientific community. Data on the continuously generating wastes, by-products and other residues, namely the flow types of anthropogenic raw materials are reported to the national and EU authorities regularly, therefore it is aimed first to give a summary of these statistical waste categories and sub-categories

according to the EU nomenclature. Then focusing only on the waste-to-material recycling the characteristic comminution machines and main types of stressing and in some cases characterising separation units are presented which are illustrated by a few selected application examples. The typical upgrading concept is well-known in mineral processing. Every time mechanical pre-processing is needed, namely comminution and classification are necessary to release the valuable components and generate narrowly distributed particle size or shape fractions, as they enable effective upgrading. Then if there is a difference in any intrinsic feature of the component materials, the materials can be upgraded by physical separation when different particles go into products because of forces, namely concentrates – rich in the useful components – and tailings – hopefully poor in the useful components – can be produced. If the particles of the feed of different materials are sorted by manual- or sensor-based sorting (SBS), this kind of upgrading requires mechanical pre-treatment also. After the mechanical pre-upgrading – when the big mass of non-useful components has been discarded – mechanical-, chemical-, thermal- or biological processes can be used for the extraction of the useful components. Without mechanical pre-concentration, it is certain that no subsequent non-mechanical waste recycling process can be economically viable. Therefore, the role of comminution is very important for urban mining.

Before going further, let's review the conclusions of Ambros (2023) about the three competing upgrading processes (upgrading at density, SBS and froth flotation), because similar conclusions are expected for the comminution. Most plastics, due to their low density and hydrophobic properties, may be considered as the urban mining equivalent of coal in mineral processing. Therefore, methods like jigging, countercurrent flow separation and dense media separation can effectively separate polymers when the material feed is adequately liberated. Centrifuge gravity separation also shows potential for isolating microplastics from soil and sediments (Ambros, 2023). Gravity concentration is promising for producing recycled aggregates from construction and demolition waste (CDW), especially for coarse aggregates (>4.75 mm). However, processing fine CDW (<4.75 mm) remains underexplored, possibly due to direct applications in backfilling and geotechnical fields (Ambros, 2023). And most importantly, gravity separation is increasingly challenged by two fronts: sensor-based sorting (SBS) in the processing of coarse materials and froth flotation in the treatment of fine-sized materials. However, there is an intermediate size range (about 0.75-5 mm) where these techniques face technical difficulties and in which gravity separation typically excels, particularly for treating construction and demolition waste (CDW) and microplastics. Also, SBS (sensor-based sorting) typically can effectively sort particles within a limited range of sizes, with a recommended maximum size ratio of about 3 between the smallest and largest particles (Ambros, 2023). This is why classification is important.

As the last element of the introduction, a short summary of comminution machine names is necessary, however this is widely applied and generally known. If comminution happens on the size range of coarser than about 0.5-1 mm, the process is called crushing and the machines are called crushers, for a smaller size range the process is

called grinding and the machines are called mills. The minerals are typically brittle materials and therefore jaw, gyratory, cone, roll, impact, hammer and other crushers can be applied for crushing and ring, ball, planetary, vibrated, stirred media and other mills can be applied for milling in mineral processing. Generally speaking, wastes are typically non-brittle materials, therefore rotary shears, rotary cutters, rotary shredders and translatory shears can be applied for waste processing.

2. FLOW TYPES OF SECONDARY RAW MATERIAL STOCKS

According to EU statistics, 776.3 million tons of waste was generated, excluding major mineral waste in the EU in 2020 (Eurostat online data code: env_wasgen). At the time of generation, this whole mass of waste can be considered as a flow type of anthropogenic secondary resource. It consists of solid wastes as 25.2% household wastes; 21.5% manufacturing wastes; 11.5% other sectors' wastes; 5.9% energy wastes; 5% construction wastes; 2.7% agriculture, forestry and fishing wastes; 1% mining and quarrying wastes and non-solid 27.4% wastewater. Some of this waste mass will be charged in deposits and landfills and later that will become a stock type of resource. Table 1 shows comminution and classification waste-to-material recycling application examples according to the subcategorization of the generated solid wastes.

2.1. Agriculture, forestry and fishing wastes

Total waste generation by entities of Section A – Agriculture, forestry and fishing – in EU countries in 2016 was about $2.6 \cdot 10^9$ tonnes, meaning an average 40 kg/capita waste generation (Komor and Bujanowitz-Haras, 2019). **Agriculture waste** comprises Crop waste (rice husk, wheat straws, sugarcane bagasse), Animal waste (animal excreta, dead animals), Processing waste (packaging material, fertilizer cans) and Hazardous waste (pesticides, insecticides). Typical agricultural waste recycling processes are composting (producing nutrient-rich compost), biogas generation (digesters convert waste into biogas and that is an energy source), mulching (solid waste can be used as mulch to protect the soil), biomass conversion (thermo- and biochemical conversion of the waste into valuable products) and the recycling of packaging materials (Yang et. al. 2021). A variety of comminution machines of brittle and non-brittle materials are used for recycling agricultural wastes but only on a small scale, mainly as auxiliary pre-processes. For crop waste comminution hammer crushers or mills can be applied because the beating, impacting and shearing types of stressing are beneficial in this case. For animal waste comminution, axial gap rotary shears are beneficial because of the shearing and tearing stress.

Table 1

Summary of waste sub-categories and examples for their recycling options and applied comminution equipment

Waste category	Waste sub-category	Recycling option examples	Comminution and classification equipment	Types of stressing
Agriculture, forestry and fishing wastes	Agriculture (crop) waste	Composting. Biogas generation. Biomass conversion (thermo- and biochemical conversion)	Hammer crushers Hammer mills	Beating impacting shearing
	Agriculture (animal)	Using the useful parts and disposing of the residues	Axial-gap rotary shears	Shearing tearing
	Forestry	Mulching (solid waste can be used as mulch to protect the soil) Waste-to energy recovery Decomposition	Swing hammer mills Cutting mills (tip point speed can reach 100 m/s)	Cutting shearing
	Fishing	Producing value-added products e.g., peptides, proteins, collagen, chitin, oil. Procedures as acid extraction, enzymatic hydrolysis and fermentation.	The role of mechanical pre-processing by comminution and classification is not so important for this waste stream.	
Mining and quarrying wastes and metallurgical slags	Mining and quarrying wastes	Waste rock (materials overlying). Overburden (low grade minerals) and Beneficiation wastes (residues of mineral processing) Primary aim: producing secondary raw materials.	Full spectrum of brittle materials comminution equipment. Crushers: Jaw, gyratory, cone, roll, impact, pin mill, hammer, hammer shredder. Mills: ring, media, planetary, vibrated, stirred media, jet, cutting, SAG, attrition mills, tower mills, HPGR (high pressure grinding rolls).	Compressing beating impacting shearing
	Metallurgical dusts and slags	Recovery of the valuable metals by hydro-, pyro- or bio-metallurgical processes after mechanical pre-processing. Complex utilisation. Producing cement additives.	Grinding: media mills, namely ball mills, autogenous mills (AG) and pebble mills. Ring mills for blast furnace slag.	Compressing, shearing
Manufacturing	Production specific, non-production specific	Quality assurance discarded. Technological (e.g. red mud of alumina production). Amortization wastes. Non-production-specific wastes.	Bring these materials back into their own production system. All types of wastes so all types of comm. equipment.	

Wastes of energy production	Residues of fuels incineration. (coal combustion-CCR, waste incineration residues)	CCRs is being used in cement, cellular concrete, fly ash lime bricks, fly ash lime gypsum block, building tiles; as admixture in cement concrete, timber substitute products; as aggregate in concrete, road and building block; as pozzolana.	Tumbling ball mill or high energy density mill (HEM) like the planetary ball mill, vibratory mill or stirred media mill.	Compressing shearing
	Residues of solar energy generation	c-Si PV modules: dismantling, shredding, SBS upgrading, pre-concentrates go to distinct waste recycler. FirstSolar and ANTEC Solar GmbH technologies for CdTe PVmodules. Shredding, slow leaching drum, glass separation, sodium hydroxide precipitation of metal compounds.	Specialised hammer crushers hammer mills	Beating impacting shearing
	Residues of wind energy generation	100 % waste-to-material recycling is possible.	Suitable comminution eq. for steel, Al, Cu, polymer materials, concrete, etc…	
	Residues of nuclear energy generation	Reprocessing of Spent nuclear fuel (SNF) by fission and activation products, and so-called minor actinides producing high-level solid packed waste (HLW).	Comminution is not applied typically	
Construction & Demolition wastes (CDW)	Excavated soil	Processed CDW and composted eucalyptus bark (CEB) were used at lab scale to make new soil.	Typically on-site handling with normal soil excavators.	
	Concrete aggregate	Producing recycled concrete aggregate (RCA). Producing controlled Low-Strength Materials (CLSM). Producing new binders.	Multiple stages. 1st stage: horizontal axis jaw crushers and beater rolls.2nd stage: Cone crushers, impact crushers	1 Compr. bending. 2 Compr. impacting.
	Asphalt aggregate	Producing Recycled asphalt aggregate (RAA) or Pyrolysis RAA.	Toothed rolls and hammer crushers	Shearing beating
	Wood waste	See forestry waste		
	Metal waste	Metallurgical processing	Guillotine shears, alligator shears	Shearing
	Mixed CDW	Removing contamination. Production of new construction materials. Production of lower utilization fills materials.	Crushers for brittle materials comminution.	Compressing shearing

Post-consumer wastes	Municipal solid wastes (MSW)	Waste-to-material recycling of SMSW and some RMSW. Waste-to-energy recovery. RDF (refuse derived fuel). Biomass conversion.	Axial gap rotary shear and swing type hammer shredder. For RMSW: Low-speed rotary shredders for pre-shredding and radial gap rotary shears for final.	Shearing and complex tearing stress
	EoL Rubber tyres	Waste-to-material-recycling or energy recovery	Multiple stages: Steel cords removing by hook, axial gap rotary shears, then radial gap rotary shears and finally cutting mills.	Shearing cutting
	EoL Batteries	Extracting precious and structural components	Hammer shredders. Issues: fire and explosion hazard, hazardous dust emission	Tearing
	EoL Refrigerators	Waste-to-material recycling. Issue: Freon gases.	Hammer shredders. Chains can serve as hammers. Nitrogen atmosphere.	Tearing
	EoL Vehicles	Waste-to-material recycling. Waste-to-energy recovery.	High mass swinging hammer shredders	Tearing
	WEEE (electric and electronic waste). EoL TV devices. EoL Computers.	Extracting precious and structural components	Hammer shredders and hammer crushers. PCB - high-speed hammer crusher and beater mill.	Tearing shearing beating

Regarding **Forestry wastes,** the conventional treatment of agroforestry waste includes landfilling, thermal management, and decomposition which is accompanied by their own share of disadvantages (Gupta et. al., 2022). To date, mills used for comminuting lignocellulose have been developed for materials with brittle material properties, whereas biogenic materials show almost brittle to viscoelastic properties. It has not yet been clarified whether the principles applicable to brittle materials can be utilized for the comminution of renewable raw materials. Developing new comminution machines for this purpose and enhancing energy efficiency to achieve necessary particulate sizes and properties for subsequent processes is of the utmost importance (Eisenlauer and Teipel, 2020). For wood comminution cutting mills with the main stress type cutting and shear stress and swing hammer mills with mainly impact stress can be used (Eisenlauer and Teipel, 2020). Sometimes, the peripheral speed of hammer mills' tip point applied for wood comminution can reach 100 m/s.

Fishing (fish) waste is not only a major environmental problem, but also a huge economic loss. For this reason, a better fish-waste management is needed to overcome these important issues. The use of fish by-products could contribute to the development of products with high commercial value, and consequently, to economic growth. Fishing wastes could become an enormous resource for the production of value-added products e.g., peptides, proteins, collagen, chitin, oil and enzymes with several potential applications. The extraction and purification techniques are mainly based on procedures as acid extraction, enzymatic hydrolysis and fermentation (Coppola et.al., 2021). The role of mechanical pre-processing by comminution and classification is not so important for this waste stream.

2.2. Mining and quarrying wastes and metallurgical slags

Mining and quarrying wastes are typically produced during ferrous metals -, non-ferrous metals – industrial minerals –, and coal mining and processing. Millions of tons of waste rock (materials overlying the area to be mined and which are moved in order to gain access to the orebody), overburden (low-grade minerals) and beneficiation wastes (residues of mineral processing) are produced by the global mining industry (Matinde et. al. 2018). The mining sector produces commodity raw materials for the production and the liberation of the useful minerals requires comminution (crushing and grinding). Comminution is more effective by the application of open and closed comminution and classification cycles and it is really important because of the high energy demand of this process. The comminution – only in the mining sector – requires about 1% of the world's total generated energy (Jeswiet and Szekeres, 2016). As it is widely recognised the energetic efficiency of comminution plays a crucial role, because a slight efficiency increase represents considerable energy saving. The full spectrum of brittle materials comminution machines from coarse crushing, from the jaw crusher towards grinding to fine- and ultrafine grinding with stirred media mills is used for mineral processing and these units can be mainly applied for the recycling too of these waste streams. This topic is really widely covered in the literature (Jeswiet and Szekeres, 2016; Matinde et. al. 2018).

Metallurgical dusts and slags, in 2020, world iron slag production was estimated to be between 310 million and 380 million tons, and steel slag production was estimated to be between 180 million and 270 million tons. The yield of copper slag reaches nearly 70 million tons each year worldwide. The residues and by-products of metallurgy still typically contain some valuable metals and some hazardous elements. It means that the freshly generated wastes and the stocked ones in deposits represent an environmental hazard and a potential secondary raw material at the same time. The primary aim of metallurgical dusts and slags recycling is the recovery of the valuable metals by hydro-, pyro- or bio-metallurgical processes (Tian et. al. 2021). That is also typical that only the valuable metal content recycling is not economical the higher mass ratio of other components utilisation has to be also implemented. This is the well-known complex utilisation. As an example copper slag can be used for construction of the top layer, base course and substructure of roads where it can be used as soil or aggregate, unbound, bituminous or hydraulically bound. Other target utilisation of metallurgical residues is a kind of construction industry or geotechnical usage, such as cement or concrete additive or other forms (Klaffenbach et. al. 2023). The applied most important comminution application of metallurgical residues recycling is the grinding; media mills, namely ball mills, autogenous mills (AG) and pebble mills are generally used (Metin Can and Mercan, 2023). The most important direct utilisation of granulated blast furnace slag is the cement additive application. Ring mills with stress-type of material bed compression are typically applied on-site for the residue's processing.

2.3. Manufacturing wastes

Manufacturing waste refers to the materials left over during the production process of new products. Other names for this type of waste include factory waste, industrial waste, construction waste, and production waste. Wastes of producers and service providers can be subdivided as production-specific wastes (QA – quality assurance – discarded or bad products, technological e.g. red mud of alumina production or slag of iron production and the amortization – worn out production machines). Non-production-specific wastes (e.g. packing materials, office paper and office computer) are also generated during production, but these wastes are characterised into other waste streams in this paper. More than two-thirds of manufacturing waste originates from biological sources, such as sludge from wastewater and inedible food waste. There are various reasons behind QA defects in mid-production products in different industries. Some examples are: pharmaceutical industry (failed stability testing, contamination, incorrect labelling), food production (microbiological contamination, chemical contamination and allergen cross-contamination), technology production (functionality testing, quality control defects and safety testing), automotive (durability testing, quality control checks, safety standards). The primary aim of production-specific waste utilisation is to bring these materials back into their own production system. If it is not possible their materials should be used as raw materials for other products production. Since the entire production scale is very extensive, so is the scale of waste materials generated; therefore all the different brittle (mineral like)

and non-brittle types of waste materials occur. Typical recycling technologies for typical waste materials are described for the other waste streams in the paper.

2.4. Wastes of energy production

Energy production is essential for humanity and right now that results huge mass of waste and residues generation. According to a recent study (Mirletz et.al., 2023) the specific waste generation ratio of the main energy-producing sectors will be as follows up to 2050. The percentage of each sector is determined as mass percentage. Fossil fuels incineration and waste-to-energy residues (97.95%), EoL solar panels - PV (1.84%), wind energy residues, mainly EoL turbine blades (0.18%) and nuclear energy generation residues, mainly spent or unprocessed fuel (0.03%).

Residues of fuels incineration: Coal and lignite-fired power plants residues are called "coal combustion residues" (CCR) and these typically include the fly ash separated in different stages of the flue gas cleaning system, bottom ash and boiler slag. It is generated in an enormous high quantity worldwide, almost 800 million tons/year. The major utilisation of CCR is in cement, concrete, bricks, wood substitute products, soil stabilisation, road base/embankment, and consolidation of ground, land reclamation and for agriculture. CCRs is being used as a raw material in cement, cellular concrete, fly ash lime bricks, fly ash lime gypsum block, building tiles; as admixture in cement concrete, timber substitute products; as aggregate in concrete, road and building block; as pozzolana in lime pozzolana (Asokan et. al., 2005; Mucsi, 2016). The mechanical activation of CCR is a promising technology and that significantly increases the waste-to-material recyclability of this waste stream. The combined utilisation of mineral processing wastes with CCR is also a promising new area. Equipment of mechanical activation might be the traditional tumbling ball mill or high energy density mills (HEM) like the planetary ball mill, vibratory mill or stirred media mill (Mucsi, 2016; Mucsi et. al., 2019). It is an interesting situation that the residues of the waste-to-energy utilisation of many waste streams, such as the municipal solid wastes (MSW), other combustible wastes, hazardous wastes are also potential secondary raw materials and represent hazard to the environment too. The processing and the application of waste incineration residues might be similar to CCR. As an example, MSW fly ash and slag can be utilised as precursors in low-range alkaline cements after mechanical activation by grinding (Cristelo et. al., 2020).

Residues of solar energy generation: at the end of 2016, the cumulative global PV waste reached 250,000 metric tons, while it is expected that by 2050 that figure will increase to 5.5–6 million tons. Much PV waste currently ends up in landfills. Given the heavy metals present in PV modules, e.g. lead and tin, this can result in significant environmental pollution issues. However, because of the valuable components like silver and copper, methods for recycling solar modules are being developed worldwide. The recycling process of c-Si PV modules (crystalline silicon) begins with the removal of the cables, junction box and frame from the PV module. Then, the module is shredded and the liberated structural components are upgraded by sensor-based sorting. For PV panels shredding specialised hammer crushers are used, when the basic machine is optimised for this waste stream. The separated waste

materials are then sent to specific recycling processes associated with each material. According to the FirstSolar and the ANTEC Solar GmbH developed technologies the recycling of the CdTe PV modules process starts with the shredding of the modules into large pieces and subsequently in to small fragments (5 mm or less) by a hammer mill. During the next 4–6 h the semiconductor films are removed in a slow leaching drum. The remaining glass is exposed to a mixture of sulfuric acid and hydrogen peroxide aiming, to reach an optimal solid–liquid ratio. After that process, the glass is separated again. The next step is to separate the glass from the larger ethylene vinyl acetate (EVA) pieces, via a vibrating screen. The glass is cleaned and sent to recycling. Sodium hydroxide is used to precipitate the metal compounds. This process recovers 90% of the glass for use in new products and 95% of the semiconductor materials for use in new solar modules (Lunardi et. al. 2017).

Residues of wind energy generation: the main EoL wind energy generation materials are ferrous and non-ferrous metals, polymers, glass and concrete (Tazi et. al., 2019). Recently, some wind turbine producers (Vestas, Siemens Gamesa) announced the production of 100% recyclable turbine blades. Carbon Rivers' recycling technology (carbonrivers.com) uses pyrolysis to break down the resins and polymers with intense heat in the absence of oxygen and separates from the inorganic fiberglass reinforcement. The process converts organic products back into raw hydrocarbon products called syngas and pyrolysis oil, which can be used for energy production. This gives the process a net positive energy output. The separated recycled glass fibre can then be cleaned and collected for direct reuse in the manufacturing of new products.

Residues of nuclear energy generation: about 440 nuclear reactors operate globally, providing approximately 10 percent of the world's electricity. Nuclear power plants (NPPs) produce negligible quantities of waste compared to other energy sources. Based on the calculations provided by the International Atomic Energy Agency (IAEA), if spent nuclear fuel (SNF) is not reprocessed, a 1000 MW(e) nuclear reactor produces around 30 tons of high-level solid packed waste annually (HLW). HLW represents high risk, therefore, proper management and safe decommissioning of HLW and SNF are the major aspects of energy production by NPPs. SNF may be considered either as waste, which will eventually be packaged and disposed of, or reprocessed to recover uranium and plutonium followed by the conditioning of residue in the form of HLW containing mainly fission and activation products, and so-called minor actinides. Several countries, instead of reprocessing the SNF, plan to dispose of it in deep geological formations. The increasing bulk of the SNF stream will be problematic as the use of nuclear power increases. Nuclear recycling is the most effective method to solve this problem. Efficient recycling of HLW from SNF decreases ~4–6% of the waste repository volume and decreases the amount of time required (by a factor of 100) during the isolation of residual waste (Alwaeli and Mannheim, 2022).

2.5. Construction & Demolition wastes

The management of construction and demolition waste (CDW) and its correct final destination has become a global problem due to the growth of urbanization. At the same time, there is a need to recover soils degraded by mining, a source of raw

material for the production of inputs and materials necessary for urbanization itself. Published in 2008, the EU decree-law 46/2008 establishes the legal framework of CDW management, including prevention, reuse, and the operations of collection, transport, storage, treatment, recovery and disposal. Some key points are: the responsibility to manage CDW belongs to the producer; uncontaminated soils and rocks must be used at the construction site or another site; CDW which cannot be reused has to be sorted at the construction site (for reuse or recycle) or delivered to a licensed waste operator; CDW landfilling is only possible after sorting and it is subject to taxation (Kamino et.al. 2019). If CDW is watched through the glasses of processing the characterising material parts are the "contaminants", namely metals, plastics, soil and woods; the remaining "useful", the brittle components (concrete aggregate, brick, ceramic, tile, etc.) and the finer particulate binding materials. It is logical to separate the "contaminants" first and process them separately using the technology according to the material. The mentioned full-scale comminution arsenal for brittle materials used primarily in mineral processing can be used for the brittle part of CDW.

Excavated soil: CDW can be used for the improvement of degraded areas by open-pit mining. According to Santos and Tubino (2021), processed CDW and composted eucalyptus bark (CEB) were used at a lab scale to make new soil for the degraded areas.

Concrete aggregate: the most important recycling option of separated concrete aggregate CDW is the production of the so-called recycled concrete aggregate (RCA) by suitable comminution and classification unit operations. The comminution typically happens in multiple stages, for coarse crushing horizontal axis jaw crushers and beater rolls can be used. Major stress of the first unit is compressing and some bending; ones of the second unit are mainly beating and some compressing. For the second comminution stage cone crushers (compressing) and impact crushers (impact) are applied. The challenge is whether the quality of the concrete made from RCA is satisfactory or not. According to McNeil and Kang (2013) the aggregate properties are most affected by the residual adhered mortar on RCA. Because of this, RCA is less dense, more porous, and has a higher water absorption capacity than natural aggregate (NA). While RCA and NA have similar gradation, RCA particles are more rounded in shape and have more fines broken off in Los Angeles abrasion and crushing tests. The other recycling target of RCA is the production of new binder or the production of concrete without cement. Fine and coarse recycled concrete aggregate (RCA) with slag or fly ash was used to produce Controlled Low-Strength Materials (CLSM) using only recycled and by-product materials without the need to add Portland cement. In addition to the hydraulic activity of slag and high-calcium fly ash (HCFA), their pozzolanic reaction was activated by the alkalis and calcium hydroxide present in the residual paste of the RCA (Achtemichuk et.al. 2009). When cement substituting materials are produced from CDW, fine grinding is necessary and lately intensive research is going on for the application of the so-called HPGR (high pressure grinding rolls) technology.

Asphalt aggregate: asphalt pavement consists of aggregates resulting in a waste material at end of its life. The aggregates can be reused as basic material for asphalt

or cementitious binding agents. In both scenarios, the recycled aggregates should provide a good bond with the binder to achieve strength. Setiadji et. al. (2022) report on the – so-called – pyrolysis method. Three types of aggregate were used: virgin aggregate (VA), recycled asphalt aggregate (RAA), and RAA after removing the thin asphalt film using the pyrolysis method, designated as pyrolysis recycled asphalt aggregate (PRAA). The Pyrolysis method is a unique new surface treatment method to remove and stabilize the residual asphalt film by heating and is expected to contribute to increasing the mechanical properties of the mortar due to an aggregate-to-mortar bond improvement. The pyrolysis method applied on RAA had a number of advantages: the compression strength increased, and the absorption decreased, reducing the formation of a water film surrounding the aggregate during the cement hydration process. The pyrolysis procedure did not have any impact on the tensile strength for both the RAA and PRAA; however, the overall tensile strength decrease was relatively low. For the comminution of waste asphalt aggregates toothed rolls and hammer crushers can be used.

Mixed C&D is now identified that some sources of mixed CDW contain a variety of potentially harmful compounds. Various building materials contain heavy metals including lead (pipe solder, paint, batteries, flashing), arsenic (treated wood), cadmium (paints, batteries), and mercury (electrical switches, lights, thermostats). Asbestos is a component of some building materials such as cement siding, roofing mastic, pipe insulation, and floor tiles. Therefore suitable recycling technologies are important (Khandani et. al., 2023). Tehran mixed CDW after the demolition of EoL infrastructure typically contains sand and cement, concrete, brick, soil, mosaic, ceramic tile, plaster, stone and other materials. After the coarse crushing with a jaw crusher of the recycled aggregate and adding 8% Portland cement as binder good quality underground mine backfilling material was made of up to 5 MPa compressive strength (Khandani et. al., 2023).

2.6. Post-consumer wastes:

Municipal solid wastes (MSW). Main types depend on the collection system, these are the one and multi-component selectively collected MSW (SMSW), such as plastic-paper-metal, plastic-paper, glass and so on, selectively collected green MSW and the residual one (RMSW). The concept of a typical mechanical RMSW processing technology starts with pre-comminution, then sieving. The so-called “bio-fraction” is the fine product of sieving, the course product goes into a multi-stage physical separation (magnetic, eddy current, flow separator, sensor-based sorting, etc.) technology. As it was pointed out earlier the comminution of brittle particles is really widely investigated and applied in mineral processing. There are standard methods, such as investigating single particle breakage events for the characterisation of the process and later designing the machine. However, the comminution of non-brittle materials – such as most of the regular post-consumer wastes – represents a new challenge. Rácz and Csőke (2021) made a pioneering work in this field carrying out repeated single particles breakage tests with real waste particles. Shear and complex tearing stresses were applied on the particles in axial gap rotary shear and swing type

hammer shredder. The results proved that the developed single-particle comminution test method is appropriate to investigate the breakage behaviour of real waste particles. Measuring the breakage probability by this method, the effect of different machine and stress types, and the operating parameters on the particles' breakage behaviour can be investigated. The obtained results can also be used both in shredders' operation and design. For RMSW processing low-speed rotary shredders are typically used for pre-shredding and radial gap shears are used for the comminution of the separated RDF (refuse derived fuel).

EoL Rubber tyres: the EoL (End of Life) tyres can be comminuted in multiple stages. Sometimes the two main steel cords are removed first with a machine, where a hook tears them out through a hole of an armour. Axial gap shears, then radial gap shears and finally cutting mills can be applied when metals are removed. The comminution itself of **EoL batteries** is not problematic, hammer shredders are generally applied. However, the other circumstances, namely the fire and explosion hazard and the hazardous dust emission of dry technologies are the challenge. **EoL refrigerators** can be comminuted by hammer shredders. Many times, one or more considerable mass chains serve as hammers. The first some units, including the first comminution stage of EoL refrigerator recycling plants are working in neutral nitrogen atmosphere which collects the released gases, typically the Freon. The working gas then cleaned and regenerated. **EoL Vehicles**, not only cars, but buses, trains, trucks and ships represent a huge material source after their normal life cycle. The typical first comminution stage of EoL vehicles processing is the pre-shredding with high mass swinging hammer shredders. **Waste electrical and electronic equipment (WEEE), EoL TV devices, EoL Computers** represent source for precious metals and structural materials. Main comminution machines used for WEEE shredding are the hammer shredders and hammer crushers. **Recycling of used printed circuit boards (PCB)** is a widely investigated area; many technological options are available (Abbadi et. al. 2024). For waste PCB comminution – among others – high-speed hammer mills, swing-hammer mills, impact crushers and cutting mills can be applied.

3. STOCK TYPES OF SECONDARY RAW MATERIALS

In a recent paper Mirletz et.al. (2023) projected the cumulative mass of different waste streams, namely many of the stock types of anthropogenic secondary raw materials are listed. According to this projection 70350 mill. tons of municipal solid wastes, 45500 mill. tons of coal ash, 12355 mill. tons of plastic waste, 1876 mill. tons of E-waste, 249 mill. tons of oily sludge and about 120 mill. tons of solar panels will be deposited somewhere by 2050. If we take into account the mineral deposits, namely gangue and tailing stockpiles and tailing ponds and the entire built infrastructure (buildings, roads) we can feel the huge amount of stocked anthropogenic materials. According to our vision there is no waste, just secondary raw materials; so the possibilities of urban mining are really promising.

4. CONCLUSION

This review paper gives only a brief glimpse into the findings of our literature survey. However, we believe that our systematic approach enhances comprehension, clarifies scientific vocabulary and provides insight into the potential urban mining applications of mineral processing. Additionally, a comprehensive overview and categorization of flow and stock types of anthropogenic secondary raw material sources are provided.

ACKNOWLEDGMENTS

This project is funded by the European Union's Horizon Europe program CiRCLE-TECH under grant no. 101079354.

REFERENCES

Abbadi A., Rácz Á., Bokányi Lj. (2024). Exploring the comminution process of waste printed circuit boards in recycling: a review. *Journal of Material Cycles and Waste Management*, 26, 3, pp. 1326–1348. DOI: 10.1007/s10163-024-01945-3

Achtemichuk S., Hubbard J., Sluce R., Shehata M. (2009). The utilization of recycled concrete aggregate to produce controlled low-strength materials without using Portland cement. *Cement and Concrete Composites*, Vol. 31 (8). pp. 564–569. DOI: 10.1016/j.cemconcomp.2008.12.011

Alwaeli M., Mannheim V. (2022). Investigation into the Current State of Nuclear Energy and Nuclear Waste Management – A State-of-the-Art Review. *Energies*, 15 (12) p. 4275. DOI: 10.3390/en15124275

Ambros W. M. (2023) Gravity Concentration in Urban Mining Applications – A Review. *Recycling*, Vol. 8. No. 85. DOI: 10.3390/recycling8060085

Asokan P., Saxena M., Asolekar S. R. (2005). Coal combustion residues – environmental implications and recycling potentials. *Resources, Conservation and Recycling*, Vol. 43, Issue 3, pp. 239–262. DOI: 10.1016/j.resconrec.2004.06.003

Coppola D., Lauritano C., Palma Esposito F., Riccio G. Rizzo C., de Pascale D. (2021). Fish Waste: From Problem to Valuable Resource. *Marine Drugs*, Vol. 19.116. pp. 1–39. DOI: 10.3390/md19020116

Cossu R., Williams I. D. (2015). Urban mining: Concepts, terminology, challenges. *Waste Management*, Vol. 45, 1–3. DOI: 10.1016/j.wasman.2015.09.040.

Cristelo N., Segadães L., Coelho J., Chaves B., Sousa N.R., de Lurdes Lopes M. (2020). Recycling municipal solid waste incineration slag and fly ash as precursors in low-range alkaline cements. *Waste Management*, Vol. 104. pp. 60–73. DOI: 10.1016/j.wasman.2020.01.013

Gupta J., Kumari M., Mishra A., Akram S.M., Thakur I.S. (2022). Agro-forestry waste management – A review. *Chemosphere*, Volume 287, Part 3. DOI: 10.1016/j.chemosphere.2021.132321

Eisenlauer M., Teipel U. (2020). Comminution of Wood – Influence of Process Parameters. *Chemical Engineering & Technology*, Vol. 43, Issue 5. pp. 838–847. DOI: 10.1002/ceat.201900488

Höffken J., Ramana M.V. (2024). Nuclear power and environmental injustice. *WIREs Energy and Environment*, 13 (1), e498. DOI: 10.1002/wene.498

Jeswiet J., Szekeres A. (2016). Energy Consumption in Mining Comminution. *Procedia CIRP 48*, pp. 140–145. DOI: 10.1016/j.procir.2016.03.250

Kamino G., Gomes S., Bragança L. (2019). Improving the sustainability assessment method SBTool Urban – A critical review of construction and demolition waste (CDW) indicator. *IOP Conf. Ser.: Earth Environ. Sci.*, 225 012004.

Khandani F. S., Atapour H., Rad M. Y, Khosh B. (2023). An experimental study on the mechanical properties of underground mining backfill materials obtained from recycling of construction and demolition waste. *Case Studies in Construction Materials*, Vol. 18. e02046. DOI: 10.1016/j.cscm.2023.e02046

Klaffenbach E., Montenegro V., Guo M., Blanpain B. (2023). Sustainable and Comprehensive Utilization of Copper Slag: A Review and Critical Analysis. *Journal of Sustainable Metallurgy*, Vol. 9. pp. 468–496. DOI: 10.1007/s40831-023-00683-4

Komor A., Bujanowitz-Haras B. (2019). Waste from the agricultural sector in the European Union countries in the context of the bioeconomy development. *AGRONOMY SCIENCE wcześniej – formerly Annales UMCS sectio E Agricultura*, Vol. LXXIV (4) pp. 47–59. DOI: 10.24326/as.2019.4.3

Lunardi M. M., Alvarez-Gaitan J. P., Bilbao J. I., Corkish R. (2017). A Review of Recycling Processes for Photovoltaic Modules. *InTechOpen*. DOI: 10.5772/intechopen.74390

Matinde E., Simate G. S., Ndlovu I. S. (2018). Mining and metallurgical wastes: a review of recycling and re-use practices. *J. S. Afr. Inst. Min. Metall.*, Vol. 118. No. 8. DOI: 10.17159/2411-9717/2018/v118n8a5

McNeil K., Kang T. H. K. (2013). Recycled Concrete Aggregates: A Review. *International Journal of Concrete Structures and Materials*, Vol. 7. No. 1. pp. 61–69. DOI: 10.1007/s40069-013-0032-5

Metin Can N., Mercan O. (2023). Evaluation of a capacity increase in AG milling of copper slag. *Physicochem. Probl. Miner. Process.*, Vol. 59 (6). No. 175181. DOI: 10.37190/ppmp/175181

Mirletz H., Hieslmair H., Ovaitt S. (2023). Unfounded concerns about photovoltaic module toxicity and waste are slowing decarbonization. *Nat. Phys.*, Vol. 19, pp. 1376–1378. DOI: 10.1038/s41567-023-02230-0

Mucsi G. (2016). Mechanical activation of power station fly ash by grinding – A review. *Journal of Silicate Based and Composite Materials*, Vol. 68. No. 2. pp. 56–61. DOI: 10.14382/epitoanyag-jsbcm.2016.10

Mucsi G., Szabó R., Rácz Á. Kristály F., Kumar S., (2019). Combined utilization of red mud and mechanically activated fly ash in geopolymers. *Rudarsko Geolosko Naftni Zbornik - Mining Gelological Petroleum Engineering Bulletin*, 34 (1). pp. 27–36. DOI: 10.17794/rgn.2019.1.3

Ongondo F. O., Williams I. D., Whitlock G. (2015). Distinct Urban Mines: Exploiting secondary resources in unique anthropogenic spaces. *Waste Management*, Vol. 45. pp. 4–9. DOI: 10.1016/j.wasman.2015.05.026

Rácz Á., Csőke B. (2021). Comminution of single real waste particles in a swing-hammer shredder and axial gap rotary shear. *Powder Technology*, Vol. 390. pp. 182–189. DOI: 10.1016/j.powtec.2021.05.064

Sander S., Schubert G., Jäckel H.G. (2004). The fundamentals of the comminution of metals in shredders of the swing-hammer type. *International Journal of Mineral Processing*, Vol. 74S. pp. 385–393. DOI: 10.1016/j.minpro.2004.07.038

Santos R.P., Tubino R. (2021). Potential evaluation of the use of construction and demolition waste (CDW) in the recovery of degraded soils by mining in Brazil. *Resources, Conservation & Recycling Advances*, Vol. 12. 200060. DOI: 10.1016/j.rcradv.2021.200060

Schubert G. (1991). Aufbereitung der NE-Metallschrotte und NE-metallhaltigen Abfälle - Teil 1. *Aufbereitungs-Technik 32*k, Nr. 2, pp. 78–89.

Schubert G., Bernotat. (2004). Comminution of non-brittle materials. *International Journal of Mineral Processing*, Vol. 74S. pp. 19–30. DOI: 10.1016/j.minpro. 2004.08.004

Setiadji B. H., Wibowo M. A., Jonkers H. M., Ottele M., Widayat, Qomaruddin M., Sugianto F. H., Purwanto, Lie H. A. (2022). Pyrolysis of Reclaimed Asphalt Aggregates in Mortar. *International Journal of Technology*, Vol. 13 (4), pp. 751–763. DOI: 10.14716/ijtech.v13i4.5621

Tazi N., Kim J., Bouzidi Y., Chatelet E., Liu G. (2019). Waste and material flow analysis in the end-of-life wind energy system. *Resources, Conservation and Recycling*, Vol. 145. pp. 199–207. DOI: 10.1016/j.resconrec.2019.02.039

Tian H., Guo Z., Pan J., Zhu D., Yang C., Xue Y, Li S., Wang D. (2021). Comprehensive review on metallurgical recycling and cleaning of copper slag. *Resources, Conservation and Recycling*, Vol. 168. No. 105366. DOI: 10.1016/j.resconrec.2020.105366

Woldt D., Schubert G. Jäckel H.G. (2004). Size reduction by means of low-speed rotary shears. *International Journal of Mineral Processing*, Vol. 74S, pp. 405–415. DOI: 10.1016/j.minpro.2004.07.008

Winterstetter A., Laner D., Rechberger H., Fellner J. (2016). Integrating anthropogenic material stocks and flows into UNFC-2009 – Challenges and potentials. 7th session, UNECE Expert Group on Resource Classification, Geneva, 26–29 April 2016.

Yakovleva E., Titova E. (2021). Recycling of forestry waste. *Forestry-2021, IOP Conf. Series: Earth and Environmental Science 875,* IOP Publishing. pp. 1–9. DOI: 10.1088/1755-1315/875/1/012045

Yang L., Xu X., Ke G. (2021). Agricultural Waste Recycling Optimization of Family Farms Based on Environmental Management Accounting in Rural China. *Sustainability 13*, No. 10. p. 5515. DOI: 10.3390/su13105515

Geosciences and Engineering, Vol. 13, No. 1 (2025), pp. 88–96.
https://doi.org/10.33030/geosciences.2025.01.007

CO_2 SEQUESTRATION EXPERIMENTS BY PRODUCING GEOPOLYMER SPECIMENS FROM LIGNITE FLY ASH

TAMÁS KURUSTA[1*], KITTI PATRÍCIA KLAJ[2], TEEMU KINNARINEN[3], NAZILA BOLOURIEH[4], GÁBOR MUCSI[5]

[1, *] *Faculty of Earth and Environmental Sciences and Engineering, University of Miskolc, Hungary; tamas.kurusta@uni-miskolc.hu*
[2] *Faculty of Earth and Environmental Sciences and Engineering, University of Miskolc, Hungrary; kittiklaj@gmail.com*
[3] *LUT School of Engineering Sciences, Lappeenranta-Lahti University of Technology LUT, Lappeenranta, Finland; teemu.kinnarinen@lut.fi*
[4] *LUT School of Engineering Sciences, Lappeenranta-Lahti University of Technology LUT, Lappeenranta, Finland; nazila.bolourieh@lut.fi*
[5] *Faculty of Earth and Environmental Sciences and Engineering, University of Miskolc, Hungary; gabor.mucsi@uni-miskolc.hu*
[1] *https://orcid.org/0009-0009-2979-1647*
[5] *https://orcid.org/0000-0003-1031-2801*

Abstract: The mineral-based sequestration of CO_2 offers a permanent and safe method to store CO_2 captured from flue gas. In this process, CO_2 reacts with calcium and/or magnesium-bearing materials to form stable, environmentally benign carbonate minerals. In a recent research project, CO_2 sequestration was performed on deposited fly ash from Visonta, Northern Hungary, coupled with mechanical activation. The resultant carbonate phases were analyzed for their suitability as geopolymer-based construction materials. CO_2 sequestration and mechanical activation occurred in a Fritsch Pulverisette 5 planetary ball mill under wet conditions. The samples were dried post-sequestration, and 20 × 20 × 20 mm geopolymer specimens were prepared and tested for compressive strength after seven days. It was found that bassanite, the primary calcium source in fly ash, reacts with CO_2 only in the presence of NaOH. Additionally, low NaOH concentrations (0.5 M) during grinding positively impacted the compressive strength of the geopolymer, while higher concentrations reduced it. At 2 M NaOH, the specimen failed to set fully, deforming plastically under pressure. The experiment yielded a maximum compressive strength of 16.1 MPa for the geopolymer using 0.5 M NaOH.

Keywords: *CO_2 sequestration, fly ash, mechanical activation, geopolymer*

1. INTRODUCTION

Global warming is a critical challenge we face today, primarily driven by the rise in Earth's atmospheric temperature due to increased greenhouse gases. While these gases naturally exist in the atmosphere, anthropogenic greenhouse gases, such as CO_2, have surged, particularly since the Second Industrial Revolution.

One promising approach to mitigate atmospheric CO_2 is mineral sequestration. This process involves reacting CO_2 with non-carbonate minerals that contain alkali

metals (e.g., sodium or potassium) and alkaline earth metals (e.g., calcium or magnesium). The reaction leads to the formation of various carbonate minerals, which can be either anhydrous or contain hydroxide (OH^-) or water (H_2O), such as calcite ($CaCO_3$), magnesite ($MgCO_3$), or siderite (Fe_2CO_3) (Turvey et al., 2018).

For effective CO_2 sequestration, the host material should be rich in non-carbonate calcium and/or magnesium minerals. Based on this requirement, natural silicate minerals with high levels of serpentinite, forsterite, or olivine (Romão, 2014), as well as industrial by-products with similar mineralogical properties, such as construction and demolition waste (Ghacham et al., 2017), red mud (Mucsi et al., 2021), steel slag (Bonenfant et al., 2008), and fly ash (Montes-Hernandez et al., 2009), can be utilized for CO_2 sequestration.

This study focuses on fly ash-based CO_2 sequestration enhanced by mechanical activation. The aim is to capture and permanently sequester CO_2 through mineral carbonation, forming stable compounds. Additionally, we explore the potential of using fly ash with newly formed mineral phases as a geopolymer material for construction. We apply a direct carbonation approach to increase the reactivity of the ash through high-energy milling in a wet medium.

2. Material and Methods

2.1. Material

The experiments were carried out on lignite fly ash from MVM Mátra Energia Ltd., Visonta, Northern Hungary. The analysis of the particle size distribution of the sample reveals that the sample primarily comprises particles below 400 μm, with a 66 μm median particle size. The initial moisture content was found to be 24.1 wt%. The fly ash particle density was 1.92 g/cm^3, and the bulk density was 0.58 g/cm^3. Biogon-C CO_2 gas (95.5% purity) was used for carbonate reactions without further purification.

2.2. Methods

2.2.1. Mechanical activation and CCS

The experiment conducted CO_2 sequestration and mechanical activation simultaneously in a Fritch Pulverisette 5 planetary ball mill under wet conditions, using NaOH solution of varying concentrations (0.1, 0.25, 0.5, 1, and 2 M) as the grinding fluid. The milling was carried out using 500 ml steel jars with a gas valve and steel grinding media. The jars were filled with 54.3 g of dry sample, 162,9 g NaOH solution and 543 g of 20 mm diameter grinding balls. The grinding was carried out at 200 rpm for 180 min, and the free grinding chamber was filled with CO_2 gas at up to 5.5 bar pressure and refilled every 15 min to the initial CO_2 pressure.

2.2.2. Measurement of mineral characteristics

The WD-XRF measurement was performed using RIGAKU Supermini 200 type WDXRF. The radiation source was an air-cooled 200 W palladium (Pd) X-ray tube with an excitation voltage of 50 kV and 4.0 mA. Quantitative analysis requires the

calibration of the standards for the identified elements. Calibration is performed element-by-element, with 8–12 pcs for main elements and 6–10 pcs for trace elements (the number of standards used is not constant, but is determined by the concentration of each component in the standards). Each element is measured seven times (two background points 10-10, peak position 40 sec), thus the errors can be reduced statistically, and the measurement also gives a better average value.

The mineralogy of the fly ash was determined by X-ray powder diffraction (XRD) with a Bruker D8 Advance diffractometer using Cu K-alpha radiation (40 kV, 40 mA) in parallel beam geometry obtained with Göbel mirror, in the 2°–70° (2θ) range with a 0.007° (2θ) step interval and a 24 s step counting time. The crystalline phases were identified by Bruker DiffracPlus software package in its EVA module ICDD PDF-2 (2005) database for search/matching of phases. The quantitative evaluation was carried out by Rietveld refinement in the TOPAS4 software, where the amorphous content was determined by the amorphous hump method.

The stretching and bending vibrations of the chemical bonds in the samples before and after CO_2 sequestration were detected by a JASCO FT-IR 4200 type Fourier Transformed Infrared Spectrometer in reflection mode with a diamond ATR. The infrared transmission spectra of the samples were recorded between 400 and 4000 cm^{-1} with a resolution of 4 cm^{-1}. The observed spectra are plotted as a function of wavenumber and transmittance. Observed FTIR bands were interpreted based on the handbook by Chukanov and Chervonny (2014).

The Controls C250Kn uniaxial compression machine was used to measure the compressive strength of the prepared specimens. The test involved placing the specimens between parallel steel plates and subjecting them to axial compression up to the breaking load, with a load increment of 300 N/min.

3. RESULTS

3.1. Chemical and mineral properties of fly ash

According to the XRF measurement (Table 1) the major component of the fly ash is CaO, proving it a suitable material for CCS. The sample contains a total of 15.51 wt% of CaO and MgO, which is relatively low for CO_2 sequestration. The utilization of CO_2-treated fly ash will play an important role.

Table 1

Oxidic components of fly ash (weight percent, error +/– 0.01 relative percent, LOI 0,05 wt%

Al_2O_3	Fe_2O_3	SiO_2	TiO_2	Na_2O	MgO	CaO	P_2O_5	K_2O	MnO	S	F
14	11.2	39.8	0.50	0.54	3.41	12.1	0.35	1.61	0.18	6.5	<0.3

Table 2 shows the mineral composition of fly ash. Among the minerals present in the sample, bassanite, bytownite, and magnesioferrite can react with CO_2. Considering the amount of crystalline calcium and magnesium phases, the amorphous phase also contains 3-3 wt% of calcium and magnesium. Portlandite, lime, brucite, and

periclase are the mineral phases typically found in typical fly ashes (Monasterio et al., 2020), and they possess good CO_2 sequestration capacity. However, these minerals are not present in the Visonta lignite fly ash.

Table 2

Mineral components of fly ash (weight percent, error +/– 0.01 relative percent)

Mineral phase	Formula	Weight percent
Calcite	$CaCO_3$	6.2
Quartz	SiO_2	17.6
Bassanite	$Ca[SO_4]\cdot 0{,}5\ H_2O$	9.5
Hematite	$Fe^{3+}{}_2O_3$	4.1
Maghemite	$Fe^{3+}{}_2O_3$	4.9
Bytownite	$Na_{0.2}Ca_{0.8}Al_{1.8}Si_{2.2}O_8$	6.7
Galenite	PbS	3.9
Albite	$NaAlSi_3O_8$	7.6
Mg-Ferrite	$MgFe_2O_4$	1.9
Amorf	–	38

3.2. Change of dispersity

Figure 1 shows the changes in dispersion occurring during grinding. After the grinding in NaOH solution, the samples have almost the same geometric surface area (2,5–3 m^2/g), with a slight increase in coarsening from 3.43 µm to 4.79 µm for the d_{50} particle size with increasing NaOH concentration. A significant difference is observed in the measurement in deionized water, where an increase in the proportion of fine grains is observed, resulting in a decrease in the median grain size from ~3-4 µm to ~0.57 µm compared to the other measurements.

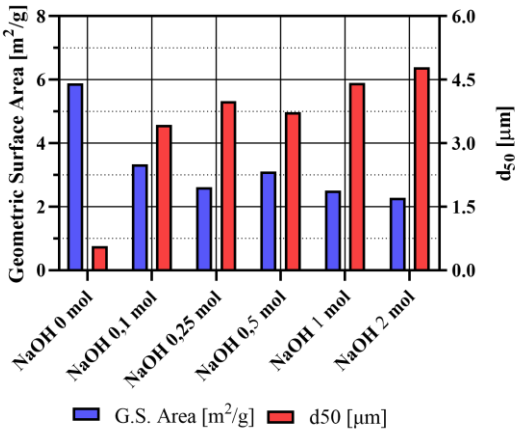

Figure 1

Changes in geometric specific surface area and particle size d_{50}

Fly ash treated with CO_2 was used to create geopolymer specimens in the size of 20 × 20 × 20 mm. To achieve the ideal Al_2O_3/Na_2O ratio of 1, various concentrations of NaOH were used as an activating solution. The mixtures were prepared with a liquid-to-solid ratio of 1, with half of the liquid being Betol93 sodium silicate. The oxide composition and mixing ratios of grounded fly ash are shown in Table 3.

The geopolymer poured into the mold was stored at ambient temperature in an isolated from air for 24 hours, followed by heat treatment at 60 °C for 6 hours.

Table 3

Oxide components of grounded fly ash and their mixing ratios

Oxidic components [w%]	Raw	0.1	0.25	5	1	2
Al_2O_3	15.14	16.07	16.24	15.62	14.27	13.11
Fe_2O_3	10.32	11.7	11.5	11.2	10.7	10.0
SiO_2	45.9	50.0	50.3	49.3	45.1	42.3
TiO_2	0.564	0.556	0.549	0.534	0.507	0.492
Na_2O	0.51	1.02	1.48	2.64	4.99	7.42
MgO	2.81	2.78	2.78	2.78	2.52	2.23
CaO	11.42	8.98	9.11	9.00	8.52	8.10
P_2O_5	0.282	0.250	0.257	0.248	0.233	0.217
K_2O	1.64	1.56	1.56	1.55	1.48	1.39
MnO	0.139	0.157	0.156	0.150	0.145	0.139
SO3	11.0	1.95	1.24	1.29	1.31	1.07
	Mixture data					
Concentration of NaOH solution [M]	10	10	10	8	5	3
Total Na_2O [g]	4.60	4.76	4.89	4.57	4.09	3.89
Al_2O_3 [g]	4.54	4.82	4.87	4.69	4.28	3.93
SiO_2 [g]	13.77	15.00	15.09	14.79	13.53	12.69
Al_2O_3/Na_2O	0.99	1.01	1.00	1.03	1.05	1.01
SiO_2/Na_2O	2.99	3.15	3.08	3.24	3.31	3.26
l [g]	30.0	30.0	30.0	30.0	30.0	30.0
s [g]	30.0	30.0	30.0	30.0	30.0	30.0
l/s ratio	1	1	1	1	1	1

3.3. Structural changes during carbonation and geopolymerization

In Figure 2, the spectral images of FTIR measurements on CO2-treated samples can be seen. Measurements on dried samples were carried out one day after milling. After CO_2 sequestration, significant differences can be observed in the -C = O peaks at

1460 cm^{-1} and the C-O peaks at 880 cm^{-1} for calcite. Both peaks increase with NaOH concentration up to a concentration of 1 M and then remain constant. A slight change is observed in the Al-O-Si peak at 1010 cm^{-1}, which decreases slightly in intensity and shifts towards 980 cm^{-1}, indicating that geopolymerization has already started during grinding.

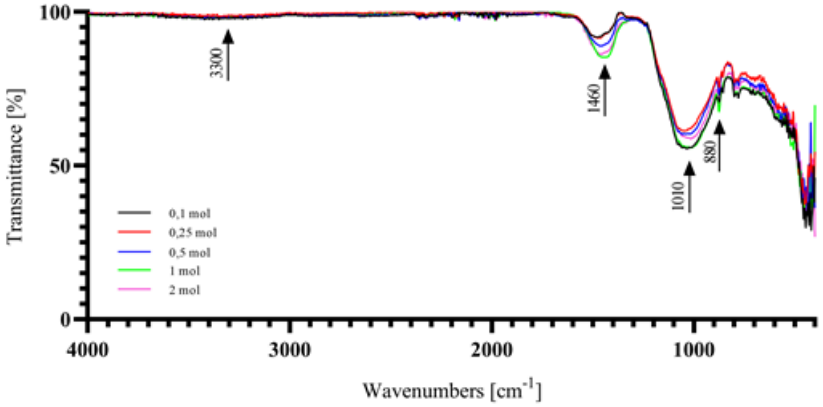

Figure 2
FTIR spectrum of the CO2-treated sample

The mineral composition after milling and CO_2 sequestration is shown in Table 4. Among the three crystalline phases in the fly ash capable of binding carbonates, bassanite and magnesioferrite fully reacted during the process, while the mass fraction of bytownite was reduced by half. From the reacted phases, two types of carbonate minerals were formed: calcite and thermonatrite. However, only calcite is suitable for long-term CO_2 storage. By the end of the process, the sample contained 14.2 wt% calcite, representing an increase of 8.3 wt% compared to the initial state. The remaining bytownite in the sample, if fully reacted, could result in an additional ~1% improvement. Therefore, the amorphous material in the fly ash must still contain a significant Ca source.

Table 4
Mineral components of CO_2 treated (2M) fly ash

Mineral phase	Formula	Volume percent
Calcite	$CaCO_3$	14.23
Quartz	SiO_2	8.47
Bassanite	$Ca[SO_4]\cdot 0{,}5\ H_2O$	0.00
Hematite	$Fe^{3+}{}_2O_3$	7.98
Maghemite	$Fe^{3+}{}_2O_3$	6.00
Bytownite	$Na_{0.2}Ca_{0.8}Al_{1.8}Si_{2.2}O_8$	4.26
Galenite	PbS	1.24

Mineral phase	Formula	Volume percent
Albite	$NaAlSi_3O_8$	5.65
Mg-Ferrite	$MgFe_2O_4$	0.00
Thermonatritis	$Na_2(CO_3)•(H_2O)$	1.27
Anhydrite	$CaSO_4$	0.16
Amorf	–	50.20

The FTIR spectra show the changes in band intensities that reflect the effects of with NaOH concentration on the geopolymerization process (Figure 3). The FTIR data reveals that up to 0.5 M NaOH, there is a slight decrease in peak intensities, while at 1 M and 2 M NaOH, a significant decrease is observed. The most prominent changes are in the OH-HOH bond (3300 cm^{-1}) and the bound water peak (1645 cm^{-1}), as well as in the silicate band around 980 cm^{-1}, which is a critical indicator of geopolymerization. The relative increase in the silicate band intensity suggests a higher degree of polymerization (Rattanasak and Chindaprasirt, 2009), although this observation does not align with the strength study results. This inconsistency indicates the possible formation of clay-like hydrosilicates in a non-bonded state. Furthermore, the -C = O peak at 1390 cm^{-1} and the C-O peak at 880 cm^{-1} show relative decreases, pointing to carbonate reactions occurring in parallel with polymerization.

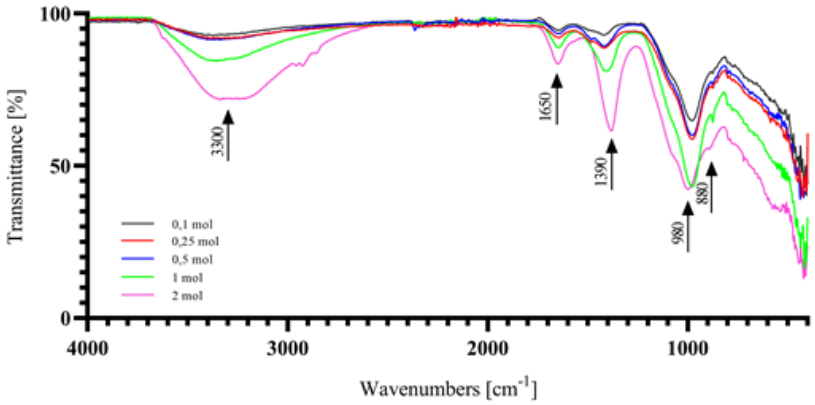

Figure 3

FTIR spectrum of the geopolymer samples

3.4. Result of the axial load test

The compressive strength of the geopolymer specimens (Figure 4) improved as the concentration of the added NaOH solution during grinding increased up to 0.5 M. The compressive strength of the specimens increased from 9.5 MPa to 16.1 MPa. However, a significant loss of strength was observed when the NaOH concentration was further increased to 1 and 2 M. At a concentration of 1 M, the strength of the specimens was

only 5.68 MPa, which is approx. 60% of the reference sample. At 2 M, the specimen did not fully solidify, leading to plastic deformation during measurement.

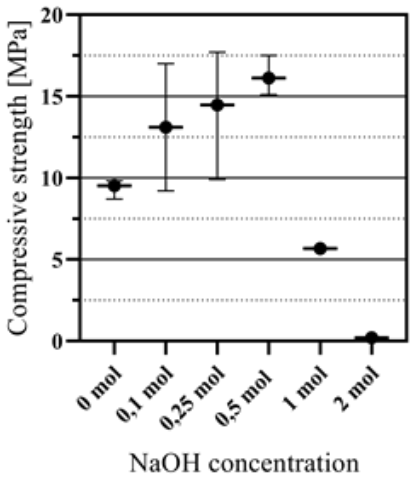

Figure 4
Compressive strength of the test specimens

4. CONCLUSIONS

By increasing the concentration of added NaOH, we can enhance the CO_2 absorption capacity of the sample material. This can be explained by the fact that the primary source of Ca in the fly ash, bassanite, decomposes into sodium sulphate, calcium hydroxide, and water after reacting with NaOH. Only then it can react with CO_2 in the system. Furthermore, adding low concentrations of NaOH (up to 0.5 M) during grinding positively affects the compressive strength of the specimens. Geopolymers prepared this way achieve 40.1% higher strength than specimens subjected only to mechanical activation. This is presumably due to the strength-increasing effect of the resulting microcrystalline calcite (Kamal et al., 2020). However, it is observed that high NaOH concentration (1, 2 M) added during grinding already causes strength loss. At 2 M solution, the specimens still need to be fully solidified. The sample prepared in 0.5 M NaOH meets the 7-day strength requirement for 32.5 strength class standard batch cements. In the next phase of the research, we will extend the strength testing to 2 and 28 days and investigate the role of different bonds (carbonate and geopolymeric bonds) in the setting process.

ACKNOWLEDGMENTS

The authors wish to acknowledge support from the Research Hub on Sustainable Circular Economy, CiRCLETECH Hub project (101079354) funded by the European Commission through the Horizon Europe programme.

REFERENCES

Bonenfant, D., Kharoune, L., Sauve, S., Hausler, R., Niquette, P., Mimeault, M., Kharoune, M. (2008). CO_2 sequestration potential of steel slags at ambient pressure and temperature. *Industrial & Engineering Chemistry Research*, 47 (20), pp. 7610–7616. https://doi.org/10.1021/ie701721j

Chukanov, V. N., Chervonnyi, D. A. (2014). *Infrared Spectroscopy of Minerals and Related Compounds*. Springer.

Ghacham, A. B., Pasquier, L., Cecchi, E., Blais, J., Mercier, G. (2017). Valorization of waste concrete through CO_2 mineral carbonation: Optimizing parameters and improving reactivity using concrete separation. *Journal of Cleaner Production*, 166, pp. 869–878. https://doi.org/10.1016/j.jclepro.2017.08.015

Kamal, N. L, Itam Z., Sivaganese Y., Beddu S. (2020). Carbon dioxide sequestration in concrete and its effects on concrete compressive strength. *Materials Today: Proceedings*, 31 (1), A18–A21. https://doi.org/10.1016/j.matpr.2020.11.185

Monasterio-Guillot, L., Alvarez-Lloret, P., Ibañez-Velasco, A., Fernandez-Martinez, A., Ruiz-Agudo, E., Rodriguez-Navarro, C. (2020). CO_2 sequestration and simultaneous zeolite production by carbonation of coal fly ash: Impact on the trapping of toxic element. *Journal of CO_2 Utilization*, 40, p. 101263. https://doi.org/10.1016/j.jcou.2020.101263

Montes-Hernandez, G., Pérez-López, R., Renard, F., Nieto, M., Charlet, L. (2009). Mineral sequestration of CO_2 by aqueous carbonation of coal combustion fly-ash. *Journal of Hazardous Materials*, 161 (2–3), pp. 1347–1354. https://doi.org/10.1016/j.jhazmat.2008.04.104

Mucsi, G., Halyag, N., Kurusta, T., Kristály, F. (2021). Control of Carbon Dioxide Sequestration by Mechanical Activation of Red Mud. *Waste and Biomass Valorization*, 12, pp. 6481–6495. https://doi.org/10.1007/s12649-021-01466-2

Rattanasak, U., Chindaprasirt, P. (2009). Influence of NaOH solution on the synthesis of fly ash geopolymer. *Minerals Engineering*, 22 (12), pp. 1073–1078. https://doi.org/10.1016/j.mineng.2009.03.022

Romão, I., Slotte, M., Gando-Ferreira, L. M., Zevenhoven, R. (2014). CO_2 sequestration with magnesium silicates—Exergetic performance assessment. *Chemical Engineering Research and Design*, 92 (12), pp. 3072–3082. https://doi.org/10.1016/j.cherd.2014.05.016

Turvey, C. C., Wilson, S. A., Hamilton, J. L., Tait, A. W., McCutcheon, J., Beinlich, A., Fallon, S. J., Dipple, G. M., Southam, G. (2018). Hydrotalcites and hydrated Mg-carbonates as carbon sinks in serpentinite mineral wastes from the Woodsreef chrysotile mine, New South Wales, Australia: Controls on carbonate mineralogy and efficiency of CO_2 air capture in mine tailings. *International Journal of Greenhouse Gas Control*, 79, pp. 38–60. https://doi.org/10.1016/j.ijggc.2018.09.015

Geosciences and Engineering, Vol. 13, No. 1 (2025), pp. 97–108.
https://doi.org/10.33030/geosciences.2025.01.008

TREATMENT OF ACID MINE DRAINAGE VIA ADSORPTION WITH FOOD WASTE ACTIVATED CARBONS

JOHN KWAME BEDIAKO[1, *], EMESE SEBE[2], BRIGHTON EMMANUEL MABURUTSE[3], EVELIINA REPO[4]

[1, *]*Department of Separation Science, School of Engineering Science, LUT University, Finland; john.bediako@lut.fi*

[2]*Institute of Energy, Ceramics and Polymer Technology, University of Miskolc, Hungary, emese.sebe@uni-miskolc.hu*

[3]*Department of Animal Production Sciences, Marondera University of Agricultural Sciences and Technology, Zimbabwe, maburutseb@gmail.com*

[4]*Department of Separation Science, School of Engineering Science, LUT University, Finland; eveliina.repo@lut.fi*

[1]*https://orcid.org/0000-0003-1816-4890*
[2]*https://orcid.org/0000-0003-4797-4024*
[3]*https://orcid.org/0000-0001-5957-3514*
[4]*https://orcid.org/0000-0002-6006-3631*

Abstract: This study addresses the challenges of acid mine drainages (AMDs) treatment by exploring food waste-derived activated carbons (ACs). The study involves a synthesis of ACs from fruit peels and evaluation for removing heavy metals in AMDs. The AMD solutions were simulated and experiments were conducted via batch adsorption. All the ACs exhibited high adsorption affinities for Pb(II) in the order of KOH-AC > NaOH-AC > H_3PO_4-AC > H_2SO_4-AC > $ZnCl_2$-AC, however, the overall best adsorption capacities were recorded by KOH-AC, NaOH-AC and $ZnCl_2$-AC, with estimated equilibrium uptakes of 526.31 ±50.52, 26.14 ±0.23, 426.62 ±20.68, 164.24 ±11.54, 129.95 ±6.31 and 141.75 ±26.01 mg/g, for Hg(II), As(IV), Pb(II), Cd(II), Cu(II) and Co(II), respectively. The adsorption kinetics was faster for the smaller size metals than the larger ones. The study highlights the potential of these ACs as sustainable and effective adsorbents for mitigating the impact of mining activities on water quality. The findings may contribute valuably to the field of environmental remediation and sustainable mining.

Keywords*: acid mine drainage, activated carbon, adsorption, heavy metal, wastewater treatment*

1. INTRODUCTION

Toxic heavy metal pollution from the mining and hi-tech industries is among several environmental problems facing the world today (Akcil and Koldas, 2006; Acheampong, 2013; Bediako et al., 2017). Mining contributes immensely to the economy of many countries across the globe; however, mining activities also lead to the generation of acid mine drainage (AMD), which is always laden with numerous toxic heavy metals, such as As, Hg, Pb, Cd, Cu, Co, Ni, Cr, Al, Fe, etc. (Akcil and Koldas, 2006; Oyewo et al., 2018). Having been recognized as one of the most severe environmental problems in the

mining industry, the causes, predictions, and treatments of AMD have become the focus of many research initiatives commissioned by governments, the mining industry, universities, and research establishments, with additional input from the general public and environmental groups (Akcil and Koldas, 2006).

In many mineral-rich developing countries, the mining activities, most of which are illegally operated, have contaminated the surrounding environments and water bodies. A typical example is the case of "galamsey", also known as "gather and sell" in Ghana, which is currently causing an existential threat to human lives, as well as the fauna and flora, due to the mass pollution of major water bodies and agricultural farmlands. These issues are seen to emanate from either outright neglect of safety and mine wastewater treatment protocols or direct ejection of the toxic metal-bearing wastewaters into the surrounding environments without prior proper treatments (Acheampong, 2013; Bansah et al., 2016). The mining activities of both artisanal and legal miners are reported to endanger the environment through land degradation, deforestation, biodiversity loss, and contamination of surface and groundwater resources. The use of chemicals, commonly heavy metals and cyanide is of major concern. For example, the mercury amalgamation technique of gold extraction, which is largely practiced by small-scale miners in some parts of Africa, is harmful to a wide range of ecological entities (Bansah et al., 2016).

Heavy metal toxicity can cause serious carcinogenic and other adverse health problems even at low concentrations (Bediako et al., 2017). This is because they are easily accumulated by aquatic organisms, which can be passed on to human beings via the food chain; hence they must be properly treated (Li et al., 2015; Oyewo et al., 2018). Due to their severe toxicities and evolving health threats, international and domestic regulatory bodies have been revising and tightening regulations on their handling and treatments before discharge into the aquatic environment (Bediako et al., 2015; Khalil et al., 2013). Despite the strict regulations, some mining entities and illegal operators still manage to flout these directives. For instance, several surveys conducted by the Environmental Protection Agency (EPA) of Ghana showed that not even the major companies adhered to the permissible discharge levels of heavy metal-bearing AMD wastewaters into water bodies (Acheampong, 2013; Ghana EPA, 2010). Lack of adequate human resource capacities to manage wastewater or the absence of low-cost wastewater treatment options are identified as the two main reasons for the non-compliance by the companies (Acheampong, 2013).

The conventional methods of AMD wastewater treatment such as cementation and chemical precipitation techniques are expensive and pose a tendency of secondary pollution through sludge formation. Conversely, adsorption has been identified as one of the best alternative treatment methods owing to its simplicity, low-cost, environmental sustainability, and efficiency for low concentrations up to parts per billion (Bediako et al., 2016; Li et al., 2013). Moreover, there are several classes of adsorbents to choose from, and adsorption using activated carbon (AC) is one of the most widely known options. However, a major issue confronting the patronage of AC is the high costs of commercial products, which are usually sourced from coal, coir, and petroleum residues (Yagsi, 2004; Bediako et al., 2018). Recent studies have suggested the use of food waste-derived ACs as alternatives, which have received

considerable acceptance owing to the ready availability and abundance of food waste precursors, such as fruit peels, shells, nuts, and seeds. Therefore, in this study, fruit peels were used as precursors to synthesize low-cost ACs and to subsequently evaluate their efficiency in heavy metal removal from potential AMDs. The study offers important perspectives for advancing environmental remediation and fostering sustainable mining practices through effective treatment of mining wastewater.

2. MATERIALS AND METHODS

2.1. Chemicals used

Metal complexes including $HNa_2AsO_4.7H_2O$, $Pb(NO_3)_2$, $Cd(NO_3)_2.4H_2O$, $Cu(NO_3)_2.3H_2O$, $Co(NO_3)_2.6H_2O$, and $HgCl_2$, and chemical reagents such as H_2SO_4, KOH, NaOH, H_3PO_4, $ZnCl_2$ and HCl, were procured from Daejung Chemicals and Metals Co., Ltd. and Sigma-Aldrich Ltd. All the chemicals used in this study are of analytical grade and were used as received, without further treatment. Stock solutions (~1000 mg/L) were prepared from the metal complexes and diluted into working solutions of 0–1000 mg/L for the adsorption experiments.

2.2. Activated carbon synthesis method

Dry pulverized orange peels were first pre-carbonized at 400 °C for 1 h. After that, they were soaked in the activation agents, i.e., KOH, NaOH, H_2SO_4, H_3PO_4, and $ZnCl_2$ in 3 : 1 weight ratio for 24 h, followed by activation at 800 °C for 1 h under continuous N_2 purging. In all, five types of activation agent-based ACs were produced. These ACs were washed with distilled water (DW) and dried in an oven kept at 70 °C for 24 h, pending adsorption evaluation. The synthesized ACs were characterized as previously reported and as discussed later (Bediako et al., 2018; Bediako et al., 2020).

2.3. Adsorption studies

The adsorption studies were performed in batch modes using the prepared metal solutions of As(V), Hg(II), Pb(II), Cd(II), Cu(II), and Co(II) as representatives of the heavy metals that usually accompany AMDs. First, each of the five ACs was evaluated against each of the six heavy metal ions. After that, the best AC for each of the metal species was selected to run adsorption isotherm studies at pH 6 with initial concentrations ranging from 0–1000 mg/L. Approximately 10 mg of each AC sample was weighed into a 50 mL falcon tube and 20 mL of each metal solution was added. The mixtures were placed in a multi-shaking incubator whirling at 120 rpm and 25 ±2 °C for 24 h. After equilibrium, the solutions were centrifuged at 12000 rpm for 5 min and diluted for analysis of the residual concentrations of metal ions.

Next, adsorption kinetics were carried out with multi-metal mixtures of all the metal ions. About 300 mL of 100 mg/L metal solutions were filled into glass beakers covered with aluminum foils and placed on multi-purpose magnetic stirrers with stirring bars. AC dozes of 0.1 g were then added to the solutions and timers were set to start counting. Small portions (~ 1 mL) were drawn from the bulk of each solution

at various time intervals for 24 h and then analyzed for residual concentrations. An inductively coupled plasma-atomic emission spectrometer (Thermo Scientific, iCAP 7000 series, ICP Spectrometer, USA) was used for the analyses, and the uptakes were calculated according to the expression:

$$q = \frac{(C_i V_i - C_e V_e)}{M} \quad (1)$$

where C_i and C_e are the initial and equilibrium metal ion concentrations in mg/L, V_i and V_e are the initial and equilibrium volumes in L, and M is the dry weight of ACs in grams.

3. Results and Discussion

3.1. Characterization of the synthesized ACs

The synthesized ACs were examined physically by means of digital camera, as well as using a field emission scanning electron microscope (FE-SEM, SUPRA 40VP), manufactured in Germany by Carl Zeiss. This equipment was integrated with an energy dispersive X-ray spectroscope (EDX) and could provide information on both the surface morphologies and elemental constitution of the ACs. Using the KOH-AC as a representative, Figure 1a presents a digital image of the synthesized ACs, showing clear formation of black granulated substances that are symbolic of typical ACs. The FE-SEM image captured at ×20000 magnification portrays varying porosities of the ACs at an average size of 1 µm (Figure 1b). Consequently, evidence of elements including C, O, Mg, K, and Ca is present in the ACs, according to the EDX spectrum in Figure 1c. As expected, the carbon content is the highest at ~78 wt% and ~87 At% (Figure 1d).

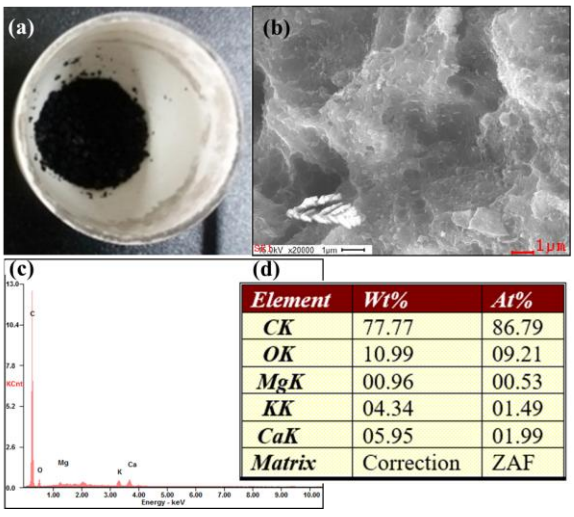

Element	Wt%	At%
CK	77.77	86.79
OK	10.99	09.21
MgK	00.96	00.53
KK	04.34	01.49
CaK	05.95	01.99
Matrix	Correction	ZAF

Figure 1

KOH-AC showing formation of black granules typical of traditional ACs in (a) a digital camera, (b) FE-SEM image showing surface morphology, (c) and (d) EDX results showing elemental spectra and table of element composition, respectively

3.2. Evaluation of heavy metal removal capacities

Initial adsorption tests were conducted to evaluate the adsorption affinity of each of the synthesized ACs towards the heavy metal ions, and to select the best adsorbent for each metal ion. The metal uptakes by the ACs using 100 mg/L initial concentrations of each metal in a multicomponent system are plotted in Figure 2. As can be seen, the adsorption capacities differed according to the types of activation agents used. The As(V) and Co(II) uptakes had been relatively low for all the ACs; however, the $ZnCl_2$-AC and NaOH-AC showed differences by recording significantly high uptakes of 15.30 and 38.58 mg/g, respectively for the aforementioned metals. The best adsorbents for Pb(II) and Hg(II) were identified to be the KOH-AC and $ZnCl_2$-AC, which exhibited uptakes reaching 210.17 and 194.32 mg/g, respectively. The Cd(II) and Cu(II) appeared to be best adsorbed by the H_3PO_4-AC, which recorded uptakes of 151.37 and 161.96 mg/g, respectively; however, careful observations of the supernatants revealed that large amounts of precipitations had occurred. For this reason, the next best adsorbent, i.e., NaOH-AC was considered for the subsequent adsorption tests for these two metals. Overall, all the ACs showed high adsorption capacities of Pb(II) due to its large size since the uptake was calculated on a milligram per gram basis. A summary of the selected best ACs and their respective heavy metal uptakes are given in Table 1.

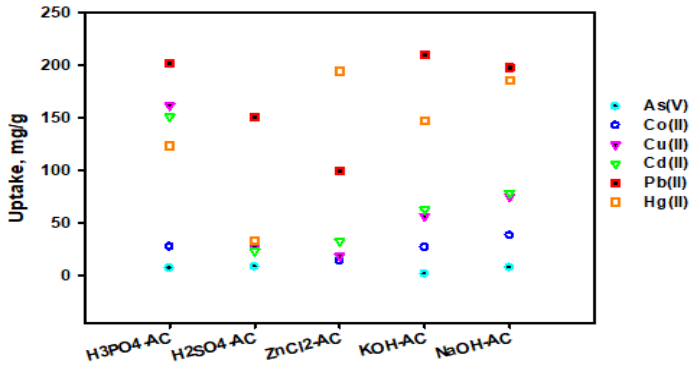

Figure 2

Activation agent-based carbons and their heavy metal uptakes. Experimental conditions: 10 mg AC in 20 mL of 100 mg/L multi-metal solution at pH 6, 120 rpm, and 25±2 °C for 24 h

Table 1

Summary of best AC adsorbents for the representative heavy metals

Adsorbent	Metal specie	Uptake (mg/g)
$ZnCl_2$-AC	As(V)	15.30
NaOH-AC	Co(II)	38.58
NaOH-AC	Cu(II)	75.49
NaOH-AC	Cd(II)	78.65
KOH-AC	Pb(II)	210.17
$ZnCl_2$-AC	Hg(II)	194.32

3.3. Adsorption isotherm evaluation

Following Table 1, adsorption isotherm studies were performed using the selected best ACs for each of the respective target heavy metals. The isotherm experiments were carried out to obtain the maximum equilibrium uptake of each metal by the ACs. It could be observed from Figure 3 that all the uptakes followed the usual adsorption phenomenon where the adsorption capacity increases but removal efficiency decreases comparatively with increasing initial concentrations (Abudaia et al., 2013; Bediako et al., 2016). In other words, the isotherm data points rose steadily and reached near plateau-like shapes at equilibrium. Each data was fitted with the two most utilized isotherm models; the Langmuir and Freundlich models, to estimate the maximum equilibrium uptakes and intensities of interactions. These models are presented in the following equations:

I) Langmuir model:

$$q_e = q_m \frac{bC_e}{1+bC_e} \tag{2}$$

II) Freundlich model:

$$q_e = KC_e{}^{1/n} \tag{3}$$

where q_m is the maximum equilibrium uptake given in mg/g, b is the coefficient concerning the affinity between the ACs and heavy metal ions, q_e is the equilibrium uptake (mg/g) at any time, C_e is the equilibrium metal ion concentration (mg/L), K and n are the Freundlich constants depicting the relative adsorption capacity and adsorption intensity, respectively.

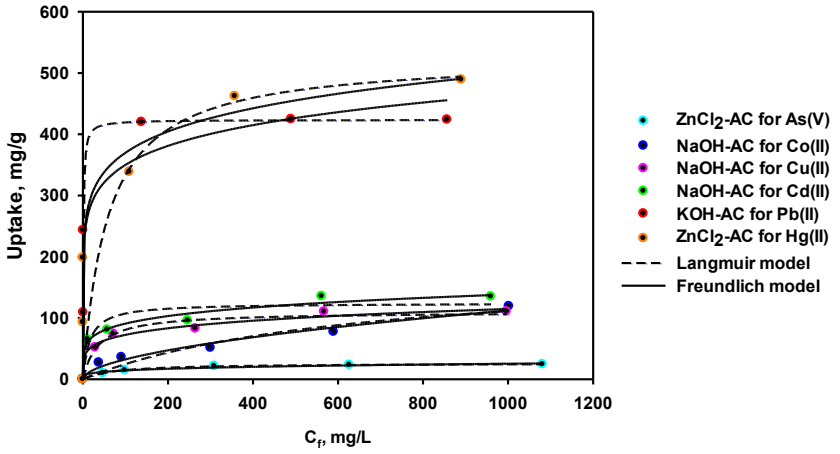

Figure 3

Isotherms of heavy metal adsorption based on the best suitable AC for each target metal. Experimental conditions: 10 mg AC in 20 mL of 0 – 1000 mg/L metal solutions at pH 6, 120 rpm, and 25±2 °C for 24 h

The Langmuir model provided better fits to the isotherm data with high values of determination coefficient (R^2) than the Freundlich model (Tables 2 and 3). Moreover, the Langmuir model's predicted order of maximum equilibrium uptakes was consistent with that from the experiments. The order was $ZnCl_2$-AC-Hg > KOH-AC-Pb > NaOH-AC-Cd > NaOH-AC-Co > NaOH-AC-Cu > $ZnCl_2$-AC-As. Although the $ZnCl_2$-AC recorded the highest adsorption capacity of 526.31±50.52 mg/g for Hg(II), the KOH-AC showed the strongest affinity of 1.029±0.39 L/mg for Pb(II). This means that the KOH-AC could be very efficient for Pb(II) removal from very dilute AMD solutions (Oyewo et al., 2018).

Table 2

Estimated parameters of the Langmuir isotherm model

Adsorbent-metal	Langmuir Model		
	q_m (mg/g)	b (L/mg)	R^2
$ZnCl_2$-Hg	526.31 ±50.52	0.017 ±0.002	0.976
$ZnCl_2$-As	26.14 ±0.23	0.013 ±0.0005	0.999
KOH-Pb	426.62 ±20.68	1.029 ±0.39	0.993
NaOH-Cd	164.24 ±11.54	0.063 ±0.03	0.990
NaOH-Cu	129.95 ±6.31	0.028 ±0.008	0.986
NaOH-Co	141.75 ±26.01	0.002 ±0.0001	0.989

Table 3

Estimated parameters of the Freundlich isotherm model

Adsorbent-metal	Freundlich Model		
	k (L/g)$^{1/n}$	n	R^2
$ZnCl_2$-Hg	204.12 ±22.47	4.74 ±1.12	0.977
$ZnCl_2$-As	4.64 ±1.20	4.06 ±0.69	0.971
KOH-Pb	198.92 ±39.54	8.15 ±2.29	0.918
NaOH-Cd	39.16 ±6.42	5.47 ±0.83	0.979
NaOH-Cu	28.95 ±5.06	5.02 ±0.73	0.981
NaOH-Co	2.72 ±1.28	1.86 ±0.25	0.973

To provide information on the tendency of the adsorption process by the ACs, the dimensionless constant, R_L in Eq. (4) was derived from the Langmuir model and applied (Bediako et al., 2016; Yan et al., 2012).

$$R_L = \frac{1}{1+ bC_0} \tag{4}$$

where C_0 is the initial metal ion concentration (mg/L). The adsorption process can be described as either favorable ($0 < R_L < 1$), unfavorable ($R_L > 1$), linear ($R_L = 1$),

or irreversible ($R_L = 0$) (Bediako et al., 2016; Yan et al., 2012). Generally, smaller values of R_L ranging between 0 and 1 signify favorable adsorption with good binding affinity. The values obtained in this study were $0.1 < R_L < 0.9$ for the isotherm concentration range evaluated, i.e., 0–1000 mg/L, indicating that the adsorption process was favorable for the entire range of concentrations. The Freundlich model's n values further affirmed that the binding affinities were good and favorable, especially at higher initial concentrations (Yan et al., 2012).

3.4. Kinetics of competitive adsorption in multi-metal mixtures

Kinetics of competitive adsorptions in multi-metal solutions were conducted to estimate the rates of adsorption and identify any likely displacement mechanisms among the competing metal ions (Liu et al., 2008). A multi-metal mixture concentration of 100 mg/L excluding As was prepared. Here, the As (arsenic complex) was omitted due to its inducement of precipitation of other metal ions in the mixture. Similar to the isotherm results, the uptakes of Hg(II) and Pb(II) were significantly more compared to Cd(II), Cu(II) and Co(II). However, the adsorption rates were much faster in the case of the latter set, reaching equilibria within an average of ~1 h, whereas the equilibria of Hg(II) and Pb(II) were achieved between 5–10 h (Figure 4). This adsorption kinetics phenomenon could be understood to be probably due to the smaller atomic sizes of the latter set than the former set.

In a previous study using diethylenetriamine (DETA)-functionalized polymeric adsorbent, it was observed that initially adsorbed Pb(II) was displaced by subsequently adsorbed copper ions, likely because of the greater electronegativity of Cu(II) than Pb(II) (Liu et al., 2008). It was speculated that the displacement mechanism was possibly through the repulsion of Pb(II) and the adjacent attachment of Cu(II). However, this phenomenon was not observed in the present study. All the ACs were observed to show rising data points of uniform and increasing metal ion uptakes until equilibria were reached.

The kinetics data for each metal adsorption were fitted through the pseudo-first-order and pseudo-second-order models given by the following equations:

I) Pseudo-first-order:

$$q_t = q_1(1 - exp\,(-k_1\,t)) \tag{5}$$

II) Pseudo-second-order:

$$q_t = \frac{q_2^2 k_2 t}{1 + q_2 k_2 t} \tag{6}$$

where q_1 and q_2 are the uptakes at equilibrium given in mg/g; q_t is the adsorption capacity at time, t (mg/g); k_1 is the first-order equilibrium rate constant (min^{-1}), and k_2 is the second-order equilibrium rate constant (g/mg·min).

The two kinetic models closely fitted the data with relatively similar R^2 values in most cases; however, the pseudo-second-order provided fairly better fit. The ranges

of R^2 values are summarized in Table 4. The similarities in the model fits depicted a combination of physisorption and chemisorption mechanisms by the ACs (Bediako et al., 2016). Furthermore, the estimated equilibrium uptakes were comparable, especially for the lowly adsorbed metals; however, in some cases, the predictions were underestimations of the actual uptake values, probably due to the rising trends of the data points.

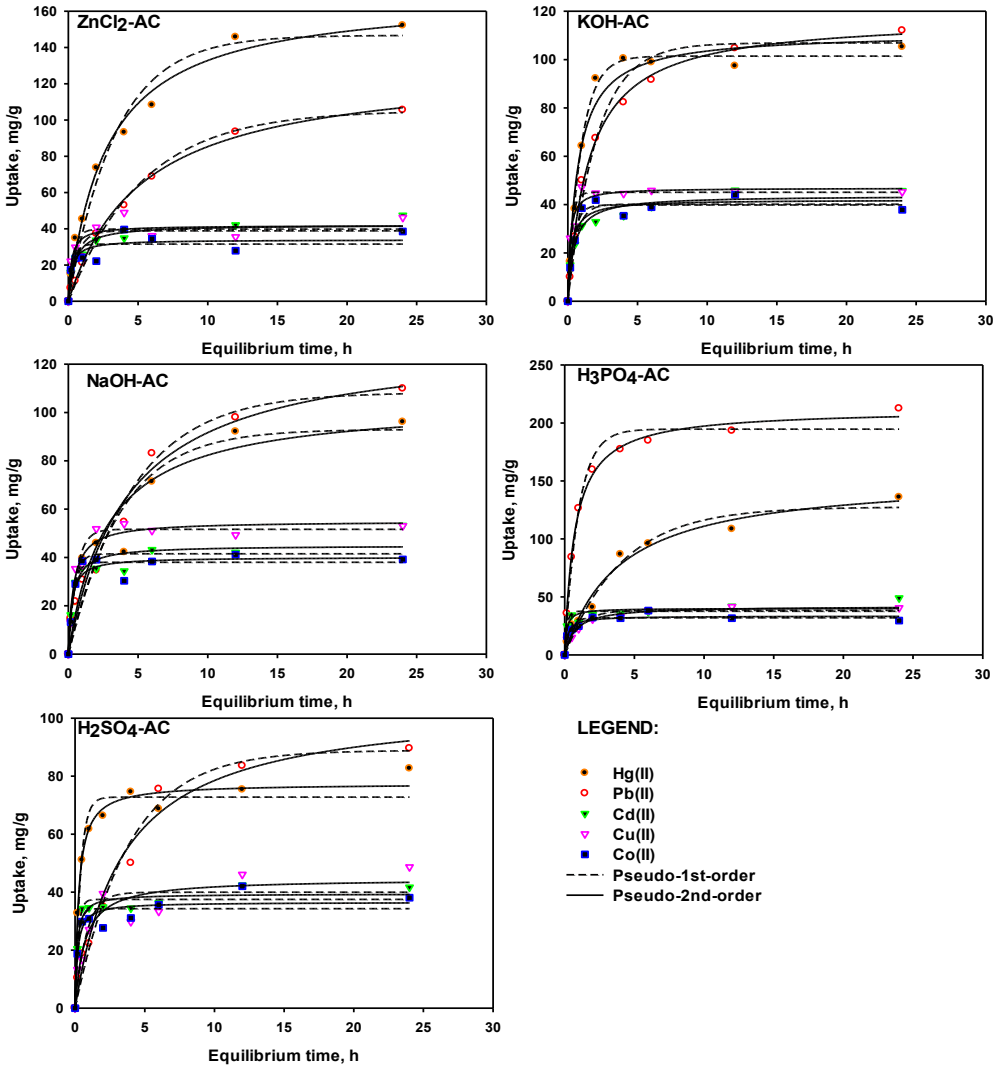

Figure 4

Kinetics of heavy metal adsorption in competitive metal mixtures. Experimental conditions: 0.1 mg ACs in 300 mL of 100 mg/L multi-metal solutions at 120 rpm and 25±2 °C for 24 h

Table 4

Ranges of R^2 values for fitted kinetics data from competitive adsorption

Metal	R^2 pseudo-first-order	R^2 pseudo-second-order
Hg(II)	0.895–0.996	0.925–0.998
Pb(II)	0.964–0.995	0.969–0.998
Cd(II)	0.833–0.953	0.922–0.968
Cu(II)	0.783–0.975	0.846–0.976
Co(II)	0.763–0.962	0.829–0.965

4. CONCLUSION

The adsorptive treatment of heavy metal ions contained in acid mine drainage (AMD) using fruit peel-derived ACs was studied. $ZnCl_2$-AC, KOH-AC, NaOH-AC, H_3PO_4-AC, and H_2SO_4-AC were effective for the removal of Hg(II), As(IV), Pb(II), Cd(II), Cu(II) and Co(II). The order of best adsorption capacity was $ZnCl_2$-AC for Hg(II) > KOH-AC for Pb(II) > NaOH-AC for Cd(II) > NaOH-AC for Co(II) > NaOH-AC for Cu(II) > $ZnCl_2$-AC for As(V), according to the isotherm studies. The kinetics of Cd(II), Cu(II), and Co(II) adsorption were faster than Hg(II) and Pb(II), likely because of the larger atomic sizes of the latter pair. The pseudo-second-order model provided a reasonably better fit to the kinetic data than the pseudo-first-order model. This study could be helpful for promoting sustainable mining practices through the adoption of effective AMD treatment strategies.

ACKNOWLEDGMENTS

The authors wish to acknowledge support from the Research Hub on Sustainable Circular Economy, CiRCLETECH Hub project (101079354) funded by the European Commission through the Horizon Europe programme. Funding support from the Research Council of Finland (decision numbers: 330076 and 358148) is also acknowledged.

REFERENCES

Abudaia, J. A., Sulyman, M. O., Elazaby, K. Y., Ben-Ali, S. M. (2013). Adsorption of Pb (II) and Cu (II) from aqueous solution onto activated carbon prepared from dates stones. *International Journal of Environmental Science and Development*, 4 (2), p. 191.

Acheampong, M. A. (2013). Sustainable gold mining wastewater treatment by sorption using low-cost materials. *SENSE Research School for Socio-Economic and Natural Sciences of the Environment*. *Ph. D. Wageningen University, Delft, The Netherlands*, p. 187.

Akcil, A., Koldas, S. (2006). Acid Mine Drainage (AMD): causes, treatment and case studies. *Journal of Cleaner Production*, 14, pp. 1139–1145.

Bansah, K. J., Yalley, A. B., Dumakor-Dupey, N. (2016). The hazardous nature of small-scale underground mining in Ghana. *Journal of Sustainable Mining*, 15, pp. 8–25.

Bediako, J. K., Kim, S., Wei, W., Yun, Y. S. (2016). Adsorptive separation of Pb (II) and Cu (II) from aqueous solutions using as-prepared carboxymethylated waste Lyocell fiber. *International journal of environmental science and technology*, 13, pp. 875–886.

Bediako, J. K., Lin, S., Sarkar, A. K., Zhao, Y., Choi, J. W., Song, M. H., Cho, C. W., Yun, Y. S. (2020). Evaluation of orange peel-derived activated carbons for treatment of dye-contaminated wastewater tailings. *Environmental Science and Pollution Research*, 27, pp. 1053–1068.

Bediako, J. K., Reddy, D. H. K., Song, M. H., Wei, W., Lin, S., Yun, Y. S. (2017). Preparation, characterization and lead adsorption study of tripolyphosphate-modified waste Lyocell fibers. *Journal of environmental chemical engineering*, 5 (1), pp. 412–421.

Bediako, J. K., Yun, Y. S. (2018). Adsorption of aurocyanide onto KOH-activated orange peel carbons: optimisation of the activated carbon yield and adsorption capacity through central composite design. In *5th UMaT Biennial International Mining and Mineral Conference. Ghana Mining Journal*, pp. 62–67. University of Mines and Technology Tarkwa, Ghana.

Ghana, E. P. A. (2010). Environmental performance rating and disclosure: report on the performance of mining and manufacturing companies. *Environmental Protection Agency, Accra, Ghana*.

Khalil, M. M. H., Al-Wakeel, K. Z., Rehim, S. S. A. E., Monem H. A. E. (2013) Efficient removal of ferric ions from aqueous medium by amine modified chitosan resins. *Journal of Environmental Chemical Engineering*, 1, pp. 566–573.

Li, Y., Du, Q., Liu, T., Sun, J., Wang, Y., Wu, S., Wang, Z., Xia, Y., Xia, L. (2013). Methylene blue adsorption on graphene oxide/calcium alginate composites. *Carbohydrate Polymers*, 95, pp. 501–507.

Li, Z., Kong, Y., Ge, Y. (2015). Synthesis of porous lignin xanthate resin for Pb^{2+} removal from aqueous solution. *Chemical Engineering Journal*, 270, pp. 229–234.

Liu, C., Bai, R., San Ly, Q. (2008). Selective removal of copper and lead ions by diethylenetriamine-functionalized adsorbent: behaviors and mechanisms. *Water research*, 42 (6–7), pp. 1511–1522.

Oyewo, O. A., Agboola, O., Onyango, M. S., Popoola, P., Bobape, M. F. (2018). Current methods for the remediation of acid mine drainage including continuous removal of metals from wastewater and mine dump. In *Bio-geotechnologies for mine site rehabilitation*, pp. 103–114. Elsevier.

Yağşi, N. U. (2004). Production and characterization of activated carbon from apricot stones, *Master's thesis, Middle East Technical University*.

Yan, H., Yang, L., Yang, Z., Yang, H., Li, A., Cheng, R. (2012). Preparation of chitosan/poly (acrylic acid) magnetic composite microspheres and applications in the removal of copper (II) ions from aqueous solutions. *Journal of hazardous materials*, 229, pp. 371–380.

Geosciences and Engineering, Vol. 13, No. 1 (2025), pp. 109–115.
https://doi.org/10.33030/geosciences.2025.01.009

MECHANICAL PREPARATION OF END-OF-LIFE MILD HYBRID CAR BATTERY PACK

SÁNDOR NAGY[1,*], TEGE FICSÓR[2], SVETLANA BUTYLINA[3], MANIVANNAN SETHURAJAN[4] TAMÁS KURUSTA[5]
[1,*]*Faculty of Earth and Environmental Sciences and Engineering, University of Miskolc, Hungary; sandor.nagy@uni-miskolc.hu*
[2]*Faculty of Earth and Environmental Sciences and Engineering, University of Miskolc, Hungary; tege018@gmail.com*
[3]*Faculty of Separation Science, LUT School of Engineering Sciences, LUT University, Finland, svetlana.butylina@lut.fi*
[4]*Faculty of Separation Science, LUT School of Engineering Sciences, LUT University, Finland; manivannan.sethurajan@lut.fi*
[5]*Faculty of Earth and Environmental Sciences and Engineering, University of Miskolc, Hungary; tamas.kurusta@uni-miskolc.hu*
[1]*https://orcid.org/0000-0003-1503-3537*
[3]*https://orcid.org/0000-0002-7282-9841*
[4]*https://orcid.org/0000-0002-2608-9424*
[5]*https://orcid.org/0009-0009-2979-1647*

Abstract: Lithium-ion batteries (LiBs) are essential to modern life, their uses range from small button cells to large-scale energy storage systems. While some used cells can be repurposed in energy storage applications, all lithium-ion batteries must undergo processing at the end of their life (EoL). The variety in shape, structure, and chemical composition of Li-ion batteries poses challenges for recycling. The first step in battery processing is mechanical preparation. This involves evaluating the structure of EoL lithium-ion batteries and designing an effective mechanical process. The process includes multiple comminution steps to liberate materials, separate parts, remove hazardous substances, and classify materials for Black Mass extraction.

***Keywords**: lithium-ion batteries, mechanical processing, recycling, black mass*

1. INTRODUCTION

Recycling and processing lithium-ion batteries (LiBs) face several technical challenges and obstacles, including:

- **Variety of Battery Types**: The wide range of LiB types (such as LCO, LFP, LMO, NMC, and NCA) necessitates careful pre-classification and sorting to handle each type appropriately,
- **Size of Battery Packs**: The large size of battery packs and cells makes disassembly labor-intensive and challenging,
- **Flammability Risks**: LiBs are flammable and can ignite or explode due to mechanical stress or even improper storage,

- **Harmful Substances**: These batteries contain materials that are hazardous to human health and the environment, requiring careful separation, disposal, and recycling as part of a closed-loop or circular economy approach during mechanical preparation. Many types of Li-ion batteries (e.g., LCO, LFP, LMO, NMC, and NCA), require appropriate pre-classification and sorting of batteries.

The European Union currently has technologies for processing EoL LiBs, with capacities ranging from several hundred tons to 20,000 tons per year. Various methods, including pyrometallurgical, hydrometallurgical, and metallurgical techniques, have been suggested for recovering metals from LiBs (Roy et al., 2021). LiB processing technologies involving mechanical pretreatment are considered environmentally friendly, as they reduce the need for downstream operations to separate pure metals at later stages. Mechanical processes are generally cost-effective and do not typically require specialized equipment (Javorsky da Costa et al., 2015). In hydrometallurgical processes, mechanical processing serves as the first step, involving battery comminution, separation of structural materials, and extraction of the black mass (Brückner et al., 2020).

Implementing specialized processes can address several technical issues. For example, discharging batteries is often necessary before shredding to prevent short circuits and fire hazards (Mádainé et al., 2020). However, discharging may not be required with wet shredding or freezing methods. Shredding can also be performed in inert atmospheres (e.g., CO_2 or nitrogen) or under vacuum, and wet technologies are available for electrolyte removal, which can be achieved through thermal treatment or vacuum application (Greenwood et al., 2020).

The primary objective of this research is to extract the black mass from battery cells. A comprehensive material balance of the entire hybrid system and battery cell processing was conducted to use the results as a foundation for practical applications.

2. MATERIAL AND METHODS

2.1. Material

The experiments were carried out on Ford Transit mild hybrid car battery pack (Figure 1), from Auto Mandy Car Ltd., Budapest (Hungary). The battery package weighed 16.02 kg and included the battery cells, inverter, battery management system (BMS), connection circuits, and cooling system. The pack also included safety fuses and protective housing to prevent overheating and ensure operational safety. These components illustrate the intricate design of modern hybrid battery systems, emphasizing the challenges involved in disassembling, and processing these units.

Figure 1
Unassembled Ford Transit battery pack

2.2. Methods

The battery pack was manually dismantled using hand tools, which involved removing of the releasable connection. After this, the battery cells were discharged by connecting them directly to a resistance (Kwade and Diekman, 2018), followed by manual and mechanical processing.

The battery cell was opened using a two-axis rotary shear shredder. Once opened, the electrolyte solvent was removed by heat treatment (Colledani et al., 2023) using the Memmert UFE 400 type drying oven at 60 °C for 24 hours.

After the electrolyte was removed, the battery cell was mechanically crushed using a hammer crusher with a 20 mm sieve. The crushed battery cell material was sorted using an airflow separator with an air speed of 2.54 m/s. Separation was carried out into the following particle size fractions: >16; 16–12; 12–8; 8–4 mm. Particles smaller than 1 mm are referred to as black mass.

The qualitative analysis of materials and their identification was carried out on the FT/IR-4200 type A Fourier Transformed Infrared Spectrometer (JASCO) with a diamond ATR accessory. The spectra were obtained in a reflection mode.

The leached metals were analyzed using Varian Inc.'s 720-ES inductively coupled plasma (ICP) spectrometry. For the calibration of the device, a series of solutions were prepared from the certified multielement standard solutions, Certipur (distributed by Merck Ltd). and the Spectrascan (distributed by Teknolab).

3. RESULTS

3.1. The manual dismantling of the hybrid system

The material balance after dismantling is shown in Table 1. The system could be split into 5 units without destruction. The largest part was the battery pack (40.60 wt%). The battery pack was treated separately and is, therefore, not included in the table. This is followed by the system case, which consists of an iron base plate (2.64 kg) to which the hybrid system is attached, and a plastic cover (2.06 kg) held together by screws and weighs 5.29 kg. The air cooling fans, and the aluminium-copper heat exchanger of the inverter are integrated into the plastic cover. Next to it is the inverter, which consists of a large aluminium heat exchanger, an AC/DC converter, and control electronics. During disassembly, the removed screws, cables, connectors, and sensors were collected; together these weighed approx. 1.2 kg.

Table 1

Hybrid system units and their component materials (unit: wt%)

Material	Units name (wt%)			
	System case	Inverter	Cooling system	Other parts (screws, plugs, sensors)
Plastic	39.06	5.00	63.46	4.10
Iron	49.83	0.00	0.00	47.39
Aluminum	6.44	46.29	23.27	1.46
Glass	4.68	9.08	0.00	0.00
PCB	0.00	38.41	0.00	0.00
Rubber	0.00	0.00	3.24	7.23
Copper	0.00	1.21	10.04	24.04
Zinc	0.00	0.00	0.00	15.78
Unit/Battery system	33.38	17.13	1.22	7.67

3.2. Processing of the battery cells

During the research, not only was the mechanical processing of the battery cell carried out, but also the manual disassembly of a cell.

3.2.1. Results of manual dismantling

Manual disassembly of the battery cell structure and its quantitative and qualitative composition were investigated. In terms of construction, the battery is coated with a cellular composite casing, in which the anode, separator foil and cathode are layered.

According to the FT-IR measurements, the cell coating is a composite material consisting of polyethylene terephthalate-aluminium-polypropylene, PET-Al-PP. The cell casing provides 16.19 wt% of the total mass, with an aluminum content of 19–25 wt% based on volume concentration. The cathode foil consists of 28 aluminium plates, each 0.005 mm thick. It accounts for 2.51 wt% of the total cell

mass. The anode foil consists of 29 copper plates, each 0.004 mm thick, making up 6.48 wt% of the cell. The separator foil between the anode and cathode plates provided 4.49 wt% of the total mass. Since the anode and cathode active materials could not be separated by the used technology, their mass fraction was determined as one, which amounted to 54.1 wt% of black mass.

During disassembly, the electrolyte content was determined by measuring the mass loss of the cells. The electrolyte content is 16.3 wt%, with a significant portion (10 wt%) removed shortly after opening the cell. The gas that is initially released contains mainly organic solvents (ethyl methyl carbonate [EMC]; dimethyl carbonate [DMC]) and CO_2 (Vetter et al., 2005; Aurbach et al., 2002).

3.2.2. Results of mechanical processing

Mechanical processing was carried out on electrically discharged batteries. The first stage of the process was to open the batteries and remove the electrolyte solvent with heat treatment. The 15.8 wt% electrolyte solvent left the cell, which is almost the same value as measured during manual dismantling. Since with this technology the electrolyte cannot be recovered, 100 wt% of the solid sample was used.

The particle size distribution and fractional composition of the battery cell after crushing in the hammer crusher are shown in Figure 2. According to the analysis, particles above 4 mm make up 60% of the sample's composition. Of these, 3/4 are metals with a partial black mass coating and 1/3 is separator foil. The fraction between 1 and 4 mm was composed of anode and cathode particles that were almost completely free of separator foil, with a significant coating of black mass. No further processing was done for particles between 1 and 4 mm.

(a) (b)

Figure 2

Main units of the hybrid system, (a) inverter and (b) battery pack.

The fraction below 1 mm, considered as a black mass, represented ~40 wt% of the sample. The composition of the extracted black mass, analyzed by ICP, is shown in Table 2. According to the results of the analysis, it has been determined that the battery that was processed is of NMC type. Upon analyzing the extracted black mass, it has been observed that it contains some amount of aluminum and copper foil fragments.

Table 2

Chemical composition of black mass

Chemical components	Ni	Mn	Cu	Ti	Al	Co	Fe	Li
wt%	17.3	3.49	3.95	0.98	0.91	4.53	0.07	3.39

3.2.3. Extraction of copper and aluminium

Valuable metals (aluminum and copper foil) with minor black mass coating were enriched in particle size fraction 4–16 mm. However, this fraction consisted of 70% separator foil by volume. The separation of metal and plastic was carried out in an airflow separator, with particle size fractions of 12–16- and 8–12-mm. Results of the separation are shown in Figure 3. Based on the measurement results, the optimal airflow velocity is 2.68 m/s. At this velocity, the metal content loss is at its minimum, but 95 wt% of the separator film will be transferred to the product with low settling velocity.

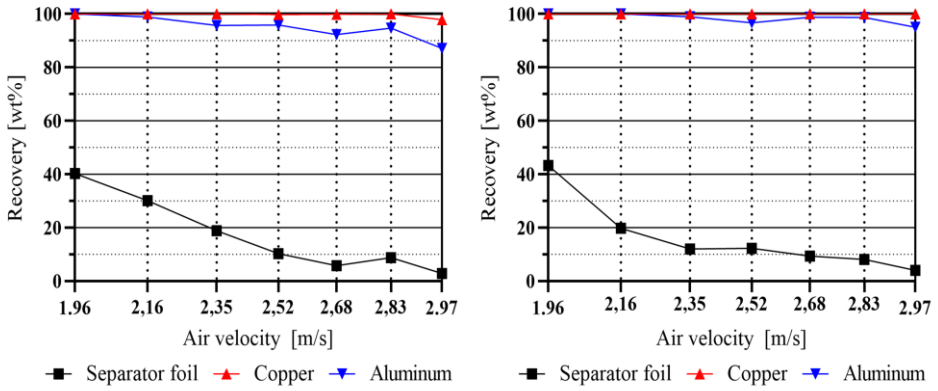

(a) *(b)*

Figure 3

Material recovery in the high settling velocity products in air separator by airspeed (a) Particles between 4–8 mm; (b) Particles between 8–12 mm

4. DISCUSSION AND CONCLUSIONS

The cells can be well opened with a rotary shear crusher, after which the electrolyte can be completely removed by heat treatment at 60 °C for 48 hours. It was found that the technology used can recover approximately 74% of the black mass. Results show that more than 90% pure black mass can be obtained by mechanical processes. Further black mass is also found in the coating moulds of the product with a high settling velocity and on the surface of the 1 to 4 mm particles from the hammer crusher.

As the research progresses, we plan to classify the anode and cathode grains, and to remove and recover the black mass adhered to the surface of the particles.

ACKNOWLEDGMENTS

The research was funded by the Sustainable Development and Technologies National Programme of the Hungarian Academy of Sciences (FFT NP FTA). This project is funded by the European Union's Horizon Europe program under grant no. 101079354.

REFERENCES

Aurbach, D., Markovsky, B., Rodkin, A., Cojocaru, M., Levi, E., Hyeong-Jin, K. (2002). An analysis of rechargeable lithium-ion batteries after prolonged cycling. *Electrochimica Acta*, 47 (12), pp. 1899–1911. https://doi.org/10.1016/S0013-4686(02)00013-0

Brückner, L., Frank, J., Elwert, T. (2020). Industrial Recycling of Lithium-Ion Batteries – A Critical Review of Metallurgical Process Routes. *Metals*, 10 (8), p. 1107. https://doi.org/10.3390/met10081107

Colledani, M., Gentilinic, L., Mossalib, E., Picone, N. (2023). A novel mechanical pre-treatment process-chain for the recycling of LiIon batteries. *CIRP Annals*, 72 (1), pp. 17–20. https://doi.org/10.1016/j.cirp.2023.04.068

Greenwood, D., Dowson, M., Unadkat, P. (2020). *Automotive Lithium-ion Battery Recycling in the UK. Based on a feasibility study by Anwar Sattar*. Canley, University of Warwick.

Javorsky da Costa, A., Matos, J. F., Bernardes, A. M., Müller, I. L. (2015). Beneficiation of cobalt, copper and aluminum from wasted lithium-ion batteries by mechanical processing. *International Journal of Mineral Processing*, 145, pp. 77–82. https://doi.org/10.1016/j.minpro.2015.06.015

Kwade, A., Diekmann, J. (2018). *Recycling of Lithium-Ion Batteries*. Springer Cham

Mádainé Üveges, V., Bokányi, L., Papp, R. Z., Szamosi, Z., Romenda, R. R., Nagy S. (2020). Valuable elements in waste electrical & electronic equipment (WEEE) and their possible recovery methods introduction. *Geosciences and engineering: a publication of the University of Miskolc*, 8 (12), pp. 71–83.

Roy, J. J., Cao, B., Madhavi, S. (2021): A review on the recycling of spent lithium-ion batteries (LIBs) by the biobleaching approach. *Chemosphere*, 282, pp. 130944. https://doi.org/10.1016/j.chemosphere.2021.130944

Vetter, J., Novák, P., Wagner, M. R., Veit, C., Möller, K. C., Besenhard, J. O., Winter, M., Wohlfahrt-Mehrens, M., Vogler, C., Hammouche A. (2005). Ageing mechanisms in lithium-ion batteries. *Journal of Power Sources*, 147 (1–2), pp. 269–281. https://doi.org/10.1016/j.jpowsour.2005.01.006

Geosciences and Engineering, Vol. 13, No. 1 (2025), pp. 116–126.
https://doi.org/10.33030/geosciences.2025.01.010

COMPARATIVE INVESTIGATION OF EGGSHELL'S PARTICLE SIZE DISTRIBUTION AS FOAMING AGENT FOR MANUFACTURING GLASS FOAM

ILDIKÓ FÓRIS[1,*], THOMAS MÜTZE[2], MIIA JOHN[3], GÁBOR MUCSI[4]
[1]*Faculty of Earth and Environmental Sciences and Engineering, University of Miskolc, Hungary*
ildiko.foris@uni-miskolc.hu
[2]*BASF Battery Materials and Recycling Schwarzheide GmbH, Germany*
thomas.muetze@basf.com
[3]*LUT School of Engineering Science, LUT University, Finland*
miia.john@lut.fi
[4]*Faculty of Earth and Environmental Sciences and Engineering, University of Miskolc, Hungary*
gabor.mucsi@uni-miskolc.hu
[1]*https://orcid.org/0000-0003-3497-3954*
[3]*https://orcid.org/0000-0001-5139-9697*
[4]*https://orcid.org/0000-0003-1031-2801*

Abstract: Various waste materials have been repurposed as secondary raw materials for producing environmentally friendly building products. One type is glass foam which is a thermal insulation material. To produce glass foams, glass powder is mixed with a foaming agent and treated at temperatures higher than 600 °C to inflict gas formation. An essential step in preparing the raw materials is grinding them to an optimal particle size range. Eggshells, due to their high calcium carbonate content, can serve as a foaming agent. However, their plate-like structure makes it challenging to accurately determine size parameters. This study presents a comparison of two different analytical methods—laser diffraction (LD) and dynamic image analysis (DIA). The results show that as grinding time increases, particle size decreases and sphericity improves. Particle breakage begins after 16 minutes, achieving optimal size at 30 minutes. Consistency is observed between the measurement methods at 60 minutes of grinding as particles become more compact and spherical.

Keywords*: eggshell, grinding, recycling as foaming agent, ball milling, glass foam*

1. INTRODUCTION

With increasing urbanization, the consumption of non-renewable raw materials continues to rise, leading to significant environmental issues if not disposed of properly (Cheng et al., 2016; Liu et al., 2019; Shelby, 2017). Effective waste management is essential for promoting sustainable development.

Glass foams are environmentally friendly materials if made from secondary raw materials (Fóris and Mucsi, 2023a; Scarinci et al., 2005; Souza et al. 2017; Assefi et al., 2021; Cengizler et al., 2021). They can be used as aggregate, heat insulation, or

filler because of their many positive features like being lightweight, highly porous, chemically neutral, non-flammable, and frost-resistant. With relatively low thermal conductivity, glass foams effectively prevent heat transfer (Goltsman and Yatsenko, 2023). Those foams open new opportunities for waste materials such as glass and eggshell powder to make a high-value product that easily fits into the circular economy concept. A key disadvantage of glass foams is the production cost, which is attributed to high raw material expenses (using SiC as a foaming agent) and energy-intensive processes, like milling and thermal treatment.

To produce glass foams, foaming agents are necessary to create pores (Da Costa et al., 2020). The foaming agents release gas in the molten glass during decomposition. Carbonates are cost-effective types of foaming agents (Thulasikanth and Padmanabhan, 2023). One example of this is eggshell (Fóris and Mucsi, 2023b) due to its high calcium carbonate content. Eggshells (ES) are one of the most abundant food wastes through everyday egg consumption. 50,000 tons of ES waste are generated approximately every year worldwide (Das et al., 2022). Eggshells' main constituent is calcium carbonate (94–96%) or more specifically calcite in crystalline form (Baláž, 2018). It is suitable for forming a porous structure in glass foams because CO_2 is generated during the thermal decomposition of calcium carbonate at high temperatures (700–900 °C) (Souza et al., 2017; Osfouri and Simon., 2022).

An essential step in glass foam production is grinding the raw materials to the optimal size. Generally, raw materials need to be ground to less than 100 μm for effective foaming (Guo et al., 2023; Bueno et al., 2020). The particle size of the foaming agent directly influences the pore size and foaming behavior. If the particle size of the foaming agent is uniform, the resulting glass foam structure is homogeneous, which is advantageous regarding its material specification (Spence and Kultermann, 2016).

The primary challenge with eggshells lies in their plate-like particle shape, making it difficult to accurately determine the particle size distribution. To accurately characterize the particle size and morphology of raw materials such as eggshell powder, advanced measurement techniques are required. Conventional sieving often fails to capture fine fractions and irregular particle geometries. Among the widely used techniques, laser diffraction and dynamic image analysis provide complementary information. In the following, LD will be used to refer to laser diffraction, and DIA to dynamic image analysis.

LD is based on the principle that particles scatter light at angles inversely proportional to their size, allowing rapid determination of particle size distribution over a wide range. LD is advantageous due to its speed, reproducibility, and ability to measure large sample volumes, but it assumes spherical particle geometry. This limitation can lead to inaccuracies when analyzing materials such as eggshells, which often have irregular, plate-like morphologies.

DIA, on the other hand, directly captures two dimensional images of particles in motion, enabling simultaneous evaluation of both size and shape descriptors (e.g., aspect ratio, sphericity, convexity). Although DIA provides detailed morphological

information, it generally requires longer measurement times, careful sample dispersion, and larger datasets for statistical reliability.

This study aimed to examine the effects of grinding on the particle size distribution and shape parameters of eggshells using two different methods: laser diffraction and dynamic image analysis.

2. MATERIALS AND METHODS

The raw material consisted of chicken eggshell waste, which was subjected to ball milling for varying durations ranging from 1 to 60 minutes (Figure 1). A general overview of the physical characteristics of the chicken eggshell is presented in Figure 2. This figure illustrates the layered structure of an ES, showcasing its unique hierarchical architecture. Starting from the outermost layer, the eggshell consists of a cuticle colloid layer and a surface layer, which provide a protective coating. Below this lies the palisade layer, composed of tightly packed materials that add strength and support. The mammillary layer follows, featuring structures that connect to the underlying fiber membrane. Notably, the structure contains gas pores and bubble pores that enable gas exchange, which are essential for biological processes. Additionally, sub-layers like the sub-micro-sphere layer and nano-line layer contribute to the eggshell's strength and rigidity, while the outer and inner membranes form a barrier that further reinforces the structure (Hincke et al., 2012).

Before milling, ES waste was heat-treated in boiling water for 30 minutes to remove the organic content. Then the material was dried at 105 °C for 2 hours until mass consistency. Before milling, the ES was kept in a desiccator at room temperture (25 °C). The eggshell's thickness was measured with a digital gauge. The average thickness was 401 ±28.29 μm.

The grinding process utilized a planetary mill with stainless steel balls of 10 and 20 mm diameter as the grinding media. Throughout the experiment, eggshell is referred to as ES.

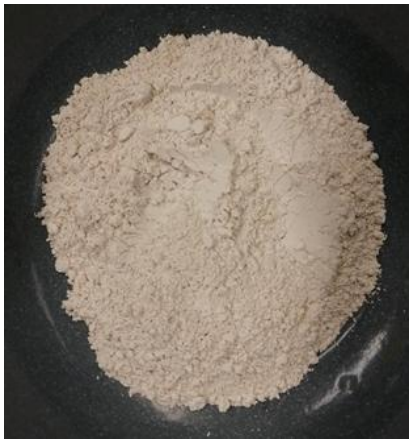

Figure 1
ES powder after 60 minutes grinding

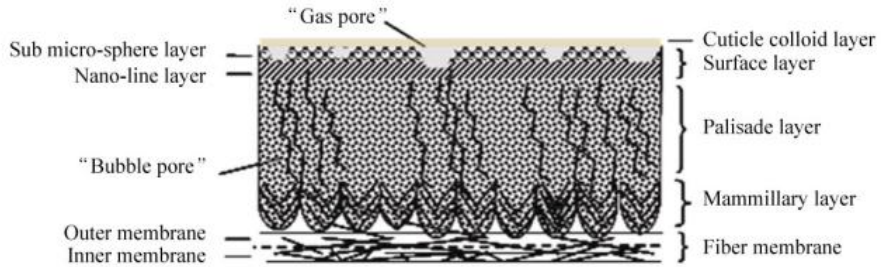

Figure 2
Description of ES (chicken ES) (Zhou et al., 2011)

2.1. Methods for raw material characterization

The chemical compositions of eggshells were measured by a Rigaku Supermini 200-type wave-length X-ray fluorescence spectroscope (XRF). The loss of ignition (LOI) was measured at 950 °C with 90 min heating rate, and 60 min holding time in a static furnace. The XRF and LOI experiments were carried out from the original sample (before ES was heat-treated in boiling water). Table 1 shows the results of XRF and LOI measurements. The primary component of the eggshell is CaO, comprising 54.5% of the total mass, reflecting the high calcium carbonate content of the eggshells. The LOI content is relatively high at 45.7%, indicating a significant amount of volatile material during thermal treatment. These values highlight the suitability of eggshells as a potential source of calcium carbonate for applications such as foaming agents in glass foam production.

Table 1
Chemical composition and loss of ignition of ES

	$(^{m}/_{m}\%)$
SiO_2	0.3
Al_2O_3	0
MgO	0.62
CaO	54.4
Na_2O	0.13
K_2O	0.13
Fe_2O_3	0.03
MnO	0.001
TiO_2	0.002
P_2O_5	0.499
S	0.21
F	<0.3
LOI	45.71

2.2. Methods for ES powder characterization

The ground powders were analyzed with two different methods. For the first method LD, a Horiba LA-950 V2 laser diffraction particle size analyzer was used in wet conditions using distilled water as dispersing media, applying the Fraunhofer theory. For the second method DIA, Retsch Camsizer XT dynamic image analyzer was used in dry conditions. To evaluate the influence of milling on the shape properties, the parameter sphericity (surface rounding of grains) SPHT was selected

$$\text{SPHT} = 4\,\pi\,(\text{particle area}) / (\text{particle perimeter})^2 \quad (1)$$

For the sphericity, the mean value, and the confidence interval of a 95 % level of confidence were calculated as

$$\alpha_{bottom} = \bar{X} - t_{0,95} * \frac{S_n^*}{\sqrt{n}} \quad (2)$$

$$\alpha_{\text{top}} = \bar{X} + t_{0,95} * \frac{S_n^*}{\sqrt{n}} \quad (3)$$

$$\alpha_{top} - \alpha_{bottom} \quad (4)$$

where $\bar{x}$ is the mean, $t_{0.95}$ is the t-distribution value at 95 % confidence level, S_n^* is standard deviation, n is the number of values, α_{bottom} is the lower limit of the 95% confidence interval, α_{top} is the upper limit of the 95% confidence interval.

3. RESULTS AND DISCUSSION

Particle size distributions are provided in Figures 3 and 4 in volume distribution (Q_3) with the two different devices (Horiba LA-950 V2 and Retsch Camsizer X2).

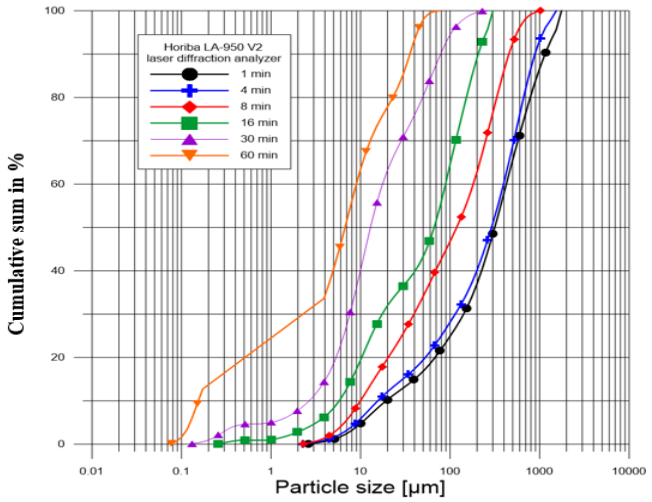

Figure 3

Particle size distribution curves at different grinding times (laser diffraction analyzer Horiba LA-950 V2)

In Figure 3 the LD results showed no major size reduction before 4 min of grinding. At 8 minutes, the particle size starts to decrease significantly. At 30 minutes, the particle size distribution is much finer with the majority (97.88%) of the particles falling below 100 µm, indicating sufficient grinding. The curve suggests that grinding at this stage reaches an optimal balance for producing finer particles. By 60 minutes, the particle size distribution shifts even further, with a 55% of particles being less than 10 µm in size. This demonstrates that with prolonged grinding, the particle sizes become even smaller and more homogeneous, as the curve becomes steeper, suggesting more uniform particle sizes. The 30-minute grinding represents a good trade-off between size reduction and energy input, as particles below 100 µm are achieved, which is typically suitable for applications in glass foam production.

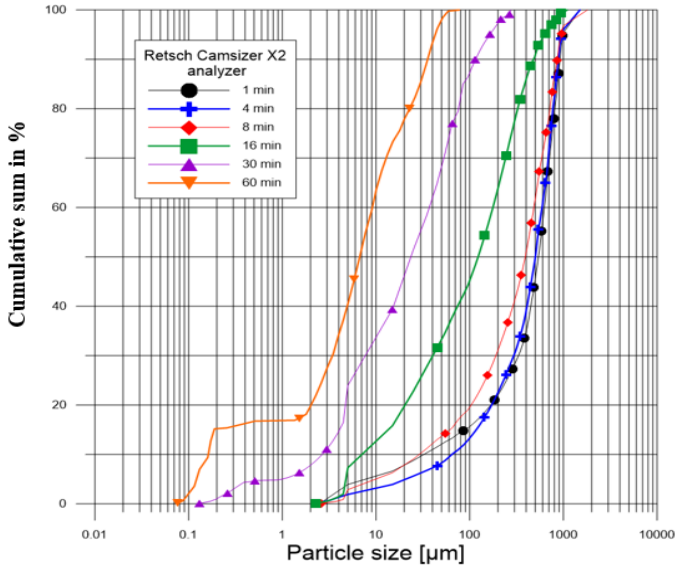

Figure 4

Particle size distribution curves at different grinding times (dynamic image analyzer Retsch Camsizer X2)

During the DIA method with Retsch Camsizer X2 the diameter of circumference was used to evaluate the particle size distribution. Similar to the previous graph, short grinding times (1–8 minutes) show no significant size reduction. By 16 minutes, approximately 85% of the particles fall within the 1–100 µm range, although the distribution is still relatively broad. After 30 minutes of grinding, 85% of the particles have shifted to a smaller size range, with most particles below 100 µm. The distribution becomes narrower, indicating more uniform particle sizes. Comparing the two methods, the major size reduction starts after 8 minutes of processing. With the increasing grinding time, the particle size reduces respectively, this trend can be seen in the case of both methods. However, slight fluctuations between the methods can be observed at shorter grinding times, as shown in Figure 5.

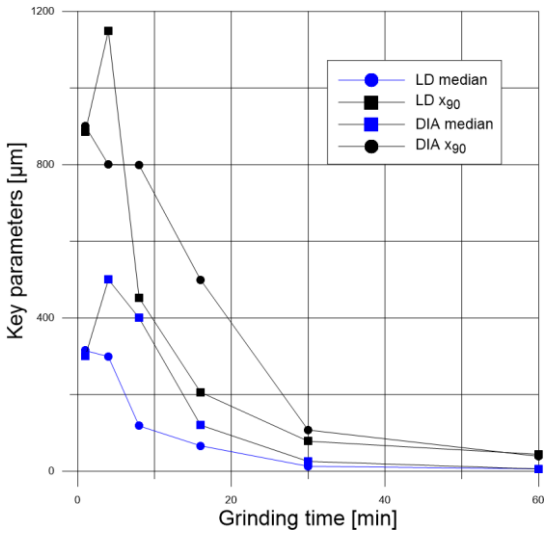

Figure 5
Key parameters measured by Camsizer (DIA) and Horiba LA-950 V2 laser diffraction analyzer (LD)

In Figure 5, it can be noticed that the key parameters of the PSD (median and x_{90}) decrease with increasing grinding time. An increase of the upper particle size x_{90} can be observed from 1 to 4 minutes of grinding, which can be an artefact due to particle shape. This artefact in particle size distribution is due to the anisotropic shape of the particles, which causes inconsistent measurements depending on their orientation during analysis. Both LD and DIA show a clear trend of particle size reduction with increasing grinding time. The particle size distribution stabilizes after around 30 minutes of grinding, where the differences between the two methods become minimal. For early grinding times, DIA may be more sensitive to larger, irregularly shaped particles like the plate-like structure of eggshells, whereas LD seems to show slightly smaller particle sizes initially. The reason for this is DIA measures the longest axis of irregular particles, it records larger sizes for plate-like eggshell fragments, while LD assumes spherical equivalents and therefore reports slightly smaller particle sizes at early grinding times. Both methods are effective in tracking particle size reduction over time, and after 30 minutes, both converge to show a similar particle size distribution, indicating more homogeneous particles.

In Figure 6, the SPHT values indicate that the sphericity of the particles increases with prolonged grinding time. As grinding progresses, the particles become more compact, gradually losing the plate-like structure of ES. A steady rise in sphericity is observed as grinding time extends with minimal changes detected before 8 minutes. This observation aligns with the particle size distribution measured by DIA, which also shows little variation in the early stages of grinding. However, by 60 minutes, a substantial improvement in sphericity is evident compared to the 1-minute grinding.

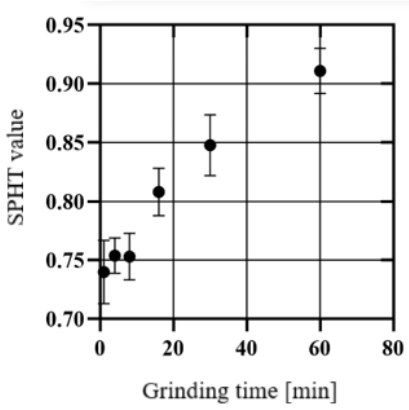

Figure 6
Sphericity results measured by Camsizer (DIA) analyzer at different grinding times

This tendency correlates with the two different methods. Laser diffraction makes the convenient assumption that every particle is a sphere, so where the SPHT values are close to 1, the LD and DIA methods show similar results. This similarity in results is apparent after 30 and 60 minutes of grinding. However, at shorter grinding times (1–8 minutes), notable discrepancies are observed. Laser diffraction indicates a significantly larger fraction of particles below 100 µm compared to image analysis, which still records most particles in the coarser size range. During the initial grinding phase (up to 8 minutes), the particles retain much of their original size and shape. Only after 16 minutes do the particles begin to break down at the plate edges and decrease in size. Concurrently, a major increase in sphericity is observed, reflecting the loss of their plate-like structure and a shift toward a more spherical shape.

The experimental results highlight the significant influence of grinding time on eggshell particle size and morphology, as well as the suitability of different analytical methods for particle characterization. Particle breakage was observed to occur mainly after 16 minutes of grinding, with an optimal fraction of particles smaller than 100 µm being achieved after 30 minutes. These findings are consistent with the observations of Baláž (2018), who reviewed ball milling of eggshells and reported that extended grinding enhances fineness and reactivity, although the efficiency of the process is strongly influenced by the original morphology of the material (Baláž, 2018). Similarly, Guo et al. (2023) demonstrated that the fineness of glass-based aggregates has a direct effect on the performance of lightweight concretes, reinforcing the need to optimize grinding conditions to obtain desirable particle properties (Guo et al., 2023).

The results also showed that longer grinding time increases particle sphericity, as particles gradually become more compact and rounded. This is in line with the descriptions by Zhou et al. (2011) and Hincke et al. (2012), who reported that the hierarchical, plate-like structure of eggshells presents challenges for comminution

(Zhou et al., 2011, Hincke et al., 2012). These structural characteristics explain why short grinding times do not yield strong correlations between particle size and shape.

The results indicate that DIA provides more reliable measurements at shorter grinding times, when particles retain their plate-like geometry, since it records particle dimensions directly from images. However, with extended grinding (60 minutes), the results from DIA and LD converge due to the particles' increasing sphericity, leading to a high level of agreement between the two methods. This dual applicability of LD and DIA highlights the importance of combining complementary techniques for accurate characterization. While Spence and Kultermann (2016) noted that uniform particle size enhances the homogeneity of construction materials, studies have not explicitly compared LD and DIA in the context of waste-derived powders.

In summary, this study confirms that systematic grinding is essential to overcome the plate-like morphology of eggshells, with particle size reduction and sphericity improvement directly influencing the effectiveness of eggshells as a foaming agent. Furthermore, the complementary use of LD and DIA provides a more complete characterization of particle properties, offering methodological guidance for future investigations.

4. CONCLUSIONS

During the experiments, systematic grinding tests were carried out and particle size distribution and particle shape distribution were investigated. The following conclusions were observed from the measurements:

- The breakage of the particles occurs at 16 minutes. Before that, the size and shape parameters do not change a lot (1–8 minutes),
- As the grinding time increases, a gradual decrease in particle size can be seen with an optimal size fraction of <100 μm being achieved after 30 minutes of grinding,
- With increasing grinding time, the particle size decreases and the particles' sphericity value increases because of more compact particles,
- At shorter grinding times, the two results do not correlate because of the plate-like shape of the particles. More energy and longer grinding are required to break these particles down. DIA measures an average of the longest, medium, and shortest physical dimensions of the plate-like particles, therefore bigger particles are measured compared to LD method,
- At the 60-minute grinding interval, the particle size distributions obtained by the two evaluation methods exhibit a high degree of agreement, primarily due to the particles' sphericity values approaching unity. Due to the plate-like nature of eggshells at shorter grinding times, DIA method is suggested to investigate particle size distribution, but at longer grinding times (60 minutes of grinding) LD analyses can give reliable results because the particles become more compact and spherical the effect of grinding.

ACKNOWLEDGEMENTS

The authors wish to acknowledge support from the Research Hub on Sustainable Circular Economy, CiRCLETECH Hub project (101079354) funded by the European Commission through the Horizon Europe programme.

REFERENCES

Assefi, M., Maroufi, S., Mansuri, I. and Sahajwalla, V. (2021). High strength glass foams recycled from LCD waste screens for insulation application. *Journal of Cleaner Production*, 280, pp. 124311–124320.

Baláž, M. (2018). Ball milling of eggshell waste as a green and sustainable approach: A review. *Advances in Colloid and Interface Science*, 256, pp. 256–275.

Boris M. Goltsman, Elena A. Yatsenko (2023). Dynamics of foam glass structure formation using glass waste and liquid foaming mixture. *Journal of Cleaner Production*, Volume 426, p. 138994.

Bueno, E. T., Paris, J. M., Clavier, K. A., Spreadbury, C., Ferraro, C. C. and Townsend, T. G. (2020). A review of ground waste glass as a supplementary cementitious material: A focus on alkali-silica reaction. *Journal of Cleaner Production*, 257, p. 120180.

Cengizler, H., Koç, M. and Şan, O. (2021). Production of ceramic glass foam of low thermal conductivity by a simple method entirely from fly ash. *Ceramics International*, 47, pp. 28460–28470.

Cheng, J.H., Dai, S. and Ye, X.Y. (2016). Spatiotemporal heterogeneity of industrial pollution in China. *China Economic Review*, 40, pp. 179–191.

Da Costa, F. P., Da Silva Morais, C. R., and Rodrigues, A. M. (2020). Sustainable glass-ceramic foams manufactured from waste glass bottles and bentonite. *Ceramics International*, 46, pp. 17957–17961.

Liu, T., Zhang, J., Wu, J., Liu, J., Li, C., Ning, T., Lou, Z., Zhou, X., Yang, Q. and Lu, A. (2019). The utilization of electrical insulators waste and red mud for fabrication of partially vitrified ceramic materials with high porosity and high strength. *Journal of Cleaner Production*, 223, pp. 790–800.

Hincke, M. T., Nys, Y., Gautron, J., Mann, K., Rodriguez-Navarro, A. B. & McKee, M. (2012). The eggshell: structure, composition and mineralization. *Frontiers in Bioscience*, 17, 1266, 80.

Shelby, J. E. (2017). Introduction to Glass Science and Technology. *Royal Society of Chemistry*, 1–3.

Scarinci, G., Brusatin, G., and Bernardo, E. (2005). Glass foams. In Scheffler, M., Colombo, P. (eds.): *Cellular Ceramics: Structure, Manufacturing, Properties and Applications*. Wiley-VCH, Weinheim, pp. 158–176.

Souza, M. T., Maia, B. G. O., Teixeira, L. B., de Oliveira, K. G., Teixeira, A. H. B. and Novaes de Oliveira, A. P. (2017). Glass foams produced from glass bottles and eggshell wastes. *Process Safety and Environmental Protection*, 111, pp. 60–64.

Vaddi Thulasikanth and R. Padmanabhan (2023). Fabrication of sustainable closed-cell aluminium foams using recycled fly ash and eggshell powder. *Materialstoday Communications*, 37, p. 107302.

J. Zhou, S. Wang, F. Nie, L. Feng, G. Zhu, L. Jiang (2011). Elaborate architecture of the hierarchical hen's eggshell, *Nano Res.*, 4, pp. 171–179.

Fóris, I., Mucsi, G. (2023a). Glass foam experiment with eggshell as a foaming agent and red mud as additive material. *Journal of Silicate Based and Composite Materials*, 75, pp. 132–135.

Fóris, I., Mucsi, G. (2023b). Influence of raw material properties on waste-based glass foam. *Mining Geological Petroleum Engineering Bulletin*, 38, pp. 75–83.

Guo, P., Meng, W., Du, J. and Stevenson, L. (2023). Lightweight ultra-high-performance concrete (UHPC) with expanded glass aggregate: Development, characterization, and life-cycle assessment. *Construction and Building Materials*, 371, p. 130441.

Osfouri, M. and Simon, A. (2022). Study on the thermal conductivity and density of foam glass. *Pollack Periodica*, 18, 1, pp. 126–131.

Das, S., Mohanty, P. K., Mallik, B. K. (2022). Agricultural and pharmaceutical applications of eggshells: a comprehensive review of eggshell waste value-added products. *Journal of Pharmaceutical Negative Results*, 13, pp. 3979–3784.

Spence, W. P. and Kultermann, E. (2016). Construction Materials, Methods and Techniques. *Cengage Learning*, pp. 510–526.

Geosciences and Engineering, Vol. 13, No. 1 (2025), pp. 127–137.
https://doi.org/10.33030/geosciences.2025.01.011

PROCESSING OF CONSTRUCTION AND DEMOLITION WASTE FROM CONCRETE

CORNELIUS NGANDU[1, *], JOHN KWAME BEDIAKO[2], GÁBOR MUCSI[3]
[1, *]*University of Miskolc, Hungary, Egerton University, Kenya;*
cornelius.ngunjiri.ngandu@student.uni-miskolc.hu
[2]*Lappeenranta-Lahti University of Technology (LUT), Finland; john.bediako@lut.fi*
[3]*University of Miskolc, Hungary; gabor.mucsi@uni-miskolc.hu*
[1]*https://orcid.org/0000-0003-2877-3534*
[2]*https://orcid.org/0000-0003-1816-4890*
[3]*https://orcid.org/0000-0003-1031-2801*

Abstract: There is a need to develop appropriate techniques and technologies that will upcycle construction and demolition waste as a secondary material. This study aims at improving construction and demolition waste from concrete. Three (3) fractions of materials were processed, jaw crusher and impact crusher were employed. Based on this study, the concrete construction and demolition waste fraction with raw material sizes between 45 to 80 mm, and 22 to 45 mm, could be explored for size range 4 mm to 25 mm (4/25) aggregates production, while the raw sizes 0 to 22 mm, could be investigated for 4 mm to 14 (4/14) aggregates after crushing and some selective sizing. Flakiness indexes were < 7% for the 2 larger size fractions. Further studies are recommended, on other properties.

Keywords*: construction and demolition waste, jaw crusher, impact crusher, aggregates*

1. INTRODUCTION

There has been an increased interest at a global level regarding the reuse and recycling of construction and demolition wastes (CDWs) (Contreras-Llanes et al., 2021). According to the European Environmental Agency (2023, last updated), CDW had a high recovery rate and stable amounts in the EU; however, management practices indicated that CDW recovery was largely based on backfilling operations and low-grade recoveries such as aggregates for road sub-base. Thus, there is a big potential for making CDW management truly circular. To increase the value and feasibility for CDW application, there is a need to develop proper up-cycling techniques. Extensive work has shown that plain and reinforced concrete debris can be crushed by primary or secondary crushers to produce recycled concrete aggregates within acceptable quality to BS 882 requirements (Limbachiya, 2010).

The “equiaxed” nature for impact breaker is advantageous in concrete aggregates (Tarján, 1981). The advantage of vertical shaft impact (VSI) crusher is the ability to produce cubicle shapes, however this shape results in significant quantities of fines (Bengtsson and Evertsson, 2006). In the study of Bengtsson and Evertsson (2006), the flakiness index (FI) from VSI crushed particles was around ½, those from the cone crusher and VSI speed have an influence on the FI, with higher speed producing

lower FI. Besides, a higher velocity VSI increases the proportions of finer particles produced as compared to a lower velocity VSI. Hubert et al. (2023) conducted a study on recycled concrete aggregates and observed that the jaw crusher produced fewer fine particles as compared with the impact crusher. In addition, the impact crusher produced recycled concrete aggregates with less flakiness and shape index as compared with the jaw crusher. However, according to Ulsen et al. (2019), the recycled concrete aggregates end products for jaw and crusher processes were not significantly different with respect to adhered cement paste, density, porosity and particle size distribution. In other words, the differences did not justify the belief that the impact crusher has superior release ratios of recycled concrete aggregates. According to a study by Wang et al. (2024), impact crushing using a water jet for recycled concrete aggregates can result in deterioration of the interfacial transition zone (ITZ), and effectively remove the residual adhered mortar, which could further lead to residual adhered mortar and water absorption values being almost similar to natural aggregates. To improve the quality of recycled aggregates, further treatment could be explored. The study by Qiu et al. (2014), which involved microbial carbonate precipitate treatment, and that of Li et al. (2019) using carbonation treatment, both resulted in reduced water absorption of the treated coarse aggregates.

According to the Advancing Standards Transforming Markets (ASTM) International, ASTM D1883-21, the CBR test can be applied to several engineering applications, such as evaluating the potential strengths of subgrade, subbases, and base course materials, including recycled materials, for flexible roads and airfield pavement designs. Zhang et al. (2021) evaluated recycled aggregates having blended components, and noticed that the aggregate crushing value varied with the amounts of gravel, brick, and mortar. Furthermore, Martinez-Echevarria et al. (2020) observed that California Bearing Ratio (CBR) values for recycled aggregates increased after being submerged, an indication of anhydrous particles that reacted with water. They further noticed that crushing resulted in an increased hydration activity, which could imply that cement particles in the recycled aggregates come to the surface after crushing, and hence increased the hydration activity as well as support capacity increase.

Consequently, this paper systematically examined the impact of crushing on three fractions of concrete CDW in Hungary. Preparations and analysis were conducted at the University of Miskolc. Crushing was done by jaw and impact crushing. The aim of this research is to systematically process and classify CDW for concrete recycled aggregates and geopolymer precursor materials.

2. Materials and Method

Three CDW waste size fractions were classified based on raw particle size (feed sizes) and denoted as CDW I for the 45–80 mm, CDW II for the 22–45 mm and CDW III for the 0–22 mm size ranges. This CDW from concrete waste with very minor impurities observed including wood/twigs. X-ray fluorescence (XRF) was used to determine the chemical composition and loss of ignition (LOI), and the result

is presented in Table 1. Based on the results, the SiO_2 amounts arguably mainly from aggregates, CaO could be attributed to previous binders while LOI from carbonation.

Table 1

Chemical composition and LOI for the CDW materials by XRF.

	CDW III	CDW II	CDW I	< 4mm, jaw crusher
SiO_2	53.94	52.77	52.79	52.97
Al_2O_3	5.21	5.18	4.48	5.79
MgO	1.20	1.36	1.29	1.25
CaO	20.67	22.00	22.97	20.73
Na_2O	0.56	0.55	0.50	0.61
K_2O	1.28	1.21	1.00	1.43
Fe_2O_3	1.51	1.41	1.24	1.61
MnO	0.09	0.10	0.10	0.10
TiO_2	0.16	0.16	0.15	0.19
P_2O_5	0.08	0.08	0.08	0.09
S	0.75	0.91	0.91	0.81
LOI	14.47	14.2	14.41	14.34

2.1. CDW Sampling Preparation

To make the homogenized samples, quartering and/or mechanical splitting techniques were employed based on size to obtain representative samples for both short- and long-term use. Quartering was initially conducted for the 3 categories of concrete CDWs, then mechanical splitting was performed for the CDW III sample, using a 50 mm width splitter based on the largest size as per AASHTO R 76 (Washington State Department of Transportation 2023). Other fractions generally followed ASTM C702 and AASTHO R 76, as described in Gilson Company Inc.

2.2. Crushing and particle size distribution

The raw CDW II & CDW III particle size distributions were done by dry sieving. Sieves of up to 125 mm were used for CDW I, due to their larger sizes. Figure 1 illustrates the raw material particle cumulative undersize graph. A semi-industrial jaw crusher (PE 02 type) was used for CDW I (2 passes) and II (1 pass), then < 4mm was sieved off before the CDW I, II and III were crushed using a RTE 24/18 type horizontal shaft impact crusher, with a rotor circumferential speed of 30 m/s in all cases. Before the CDW material fractions were fed into the impact crusher, the < 4 mm sizes were sieved off. The CDW I and CDW II were crushed by the jaw crusher and impact crusher, whilst CDW III was crushed only by the impact crusher. The type and level of crushing were chosen based on the size-dependent classification. In other words, the CDW III was crushed only by the impact crusher due to its relatively small average particle size. CDW I was subjected to 2 passes jaw crushing with approximate spacings of 30 mm and 20 mm (peak to peak). The jaw crushing of CDW II fraction was passed through approx. 20 mm spacing (peak to

peak). The cumulative undersize for ≥ 4 mm of jaw crushed and raw CDW III material before impact crushing is illustrated in Figure 2.

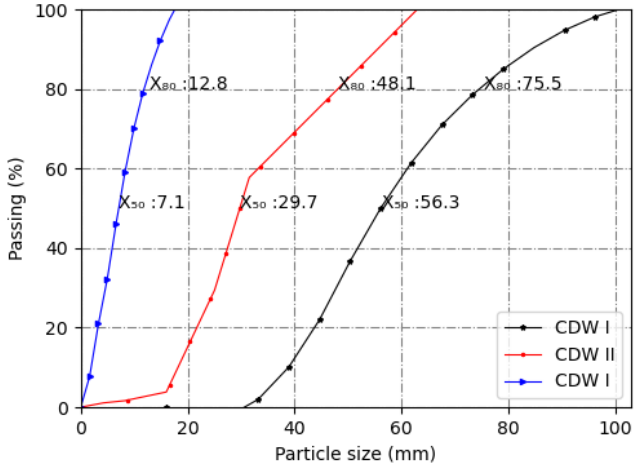

Figure 1

Particle size distribution for the CDW raw materials, sieve sizes of 125 to 16 mm, 6 fractions for CDW I, 63 to 4 mm for CDW II and 31.5 to 1 mm, 4 fractions for CDW III

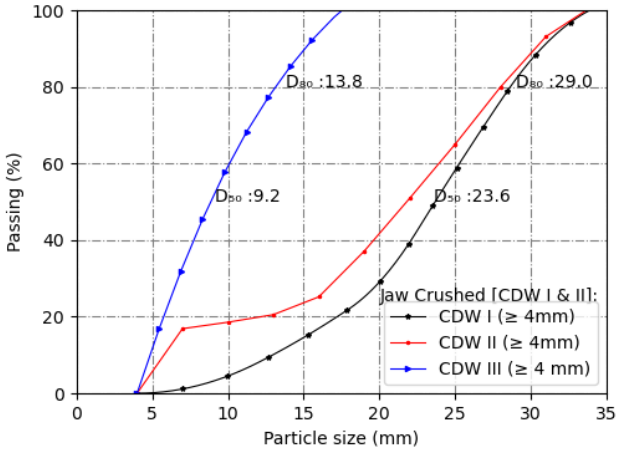

Figure 2

Particle size distribution for the CDW ≥ 4mm for CDW III and jaw-crushed CDW I & II, sieve sizes of 40 to 4 mm.

General crushing and classification steps are illustrated in Figure 3. The particle size distribution for materials with dry seiving, was conducted, with up to 125 mm sieve size, CDW I and CDW II raw materials, for CDW III raw materials dry sieving was up to 31.5 mm. The primary sieve sizes were based on ISO-3310.2 and ISO-3310.1.

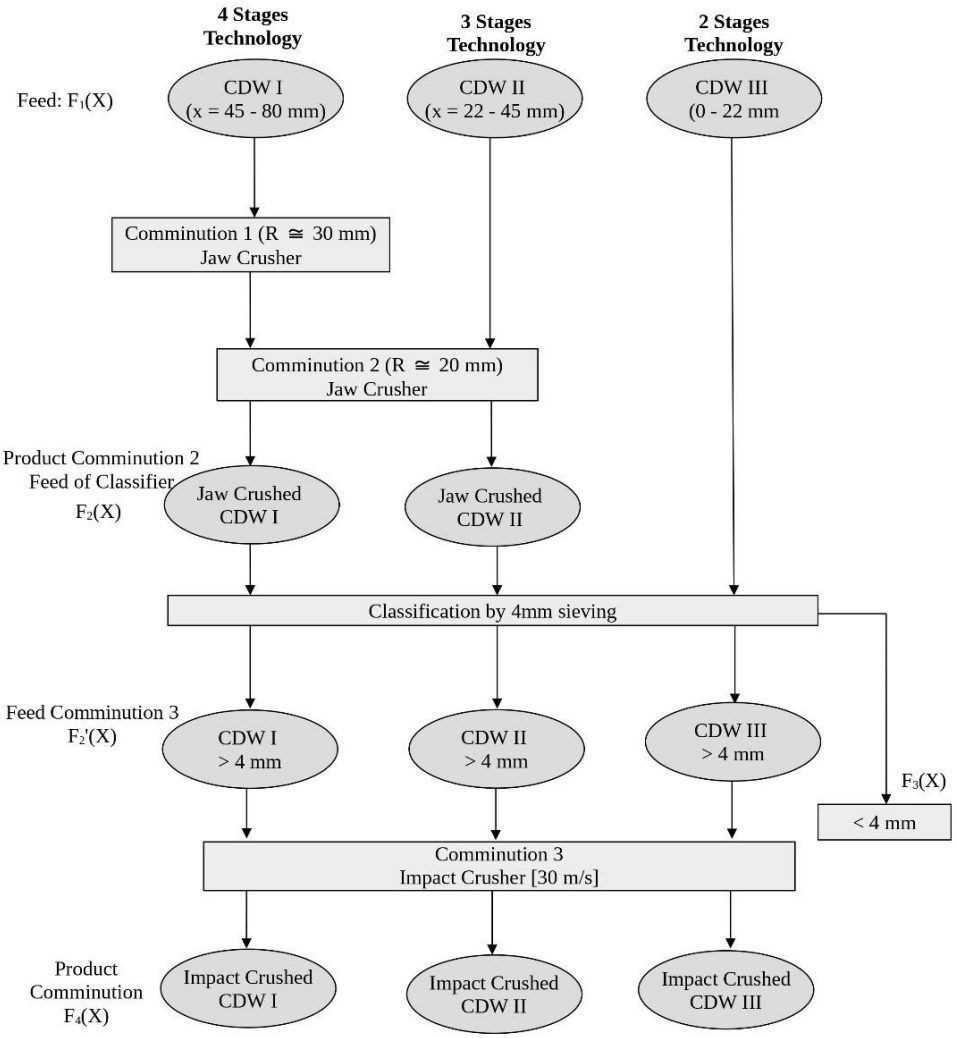

Figure 1: Flow sheet of CDW with different feed sizes

Figure 3

Flow sheet for crushing the CDW I (45–80 mm size), CDW II (22–45 mm size) & CDW III (0–22 mm size)

2.3. Flakiness Index

The flakiness index (FI) was conducted for aggregates CDW I and CDW II for sizes > 4 mm in this study. Based on the slot widths and particle size fractions according to European standards EN 933-3: 2012, whereby the slot widths are ½ the size of the particle size sieve passing the respective fraction. All the aggregates were assumed to be in a dry condition, within an enclosed laboratory.

$$FI = \frac{M_p}{M_T} \quad (1)$$

where M_P and M_T are the mass passing the slots, and the total mass of the respective fraction.

3. RESULTS

Particle cumulative undersize for the impact crushing products are illustrated in Figure 4 and 5, for CDW I, CDW II, and CDW III after impact crushing, also curved developed based European standards limits SIST EN 12620: 2013, for categories G_c 80/20 and sizes 4 mm (d) to 25 mm (D) i.e. (4/25) in Figure 4 and G_c 80/20 and sizes 4 mm to 14 mm (4/14) in Figure 5. G_c represent 80% passing lower limit size D and 20% passing upper limit size d.

In addition, Figure 6 presents the cumulative undersize of CDW IV, which is a mixture of CDW I, II & III for sizes < 4 mm and sieved from the impact crusher feed. The Figure 4 curves for CDW I and II against the 4/25 sizes had higher finer particles, the coarser proportions were within the limits. After removal of ¾ material of < 4 mm, the adjusted curves [denoted: ADJ] fitted the limit-based curves. The removed material represents 20.7% and 18.9% of the initial impacted crushed material for CDW I and CDW II, respectively. The Figure 5 curves for CDW III, the 4/14 sizes had higher finer particles, with coarser proportions generally within the limits, after removal of < 20 mm (2.18% of total crushed) and ¾ for < 4 mm portion (23.2% of total crushed), the ADJ curve fitted. Figure 6, the < 4 mm sieved from the 3 fractions, after jaw crushing CDW I and II and raw CDW III, the passing 50% and 80% i.e. D_{50} and D_{80} were 1.6 mm and 3 mm, showing an almost constant steepness from ≥ 60% undersize and relatively steeper at ≤ 20% undersize.

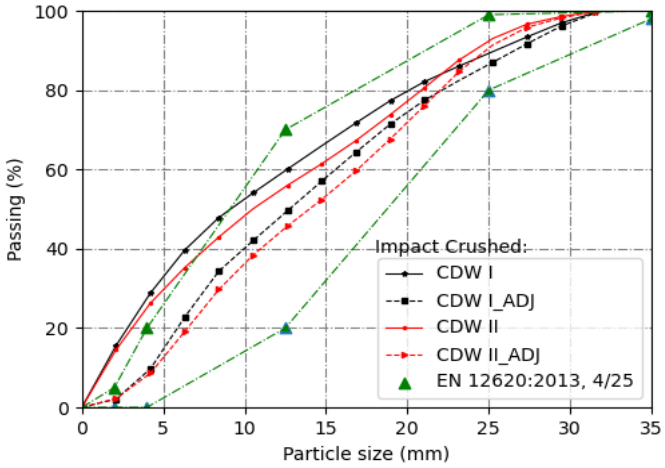

Figure 4

Particle size distribution for CDW I and II impact crushing products, sieve sizes of 40 to 4 mm, and 8 size fractions for CDW I and 10 for CDW II

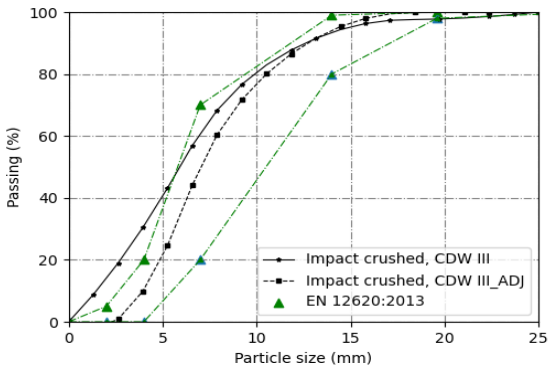

Figure 5

Particle size distribution, CDW III products after impact crushing with sizes ranging from 25 to 4 mm, and 7 size fractions

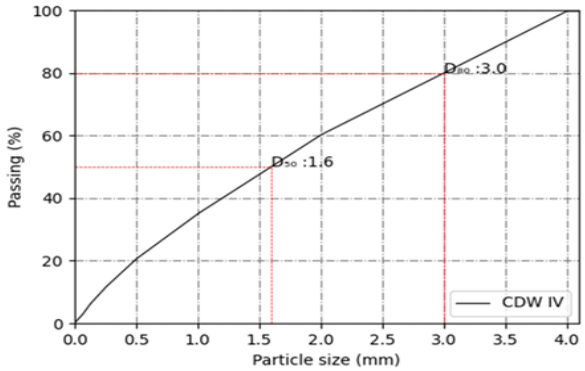

Figure 6

Particle size distribution for CDW IV with sizes <4mm from impact feed, sieve sizes of 8 to 0.063 mm, and 8 size fractions

Reduction ratios for 50% passing (r_{50}) and 80% passing (r_{80}), for the jaw crusher and impact crusher (30 m/s) are as illustrated in Table 2. Moreover, Figure 7 shows the jaw-crushed sample and Figure 8 illustrates the samples after impact crushing, with a visible size reduction. Based on those Figures, size reduction occurred for CDW I and CDW II after impact crushing and an increase in finer particles.

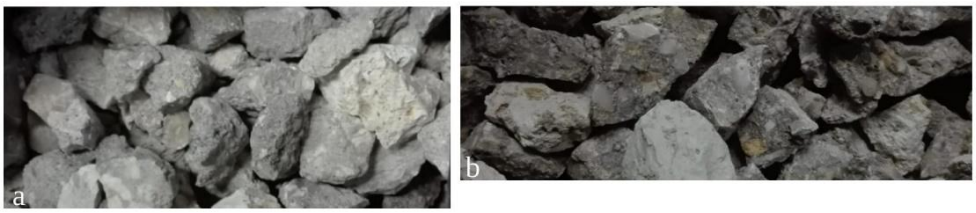

Figure 7

Jaw crushed concrete waste sample a) CDW II and b) CDW I.

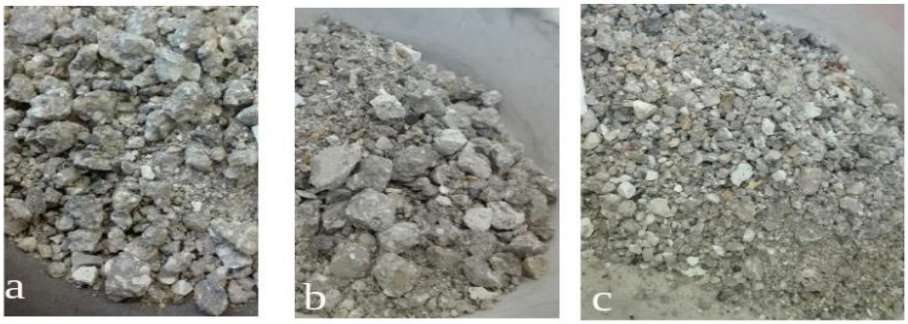

Figure 8
Impact crushed concrete waste at 30 m/s sample a) CDW I, b) CDW II, and c) CDW III.

Table 2
Reduction ratios at passing 50% (r_{50}) and 80% (r_{80}) for the jaw and impact crushers at 30 m/s

	CDW I		CDW II		CDW III	
	r_{50}	r_{80}	r_{50}	r_{80}	r_{50}	r_{80}
Jaw Crushed	2.5*	2.6*	1.4	1.7		
Impact Crushed	2.6	1.4	2.1	1.4	1.5	1.4
****Total**	**6.1**	**3.8**	**2.8**	**2.3**	**1.2**	**1.3**

*2 passes; ** 4 mm classifier before feeding into the impact crusher, hence the feed $\geq$4 mm.

The FI, for $\geq$ 4 mm is presented in Table 3 for CDW I & II, the maximum at 6.11%, based on the results, CDW I improved, from 6.11% to 3.23% after impact crushing but CDW II had just a marginal change/decline from 3.14% and 3.62%.

Table 3
Flakiness index (FI) for jaw crushed and impact crushed CDW I & CDW II

	CDW I		CDW II	
	Jaw crushed	Impact crushed	Jaw crushed	Impact crushed
FI	6.11%	3.23%	3.14%	3.62%

4. Discussion and Conclusions

The sampling preparation undertaken in this study proved very important as it ensured consistency in the CDW material. Furthermore, the size reductions achieved after crushing the CDW samples helped in the categorization of the samples into various aggregate categories suitable for different applications. The CDW I and CDW II reduction ratios (r_{50}) were 6.1 and 2.8 for the jaw crushing, 4 mm classifier, and impact

crushing, respectively and r_{80} of 3.8 and 2.3, respectively. Hence, almost a similar reduction ratio, with CDW I being marginally higher, could be due to the slightly higher raw material sizes for the larger particles (> 80 mm) and 2 passes for CDW I. There was not much difference between the CDW I and CDW II product sizes, the closeness of the reduction ratio value could indicate the similarity of properties for both factions. The CDW I and II lower and higher fractions were not within the 20 mm maximum limit curve ranges, however, the D_{50} were within the range. The CDW III was marginally not within the 10 mm maximum limit curve range.

Visibly, the aggregates produced by the impact crusher had regular shapes with reduced sharp edges. The FI for CDW I and II were below 4% after impact crushing and below 6.11% after jaw crushing, showing that the jaw and impact crushing aggregate shape could be suitable for concrete application. According to a study by Ulsen et al. (2013), impact crushing affected the sphericity of CDW-sand and rock-to-rock crushing, resulting in improved morphology.

According to Moreno-Juez (2021), higher LOI for CDW in comparison to cement was attributed to calcite content in the CDW. The Federal Highway Administration Research and Technology (USA) described the maximum LOI at 6% for fly ash or natural pozzolans as a Portland cement admixture. Moreover, according to ASTM C618-92a requirement, high carbon content (high LOI) results in a negative impact on air entrainment. In this study, the LOI values are in the range of 14–15%, in Table 1 which are significantly higher than the allowable limits of ordinary Portland cement (OPC). Based on the LOI, utilization of CDW binder from this study should be a consideration, particularly for the longer-term or durability concrete properties. Also, the study recommends further CDW binder's LOI control studies.

In a nutshell, this study underscores the significance of initial systematic preparation and characterization of recycled aggregates, however, there is a need to pursue further studies such as surface treatment and other properties. Further treatment is required to clean up the adhering mortar. This further treatment, coupled with selective material sizing can be considered for the CDW 4/14 and 4/25 mm coarse aggregate production. Besides, the CDW fines ($\geq$ 4 mm) from the classifier can be further processed for utilization as a concrete binder in future research. This study recommends additional property tests and further research to improve the quality of recycled aggregates including chemical or mechanical treatment.

ACKNOWLEDGMENTS

The publication was funded by the CiRCLETECH project (GA. nr. 101079354) funded by the European Union under the Horizon Europe programme. Appreciation is also due to staff members from the Institute of Raw Materials Preparation and Environmental Technology and the Department of Exploration Geoscience, both at the University of Miskolc.

REFERENCES

ASTM D1883-21(2021). *Standard test method for California Bearing Ratio (CBR) of laboratory-compacted soils, D18 Committee*.

SIST EN 933-3:2012 (2012). Tests for geometrical properties of aggregates-Part 3: *Determination of particle shape-Flakiness index*, Part 3:2012, CEN Bruxelles.

Bengtsson, M., Evertsson, C. (2006). Measuring characteristics of aggregate material from vertical shaft impact crushers. *Minerals Engineering*, 19 (15), pp. 1479–1486. doi:10.1016/j.mineng.2006.08.003.

Construction and demolition waste: challenges and opportunities in a circular economy, European Environmental Agency. Available online: https://www.eea.europa.eu/publications/construction-and-demolition-waste-challenges (Accessed on 28 September 2024).

Contreras-Llanes, M., Romero, M., Gázquez, M. J., Bolívar, J. P. (2021). Recycled aggregates from construction and demolition waste in the manufacture of urban pavements. *Materials*, 14 (21), p. 6605. https://doi.org/10.3390/ma14216605.

Hubert, J., Zhao, Z., Michel, F., Courard, L. (2023). Effect of Crushing Method on the Properties of Produced Recycled Concrete Aggregates. *Buildings*, 13 (9), p. 2217. https://doi.org/10.3390/buildings13092217

Li, Y., Zhang, S., Wang, R., Zhao, Y., Men, C. (2019). Effect of carbonation treatment on the crushing characteristics of recycled coarse aggregates. *Construction and building materials*, 201, pp. 408–420. https://doi.org/10.1016/j.conbuildmat.2018.12.158

Limbachiya, M. C. (2010). Recycled aggregates: Production, properties and value-added sustainable applications. *Journal of Wuhan university of technology-material science edition*, 25, pp. 1011–1016. https://doi.org/10.1007/s11595-010-0140-x

M 46-01.42, *Washington state department of transportation (WSDOT) material manual*, January 2023. Washington state department of transportation.

Martinez-Echevarria, M. J., Lopez-Alonso, M., Garach, L., Alegre, J., Poon, C. S., Agrela, F., Cabrera, M. (2020). Crushing treatment on recycled aggregates to improve their mechanical behaviour for use in unbound road layers. *Construction and Building Materials*, 263, p. 120517. https://doi.org/https://doi.org/10.1016/j.conbuildmat.2020.120517

Moreno-Juez, J., Vegas, I. J., Frías Rojas, M., Vigil de la Villa, R., Guede-Vázquez, E. (2021). Laboratory-scale study and semi-industrial validation of viability of inorganic CDW fine fractions as SCMs in blended cements. *Construction and building materials*, 271, p. 121823. https://doi.org/https://doi.org/10.1016/j.conbuildmat.2020.121823.

Qiu, J., Tng, D. Q. S., Yang E-H. (2014). Surface treatment of recycled concrete aggregates through microbial carbonate precipitation. *Construction and building materials*, 57, pp. 144–150. https://doi.org/10.1016/j.conbuildmat.2014.01.085

Reducing bulk samples to testing sizes by quartering (ASTM C702 and AASTHO R 76), Gilson Company Inc. Available online: https://www.youtube.com/watch?v=k0DXUx99UhI (Accessed on 28 September 2024).

SIST EN 12620:2013 (2013). *Aggregates for concrete*, CEN Bruxelles

Tarján, G. (1981) *Mineral processing, Volume I: Fundamentals, comminution, sizing and classification*. Akadémiai Kiadó, Budapest.

Test sieves for particle size distribution analysis in aggregates, Blau-Metall. Available online: https://labsieves.com/blau-metall/test-sieves-for-particle-size-distribution-analysis-in-aggregates/ (Accessed on 28 September 2024).

Ulsen, C., Kahn, H., Hawlitschek, G., Masini, E.A., Angulo, S.C. (2013). Production of recycled sand from construction and demolition waste. *Construction and building materials*, 40, pp. 1168–1173. https://doi.org/https://doi.org/10.1016/j.conbuildmat.2012.02.004

Ulsen, C., Tseng, E., Angulo, S. C., Landmann, M., Contessotto, R., Balbo, J. T., Kahn, H. (2019). Concrete aggregates properties crushed by jaw and impact secondary crushing. *Journal of Materials Research and Technology*, 8 (1), pp. 494–502. https://doi.org/https://doi.org/10.1016/j.jmrt.2018.04.008

User guidelines for waste and byproduct materials in pavement construction, Federal Highway Administration research and technology. Available online: https://www.fhwa.dot.gov/publications/research/infrastructure/structures/97148/cfa53.cfm (Accessed on 28 September 2024).

Wang, Z., Pan, C., Jiang, Y., Zhong, J., Tang, J. (2024). Impact crushing of waste concrete for coarse aggregate liberation by water jet. *Powder Technology*, 436, p. 119513. https://doi.org/https://doi.org/10.1016/j.powtec.2024.119513

Zhang, H.-L., Tang, Y., Meng, T., Zhan, L.-T. (2021). Evaluating the crushing characteristics of recycled construction and demolition waste for use in road bases. *Transportation Geotechnics*, 28, p. 100543. https://doi.org/https://doi.org/10.1016/j.trgeo.2021.100543

Responsible: Prof. dr. Péter Szűcs Vice-Rector
Published by the Miskolc University Press under leadership of Beáta Szabóné Kovács
Responsible for duplication: Erzsébet Pásztor
Number of copies printed:
Number of permission: MERT-2026 – 31 – ME
HU ISSN 2063-6997